ICE PROPERTIES DERIVED FROM REFLECTION SEISMICS AT A COLD ALPINE SADDLE AND A LOCAL ANTARCTIC DOME

Diplomarbeit

5. Juli 2010

eingereicht an der

Fakultät für Physik

Karlsruher Institut für Technologie (KIT)

durchgeführt am

Alfred-Wegener-Institut für Polar- und Meeresforschung (AWI)

von

Anja Diez

Referent: Prof. Dr. Thomas Bohlen (KIT)

Korreferent: Dr. Olaf Eisen (AWI)

Erklärung

Hiermit versichere ich, dass ich die vorliegende Arbeit selbständig und nur mit den angegebenen Hilfsmitteln verfasst habe.

Karlsruhe, den 5. Juli 2010

Zusammenfassung

Für paläoklimatische Rekonstruktionen oder um Vorhersagen über die Änderungen im Meeresspiegel treffen zu können, muss die Dynamik von Gletschern und Eisschilden verstanden werden. Dieses Wissen kann erhalten werden durch ein besseres Verständnis über physikalische Eiseigenschaften. Um diese physikalischen Eiseigenschaften herzuleiten, können reflexionsseismische Messungen durchgeführt werden. Solche Untersuchungen sind zur Zeit allerdings noch kein Standard.

Für diesen Zweck wurden Daten vom Colle Gnifetti, Monte Rosa, Schweiz und Halvfarryggen, Dronning Maud Land, Antarktis untersucht. Der Colle Gnifetti, ein alpiner Sattel, spiegelt sehr gut polare Eisbedingungen wieder und ist damit ein herausragendes Testgebiet in der Nähe. Durch den flachen Gletscher (60 m) und das dicke Firnpacket (30 m) war es nicht möglich interne Reflexionen herauszufiltern. Weitere Probleme beim Filtern traten auf durch parasitäre Resonanzen der Geophone. Trotzdem konnte die Tauchwelle verwendet werden um ein Dichteprofil des Firns und des Eises zu erstellen.

Am Halvfarryggen, einem Eisdom mit 900 m Eisdicke, konnten dafür deutlich interne Strukturen unterhalb der Firngrenze bis hin zum Felsbett beobachtet werden. Die Änderungen in der seismischen Geschwindigkeit, die diese Reflexionen hervorrufen, konnten durch die Analyse des Reflexionskoeffizienten in Beziehung gesetzt werden zu Änderungen im 'crystal orientation fabric' (COF). Die Ergebnisse unterstützen damit Eisdynamik-Modellierungen, die auf starke Orientierung der Kristalle im Eis und deren Änderungen über die Tiefe hindeuten.

Am Colle Gnifetti wurden zwei senkrecht zueinander orientierte Seismiklinien geschossen mit 34 Schüssen auf der Nord-Süd Linie und 33 Schüssen auf der Ost-West Linie. In der Nähe des Schnittpunkts gibt es eine Bohrkern. Von diesem Kern KCI sind Dichtedaten vorhanden. Zusätzlich wurden noch Radarmessungen durchgeführt, die mit den Seismikdaten verglichen werden konnten (Kapitel 3.1.1). Bei der Nord-Süd Linie, Schuss 34 war es möglich mit Hilfe eines FK-Filters die Bettreflexion herauszufiltern. Daher ist bekannt, dass die Bettre flexion ungefähr im Frequenzbereich von 20 bis 220 Hz liegt. Für alle anderen Schüsse war es leider nicht mögliche die Bettreflexion heraus zu filtern, da die Reflexion von Oberflächenwellen, Tauchwellen und refraktierten Wellen überlagert wird. Diese Wellen Überlagern sich sowohl im Zeit-Offset Bereich, als auch im Frequenzbereich. Verschiedene Filter, FK-Filter, KL-Transformationen, Frequenzfilter und Dekonvolu-

tion wurden vor dem Stapeln der Daten getestet ohne ein zufriedenstellendes Ergebnis zu liefern. Eine Verbesserung der Daten konnte erreicht werden durch das Stapeln und anschließendes FK-filtern. Somit konnte zumindest die Bettreflexion herausgefiltert werden, allerdings war es nicht möglich interne Reflexionen aus dem Eis zu finden (Kapitel 4.2).

Ein weiteres Problem in den Daten sind parasitäre Resonanzen. Ein Vertikalgeophon soll sich eigentlich nur in vertikal Richtung bewegen können. In Wirklichkeit hat es allerding mehr Freiheitsgrade, z.B. in Horizontalrichtung. Dadurch kommt es in der Übertragungsfunktion des Geophons zu Phasensprüngen und Variationen in der Sensitivität. Dies äußert sich durch ein starkes Nachschwingen im Seismogramm. Um dieses Rauschen zu unterdrücken und die Daten deutlich zu verbessern, wurden die Spuren mit Offset 1,5 m gelöscht (Kapitel 4.3).

Die Tauchwellen konnten allerdings verwendet werden um Dichteprofile zu erstellen. Diese Ergebnisse konnten dann mit den Dichtedaten vom Bohrkern KCI verglichen werden. Der Strahlparameter p ist konstant über den Weg einer Welle und entspricht am untersten Punkt der Tauchwelle gerade dem inversen der Geschwindigkeit in dieser Tiefe. Die zu dieser Geschwindigkeit gehörende Tiefe kann dann mit der Inversionsformel von Herglotz-Wiechert berechnet werden. Dafür musste zunächst eine Exponentialfunktion an die Laufzeitkurven der Tauchwellen angepasst werden, mit deren Hilfe dann die Geschwindigkeiten berechnet werden konnten. Aufgrund der Inhomogenität der gepickten Laufzeitkurven wurde die Exponentialfunktion an verschiedene Gruppen der Datensätze der Laufzeitkurven angepasst. Die so erhaltenen Geschwindigkeits-Tiefen Profile konnten dann mit Hilfe einer empirischen Formel von Kohnen in Dichtedaten umgerechnet werden. Der Vergleich der berechneten Dichtedaten aus den Tauchwellen und den gemessenen Dichtedaten von dem Bohrkern KCI zeigt eine sehr gute Übereinstimmung (Kapitel 5.1).

Der zweite Datensatz stammt vom Halvfarryggen, einem lokalen Eisdom, an dem aus früheren Radarmessungen Anisotropie erwartet werden konnte. Am Halvfarryggen wurde nur eine Seismiklinie, mit 10 Schüssen, geschossen. Durch das deutlich dickere Eis (900 m) und die größeren Geophonabstände, wie auch größeren Offsets war das Prozessieren der Daten deutlich einfacher als am Colle Gnifetti. Mit Hilfe von FK-Filtern und Frequenzfiltern war es möglich interne Strukturen herauszufiltern (Kapitel 4.4). Dies war das erste Mal, dass mit Hilfe von Seismik so deutlich interne Strukturen an einem Eisdom beobachtet werden konnten. Interne Schichten treten dabei auf ab einer Tiefe von ungefähr 300 m bis hinunter zum Felsbett (Kapitel 4.5.3).

Die einzelnen Schichten wurden dann weiter untersucht. Dabei war speziell ein starker Reflektor knapp oberhalb des Betts von Interesse. An diesem sollte eine 'Amplitude gegen Winkel' (Amplitude versus Angle, AVA) Analyse durchgeführt werden. Da der zu betrachtende Reflektor ungefähr in einer Tiefe von 900 m liegt und der größte verwendet Offset 495 m ist wurden nur 15° Einfallswinkel abgedeckt. Bei einer AVA-Analyse versucht man allerdings Kurven berechneter Reflexionskoeffizienten mit den Kurven der gepickten Amplituden Werte zu vergleichen um durch Besonderheiten im Kurvenverlauf auf den Reflexionkoeffizienten zu schließen. Innerhalb der ersten 15° sind alle diese Kurven, die man für eine Änderung in der seismischen Geschwindigkeit im Eis berechnen kann, flach und lassen daher keine Rückschlüsse auf den Reflexionskoeffizienten zu (Kapitel 5.2).

Allerdings gibt es die Möglichkeit die gepickten Amplitudenwerte zu skalieren, wobei verschieden Abschätzungen gemacht werden müssen, z.B. für die Dämpfung der Welle. Somit konnte abgeschätzt werden, dass die betrachtete Reflexion aufgrund einer Geschwindigkeitserhöhung von 5-15 m/s entsteht. Diese Reflexion hat eine positive Reflexionsamplitude, bei nahezu allen anderen beobachtbaren Schichten ist die Reflexionsamplitude negativ. Dies bedeutet, dass die Geschwindigkeit sich bei den Schichten mit negativer Reflexionsamplitude von der ersten zur zweiten Schicht verringert.

Diese Geschwindigkeitsänderungen entstehen vermutlich aufgrund von Änderungen im 'crystal orienttion fabric' (COF), also durch Änderungen der Orientierung der verschieden Eiskristalle im gesamten Eisvolumen. Eine P-Welle mit Ausbreitungsrichtung entlang der c-Achse eines Eiskristalls ist 120 m/s schneller als wenn ihre Ausbreitungsrichtung senkrecht zur c-Achse ist. Eis wird normalerweise als isotrop betrachtet. Aufgrund der Spannungen in einem Eisschild oder einem Gletscher können sich die Eiskristalle allerdings ausrichten. Dies führt zu Änderungen in den seismischen Geschwindigkeiten. Eine Änderung von isotroper Eiskristallverteilung zu einem vertikalen Gürtel, also alle c-Achsen in einer Ebene, führt zu einer Erhöhung der P-Wellengeschwindigkeit in vertikaler Richtung um 40 m/s. Dabei kann ein vertikaler Gürtel allerdings parallel oder auch senkrecht zur Schusslinie orientiert sein. Da die P-Wellengeschwindigkeit von ihrer Ausbreitungsrichtung abhängt, setzt sie sich sowohl aus einem Anteil Vertikal- wie auch Horizontalgeschwindigkeit zusammen. Die Drehung eines Gürtels von vertikaler, paralleler Orientierung zur Seismiklinie zu einer Orientierung vertikal und senkrecht zur Seismiklinie würde damit aufgrund der horizontalen Komponente zu einer Geschwindigkeitsverminderung führen. Eine weitere Möglichkeit für Geschwindigkeitsverminderung ist, wenn die c-Achsen zunächst vertikal orientiert sind und sich dann wieder weiter entfernen von der Vertiklen, also wieder hor-

izontaler orientieren. Die Geschwindigkeitserhöhung der letzten Schicht kommt hingegen vermutlich durch eine zunehmende Vertikalisierung der c-Achsen (Kapitel 5.2.4).

Es konnte somit gezeigt werden, dass am Colle Gnifetti eine veränderte Schussgeometrie von Nöten ist um interne Reflexionen im Eis, falls sie existieren, zu detektieren. Auch wenn keine internen Strukturen heraus gefiltert werden konnten, konnte die Tauchwelle verwendet werden um Dichteprofile zu erstellen. Die fehlenden internen Reflexionen am Colle Gnifetti konnten dafür am Halvfarryggen beobachtet werden. Zum ersten Mal war es möglich mit Hilfe von Reflexionsseismik deutlich interne Strukturen im Eis eines Eisdoms zu beobachten. Die AVA-Analyse ist dabei eine vielversprechende Möglichkeit um auf die Geschwindigkeitsänderungen im Eis zu schließen. Abschätzungen der Geschwindigkeitsänderungen konnten mit Hilfe einer Abschätzung des Reflexionskoeffizienten gemacht werden. Diese Geschwindigkeitsänderung deuten auf Anisotropie im Eis und damit auf Änderungen im COF hin.

Abstract

For paleoclimate reconstructions or to predict future changes in sea level rise the dynamics of ice need to be known. This knowledge can be gained by a better understanding about the physical properties of ice. To derive these ice properties reflection seismics can be carried out. Up to now it is not very common to investigate internal structures of glaciers with the help of seismic measurements.

For this purpose data from Colle Gnifetti, Monte Rosa, Switzerland and Halvfarryggen, Dronning Maud land, Antarctica were analyzed. Colle Gnifetti, an alpine saddle, resembles very well polar ice conditions and is thus an excellent test area close by. The shallow glacier (60 m) and the thick firn pack (30 m) made it impossible to filter out internal reflections. Further problems during filtering occurred due to parasitic resonances of the geophone. Nevertheless the diving wave could be used to derive a density profile of the firn and ice.

At Halvfarryggen, a local dome of 900 m thickness, internal reflections could clearly be observed below the firn transition zone down to the bed. It was the first time that internal reflections could be observed at an ice dome. The changes in seismic velocity, which caused the reflections, could then be linked to changes in crystal orientation fabric (COF) by the analysis of the reflection coefficient and partly by an amplitude versus angle (AVA) analysis. The results thus support ice-dynamic modeling studies which indicate the presence of strongly oriented crystal fabric and their changes over depth.

Contents

List of Figures

List of Tables

1 Introduction

With ongoing warming of the global climate the question of the behavior of mountain glaciers and polar regions to temperature increase becomes more and more important. It is necessary to be able to predict glacier melting and their contribution to sea level rise [IPCC, 2007]. Mountain glacier react quickly to temperature variations. Their behavior is therefore important because of glacier hazards like ice fall, rock fall or glacier dammed lakes putting the people living in the mountains under risk. Additionally, they provide the biggest fresh water resource in the mountains.

To be able to predict the responds of glaciers and ice sheets to changes in climate, ice flow models need to be improved. A good understanding about the physical properties of glaciers is thus necessary. To gain information about physical properties like density, temperature, crystal size or crystal orientation an ice core would normally be drilled. However, ice cores can only give information about one local point. Next to this, drilling a deep ice core is time, labor and cost intensive. The big advantage of geophysical methods is that they can provide information about physical properties of ice over a much larger area with considerably less effort.

Seismic measurements on glaciers were quite popular up to the 80s carried out by for example Robin [1958], Kohnen [1974] and Bentley [1972]. Slichter [1932] was the first to use the travel times of the diving wave to derive velocities for the ice, with help of the Herglotz-Wiechert inversion (chapter 5.1.2). During the Norwegian-British-Swedish Antarctic expedition Robin [1958] investigated the ice more comprehensively. He derived a linear relationship between P-wave velocity and density (equation 8), investigated the behavior of P-waves to changes in temperature and crystal orientation. Similar topics, the relation ship between seismic velocity and density of firn or the relationship between velocity and ice temperature were as well investigated by Kohnen [1972, 1974] and Kohnen and Bentley [1973]. The influence of anisotropic ice on seismic velocity was described by Bentley [1972]. Then the advantage of radar and its high resolution was used. However seismic measurements can give additional information to radar results about the properties of ice. In the last years seismics was more used to investigate the bed and the conditions at the bed [Blankenship et al., 1986, King et al., 2004, 2007, Smith and Murray, 2008, Smith, 2007]. Ice itself was for example investigated by King and Jarvis [2007] who calculated the Poisson ratio of polar firn. To reveal the basal condition amplitude versus offset (AVO)

analyses were used. New approach to use AVO to determine the bed conditions were developed by Anandakrishnan [2003] and Holland and Anandakrishnan [2009]. Although nowadays seismics is mostly used to investigate the glacier bed, we are interested in the advantages of seismics to investigate internal structures of glaciers.

The Emmy-Noether research group LIMPICS is interested in 'Linking micro-physical properties to macro features in ice sheets with geophysical techniques' (LIMPICS on www.awi.de). To achieve this radar as well as seismic measurements are carried out. Both methods provide different information about the ice properties. Before applying the methods to ice sheets they are first tested on a glacier in Switzerland.

The aim of this diploma thesis is to investigate reflections from within the ice and derive physical properties with the use of reflection seismics. The following questions were asked:

- Can internal reflections be observed with reflection seismics?

- Can an anisotropic behavior be identified with help of an amplitude versus offset (AVO) analysis?

- Can an AVO analysis indicate changes in crystal orientation fabric (COF)?

- Can a density profile be derived from the data and does it fit to ice core data?

To be able to answer these questions two data sets were used, one from Colle Gnifetti, a saddle in the Monte Rosa massif, Switzerland and one from Halvfarryggen, a local dome in Dronning Maud Land, Antarctica.

Colle Gnifetti gives the opportunity to test geophysical methods on a glacier close by with low logistic effort. Although it is a mountain glacier it resembles very well polar ice conditions and is a well studied area. Colle Gnifetti has an comparably large firn pack of 30-40 m, in comparison to the glacier thickness, which is about 60-120 m. With the used shot-receiver geometry, the large firn pack and the shallow character of Colle Gnifetti, processing became quite difficult and it was not possible to investigate internal structures of the ice. However the diving wave could be used to derive a density-depth profile to be compared to the density data from an ice core.

The processing for the Halvfarryggen data turned out to be a lot easier due to the larger ice thickness of about 900 m. Thus internal layers could clearly be observed for the very first time at an ice dome and used to carry out amplitude versus offset analyses to derive information about the crystal orientation fabric.

In the first part the theory of seismic wave propagation in ice and glaciological basics are described. Afterwards, the two field sites are introduced (chapter 3). In chapter 4 the different processing steps are explained that were applied to the Colle Gnifetti and Halvfarryggen data to obtain satisfying results. Some problems occurred here, especially for the processing of the Colle Gnifetti data because of parasitic resonaces. Based on the finally processed data (chapter 4.5), the diving wave could be used to derive the density distribution of the firn pack at Colle Gnifetti (chapter 5.1).

The larger ice thickness at Halvfarryggen compared to Colle Gnifetti and the bigger geophone-receiver spread made it possible to use the observed internal layers for a limited amplitude versus offset analysis (chapter 5.2) and thus analyze the crystal orientation fabric over depth.

2   Seismics on ice - Basics

2.1   Glaciology

A brief introduction into some glaciological features is given here, to understand why seismics may by a tool to investigate physical properties of ice. The data from Colle Gnifetti and Halvfarryggen comes from the accumulation area. The accumulation area is the part of the glacier where the snow gets compacted more and more to become ice, thus adding up to the volume of the glacier or ice sheet. The ablation area is the part where the glacier ice melts, reducing the mass of the glacier [Paterson, 1994].

2.1.1   Densification of snow

In the accumulation area of a glacier, where our field surveys are carried out, snow is densified to glacier ice. Afterwards it flows downwards, melting in the ablation area. For the process of densification of snow to glacier ice it is important whether this process is without or with melting of snow.

The accumulation area can be split into different zones, like described by Benson in 1961, due to their different characteristics of melting of snow and the refreezing after infiltration of the melt water [Paterson, 1994]. In the dry-snow zone densification occurs without melting, this process is known as sintering. The classical model for this densification process is the one by Herron and Langway [1980]. During the process different mechanisms in different phases are mainly responsible for the snow to become ice (Figure 1). All mechanisms aim at minimize the free energy. To reduce the free energy the surface area needs to be reduced. First the new snow is altered mechanically, often by strong wind. Branches of the snow crystals break off, crystals develop from their typical dendritic form to rounded grains. These rounded grains are then packed in the densest possible way, corresponding to 40 % porosity, as experiments have shown [Paterson, 1994]

After the rounded grains have been packed in the densest possible way the free energy is further minimized by sublimation. With sublimation the free pore space can be filled. As the overburden pressure increases recrystalisation takes place, bigger grains are growing to the expend of smaller ones and the grains are further deformed by movement along gliding planes within the crystal structure.

The density of 830 kg/m^3 is known as the 'pore-close off'. After this point an exchange of air with the surface is no longer possible. The remaining air within the ice, about 10 % of the volume, is enclosed in bubbles. Further densification, up to 910 kg/m^3, is now due to

the compression of the air bubbles. Figure 2 shows a typical density-depth profile. Ice is
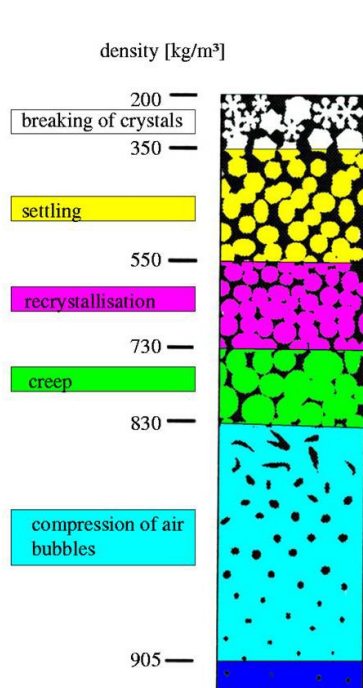
Figure 1: Process of snow
becoming ice (according to
Stauffer [1985])
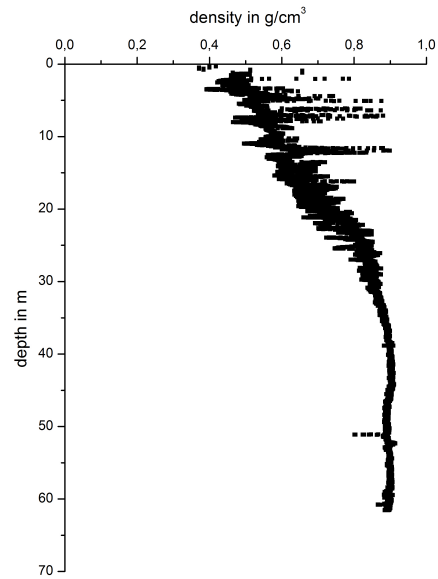
Figure 2: Density profile of ice core
KCI, at Colle Gnifetti (density data,
Pascal Bohleber, personal communica-
tion)

defined as glacier ice, after the value of 830 kg/m^3 is reached. Firn in comparison is not
defined by a density value, instead as snow that lasts for more than one year.

If the densification process takes place in the wet-snow zone where melting occurs, the
process is a much faster than in the dry-snow zone. The main processes remain the same,
the difference is characterized by the melt water that infiltrates into the snow and firn
pack. The rounding of the grains is faster, as the fragile branches of the crystals melt away
first. Additionally smaller grains melt more easily so that bigger grains grow faster as well.
The infiltrated water can than refreezes within the pore space. Hereby the 'close off' in the
wet-snow zone is reached in a more shallow depth creating glacier ice more rapidly than
in the cold-snow zone. A zone between cold-snow zone and wet-snow zone is called the
percolation zone. Some melt water exists here that infiltrates into the snow pack as deep
as this years snow, creating small ice lenses or ice layers.

Because of the density gradient within the firn layer of a glacier there is a strong velocity
gradient for the seismic waves, especially in the upper layers. This will have an influence

on the travel path of these waves, which will be explained in more detail later (chapter 5.1).

2.1.2   Crystal orientation fabric

To understand why the crystal orientation within a glacier or ice sheet is of importance, one needs to have a certain knowledge of ice structure.

There are 12 different phases of ice. But on earth under normal atmospheric conditions only hexagonal ice (Ih) exists, as the phase depends on temperature and pressure. The oxygen atom of the water molecule H_2O is bonded with four water atoms, building a tetrahedron. These tetrahedrons then build up the hexagonal structure of ice (Figure 3). Because of the hexagonal structure of ice on earth an ice crystal itself is anisotropic. The axis perpendicular to the basal plane is called the c-axis. The axis lying within the basal plane is called the a-axis (Figure 4). Glacier ice is normally isotropic. As the ice crystal
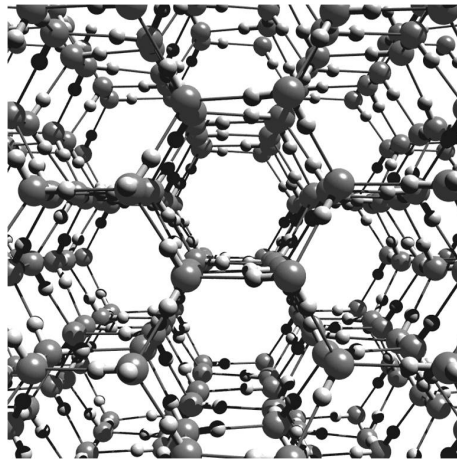
Figure 3: Structurer of the ice crystal, c-axis coming out of the picture (Lecture Physics of the Ice, ETHZ, T. Hondoh)

itself is anisotropic, the glacier ice is isotropic due to random orientation of the single crystals. However, due to different stresses crystals can be rotated, and the glacier ice can become anisotropic.

Glacier ice flows as visco-plastic material. This viscosity depends highly on the crystal orientation. Flow of ice is due to processes within the grains like dislocation climb and glide, mainly basal gliding and between the grains like recrystallization, diffusion or rotation of grains.

Within a crystal different glide plans exist like the basal plane, the prismatic plane or the pyramidal plane. The resistance for gliding on the basal plane is a lot smaller then for

gliding on the other planes, because the bonding within the basal plane is much stronger. The strength of bonding depends on the distance between the molecules. Because of the higher number of oxygen atoms within the basal plane, this distance is smaller compared to the other gliding planes. This means that the stress that needs to be applied to generate a strain for example of 1.0 a^{-1} is 0.03 MPa for glide on the basal plane and 3 MPa for glide on an other plane [Hooke, 2005]. Near the bed of an ice sheet or glacier simple shear
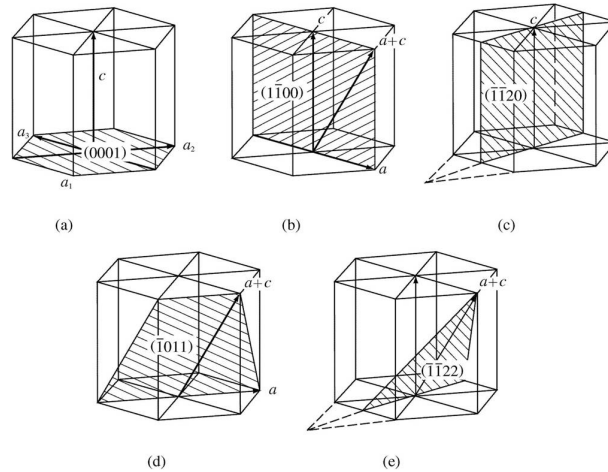
Figure 4: Different glide planes in the ice crystal (Lecture Physics of the Ice, ETHZ, T. Hondoh)

occurs. Hence the crystals start to rotate so the basal plane gets rotated towards the shear plane and the c-axis will therefore be vertical [Alley, 1988]. This leading to an anisotropic layer of ice just above the bed.

This crystal orientation fabric (COF) can be displayed in Schmidt diagrams where each point gives the direction of one c-axis (Figure 5). The viscosity of ice is stress dependent and depends on the crystal orientation. As the viscosity of ice depends on its COF, it has an influence on seismic velocities [Alley, 1988] (chapter 2.2.3). A wave parallel to the c-axis is therefore faster than one along the a-axis [Horgan et al., 2008].
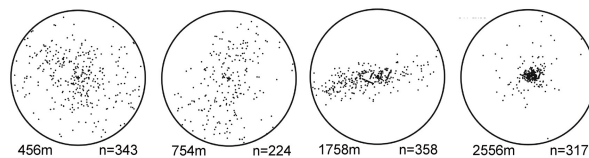
Figure 5: Example for COF from the ice core EDML, complete COF plots for more depth station see appendix A.1 (Ilka Weikusat, personal communication)

2.1.3   Glacier flow

As mentioned before ice is a visco-plastic material. To describe the flow of a glacier, the ice is usually treated as isotropic.

If stress is applied, glacier ice first reacts elastically (Figure 6, a), before it starts to creep. In glacier flow stress is applied for a longer period, therefore secondary and tertiary creep of ice is the dominant behavior and the deformation is not reversible. If a seismic wave moves through the ice, this period is very small and the deformation is elastic, thus reversible. Glacier flow adds up through different parts, the deformation of the ice, the gliding over
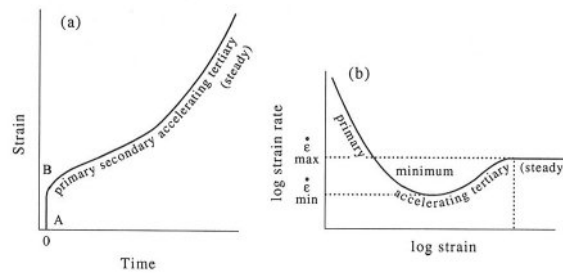
Figure 6: Creep of glacier ice with different stations, (a) time dependent and (b) strain dependent [Paterson, 1994]

the bed and if existing deformation of the subglacial till.

The deformation of ice can be described with Glen's flow law [Paterson, 1994], an empirical law for secondary creep

$$\dot{\epsilon} = A\tau^n \tag{1}$$

with $\dot{\epsilon}$ the effective strain rate and τ the effective stress rate. A is a variable that depends on temperature, impurities, crystal size and water content, as well as the initial stress state. By experiments n was found to be approximately 3. The effective strain rate is given by $\epsilon^2 = (1/2)\varepsilon_{ij}\varepsilon_{ij}$ and the effective stress rate by $\tau^2 = (1/2)\sigma^d_{ij}\sigma^d_{ij}$. Effective strain rate and effective stress are the second invariants of the strain rate tensor ε respectively the deviatoric stress tensor σ^d. The indexes i, j stand for the three directions in space x, y, z.

As ice is an incompressible material isotropic pressure can not induce deformation. This means $\dot{\varepsilon}_{ij}\delta_{ij} = 0$, with $\delta_{ij} = 0$ the Kronecker delta. It is therefore a necessary way to express Glen's flow law in relation to the deviatoric stress tensor σ^d. The first invariant of the stress tensor σ is the mean stress $\sigma_m = (1/3)\sigma_{ii}\delta_{ij} =$. Because of the incompressibility of ice this mean stress does not contribute to deformation. The deviatoric stress is then

given by

$$\sigma_{ij}^d = \sigma_{ij} - \frac{1}{3}\sigma_{ij}\delta_{ij} \tag{2}$$

with σ_{ij} a component of the stress tensor. By that the devitaoric stress is the stress that really contributes to the deformation.

Glens flow law can than be expressed in the following form

$$\dot{\varepsilon}_{ij} = A\tau^{n-1}\sigma_{ij}^d. \tag{3}$$

It is the most commonly used flow law in glaciology. Other flow laws exist as well. They take into account the crystal size, impurities, anisotropies etc. The effective viscosity η of ice is given by

$$\eta = \frac{1}{2A\tau^{n-1}} \tag{4}$$

which can be found by comparing the relation for a Newtonian fluid

$$\dot{\varepsilon}_{ij} = \frac{1}{2\eta}\sigma_{ij}^d \tag{5}$$

with equation (3) [Lüthi and Funk, 2008]. Glacier ice is therefore a non-Newtonian fluid as the viscosity is stress dependent and the relationship between viscosity and stress is non-linear. In the case of ice the viscosity decreases when the strain rate increases.

2.2 Seismics

When a seismic survey is carried out on glaciers, some specialties occur compared to seismic survey on land or water. Because of the strong density gradient of firn, waves are refracted continuously. These diving waves can be used to calculate for example velocity profiles (chapter 5.1.2). Because of the vertical density distribution and the continuous refraction in frin, first arrivals in a seismogram are not straight lines but bended ones, which makes processing more complicated. Additionally, the strong ground roll is normally a big disturbance for the processing.

2.2.1 Velocity profile

In seismic data processing it is very important to have a good velocity profile for the normal-move-out (NMO) correction (chapter 4.1.5) to get the best possible stack. As the seismic velocity depends on the density ρ

$$v_p = \sqrt{\frac{\kappa + 4/3\mu}{\rho}} \tag{6}$$

$$v_s = \sqrt{\frac{\mu}{\rho}} \qquad (7)$$

a velocity profile can be obtained if density values are known. Here κ is the bulk modulus and μ the shear modulus.

An empirical relationship between snow/ice density and P-wave velocity was derived by Robin [1958]. Measurements from the Norwegian-British-Swedish Antarctic Expedition, 1949-52, laboratory tests as well as tests at the Jungfraujoch, Switzerland were carried out. The following, linear relationship, was derived

$$\rho = 2.21 \cdot 10^{-4} v_p + 0.059 \qquad (8)$$

with v_p in m/s and ρ in g/cm^3. This formula was limited to a depth greater than 10 m and therefore a density higher then 0.58 g/cm^3.

Kohnen [1972] came up with a more precise formula for the density ρ derived from the P-wave velocity v_p at depth z

$$\rho(z) = \frac{0.915}{1 + \left(\frac{v_i - v(z)}{2.25}\right)^{1.22}}. \qquad (9)$$

The velocity $v_i = 3800$ m/s represents the P-wave velocity in ice.

If no density data is available the velocity function can be obtained using the diving waves. This approach will be explained in detail in chapter 5.1.

2.2.2 Diving wave

Because of the strong density gradient in the firn pack of a glacier diving waves exist here. A wave is traveling through a horizontally layered medium, with a constant velocity in each layer. Hence the wave is refracted at each layer boundary. These refractions can be calculated using Snell's law

$$\frac{sin(\alpha_i)}{v_i} = \frac{sin(\alpha_{i+1})}{v_{i+1}} = p. \qquad (10)$$

The ray parameter or horizontal slowness p is a constant over each ray. The wave reaches the turning point when $p \cdot v(z) = 1$. Here the emergent angle is $\alpha_{i+1} = 90°$ and the slowness p equals the inverse of the velocity $v(z)$ at this point ($p = \frac{1}{v(z)}$).

If the thickness of the layers reaches infinity the velocity can be described by a velocity gradient $v(z) = v_0 + m(z) \cdot z$. Hence the ray is refracted continuously and describes a semicircle if m is a constant. These rays are called direct wave, diving wave or turning ray

(Figure 44, chapter 5.1).

These types of waves are normally more common in seismology. Due to the density gradient and therefore the velocity gradient in the firn pack diving waves are the first arrivals in seismograms from a glacier or ice sheet.

2.2.3   Zoeppritz equation

The transmitted and reflected amplitudes of a seismic wave at a transition zone for different incoming angles are described by the Zoeppritz equations. The angle of a reflection of a seismic wave can be calculated via Snell's law (equation 10). To learn something about physical properties of the reflection horizon it is however interesting to know the reflection coefficient R. The energy of an incoming wave I_e, which is proportional to the square of the absolute value of the amplitude A, gets splited into the intensity of the transmitted wave I_t and the reflected wave I_r ($I_e = I_t + I_r$). For a normal incident P-wave, a P-wave gets reflected and a part gets transmitted. The reflection coefficient is then described by the acoustic impedance $Z_i = \rho_i v_{p,i}$ of the first ($i = 1$) and the second ($i = 2$) layer,

$$R = \frac{\sqrt{I_r}}{\sqrt{I_e}} = \frac{A_2}{A_1} = \frac{Z_2 - Z_1}{Z_2 + Z_1}. \tag{11}$$

This means that the reflection coefficient only gets negative when the acoustic impedance of the second layer is smaller than the acoustic impedance of the first layer.

Here the reflection coefficient is defined by the amplitude, but it can as well be defined by the power $R_{power} = I_r/I_e$.

If the wave however is not normal incidence, an incoming P-wave generates a transmitted and reflected P-wave as well as a transmitted and reflected S-wave as shown in Figure 7. Thereby the reflection coefficient depends on the angle of incidence and the acoustic impedance of both, the P-wave as well as the acoustic impedance of the S-wave $W_i = \rho_i v_{s,i}$. The propagation of a wave at an interface is then described by the Zoeppritz equations [Yilmaz, 2001]:

$$A_1 cos\theta_1 - B_1 cos\delta_1 + A_2 cos\theta_2 + B_2 cos\delta_2 = A_0 cos\theta_1 \tag{12}$$

$$A_1 sin\theta_1 + B_1 cos\delta_1 - A_2 sin\theta_2 + B_2 cos\delta_2 = -A_0 sin\theta_1 \tag{13}$$

$$A_1 Z_1 cos2\delta_1 - B_1 W_1 sin2\delta_1 - A_2 Z_2 cos2\delta_2 - B_2 W_2 sin2\delta_2 = -A_0 Z_1 cos2\delta_1 \tag{14}$$
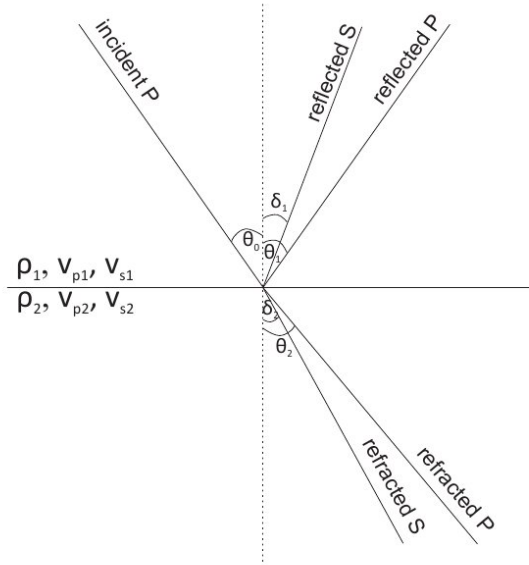
Figure 7: A P-wave gets reflected at a discontinuity, generating reflected and transmitted P- and S-waves

$$A_1(\frac{v_{s,1}}{v_{p,1}})W_1 sin2\theta_1 + B_1 W_1 cos2\delta_1 + A_2(\frac{v_{s,2}}{v_{p,2}})W_2 sin2\theta_2 - B_2 W_2 cos2\delta_2 = A_0(\frac{v_{s,1}}{v_{p,1}})W_1 sin2\theta_1 \tag{15}$$

The index 1 stands for the reflections, index 2 for the transmitted wave, with the P-wave amplitudes A, incoming wave A_0 and the S-wave amplitudes B. The incident angle of the P-wave θ_0 is equal to the emergent angle of the reflected P-wave θ_1. To get the reflection amplitudes as solution, some good approximations exist, e.g. Aki and Richards [2002]. Here, the notation $R(\theta)$ is used for the angle dependent reflection amplitude A_1 [Yilmaz, 2001],

$$R(\theta) = \left[\frac{1}{2} \left(1 + \tan^2 \theta \right) \right] \frac{\Delta v_p}{v_p} - \left[4 \frac{v_s^2}{v_p^2} \sin^2 \theta \right] \frac{\Delta v_s}{v_s} + \left[\frac{1}{2} \left(1 - 4 \frac{v_s^2}{v_p^2} \sin^2 \theta \right) \right] \frac{\Delta \rho}{\rho} \tag{16}$$

with $\Delta v_p = v_{p,2} - v_{p,1}$, $\Delta v_s = v_{s,2} - v_{s,1}$, $\Delta \rho = \rho_2 - \rho_1$ and $v_p = (v_{p,1} + v_{p,2})/2$, $v_s = (v_{s,1} + v_{s,2})/2$, $\rho = (\rho_1 + \rho_2)/2$.

Normally, the reflection coefficient is unknown. Carrying out an amplitude versus offset (AVO) or versus angle (AVA) analysis can help to figure out something about the acoustic impedance and therefore about the physical properties of the reflection horizon. This is possible because the amplitude versus offset curve has some characteristic features depending on the acoustic impedance.

The AVO approach is interesting for reflections of internal layers in an ice sheet. The den-

sity ρ can be assumed constant for deeper layers. When COF changes the viscosity of the ice changes and therefore the shear modulus as well, leading to a change in seismic velocity and therefore to a reflection. The difference in seismic velocity parallel or perpendicular to the c-axis is around 120 m/s for P-waves and 100 m/s for S-waves [Anandakrishnan et al., 1994, Kohnen and Bentley, 1973].

2.2.4   Seismic source

As source for seismic surveys a source with a signal closest to a delta pike is preferable. For land surveys different seismic sources are in use. The most basic technique is the use of a sledgehammer. The sledgehammer is blown on to a plate lying flat on the earth surface, creating a shock wave. This technique is of course only useful for very shallow surveys, where little energy is needed.

The use of explosives is more powerful as a seismic source. Another powerful source is dropping of a weight, e.g. a plate (3000 kg). A big truck is needed for this approach so it is only useful in areas with easy access. Another very useful technique is Vibroseismics. In this case it is not the aim to create a signal most similar to a delta peak, but a sweep is created. The signal lasts a couple of seconds with variations in frequency. Therefor a plate is pressed onto the ground, vibrating with different frequencies creating a seismogram that only becomes useful after crosscorrelation with the original sweep.

In this study two different sources were used, at the Colle Gnifetti a SISSY (Seismic Impulse Source SYstem), at Halvfarryggen explosives.

SISSY

The SISSY (Figure 8) is an impulse source. The big advantage is its size. The SISSY is a steel tube about 1.26 m long and 50 mm in diameter (www.geosym.de). With a total weight of 10 kg it is very easy to handle and therefore a good source in difficult terrain like Colle Gnifetti. Another big advantage is, that in comparison to conventional explosives it can be used without special permissions. The cartridge of Dynergit is screwed in to the lower part of the pipe. After putting the SISSY into the shot hole it is fixed with help of the packer. Due to the exhausters being on the sides of the cartridge container the energy is not released downward and the device is therefore not pushed out of the hole.

With SISSY one does not carry out a detonation but a deflagration. It is very useful for a survey depth up to 500 m.
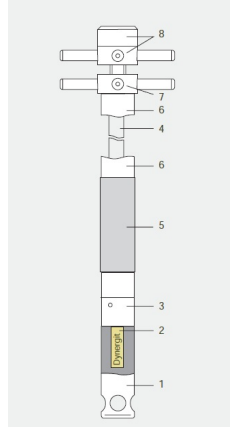
Figure 8: Construction of SISSY: 1-cartridge container with exhausters; 2-cartridge DYNERGIT; 3-cartridge lock with electrical contacts; 4-pipe; 5-packer, 6-distance pipe; 7-hand wheel one to tighten the packer; 8-hand wheel two with electric contacts and female connectors to the fireing device (www.geosym.de)

Explosive

If more energy is needed and deeper surveys are carried out conventional explosives can be used, which cause a detonation. Here a borehole has to be drilled to lower the explosive into that hole. The most common explosives are gelatin dynamite and ammonium nitrate. Mostly one can find them packed in tins or tubes. When using explosives one normally needs special permissions for transport and application and has to stay in a save distance to different things like pipe lines, telephone lines, wells, buildings . . . .

2.2.5   Receiver: The geophone

Today the most common geophone for surveys on land is an electromagnetic one. In this case a moving coil generates a voltage which is then recorded. The geophone itself is placed within a case with a spike that is pushed into the ground for better coupling, so the case can really follow the movement of the ground. The geophone consists of a cylindric magnet with the south pole in the middle divided by a gap of the north pole around it (Figure 9). The streamlines of the field are thereby only varying in radial direction. The coil, which is held by leaf springs, sits within the gap between south and north pole. When the ground moves the case of the geophone and the magnet attached to that is moving, whereas the coil stays in its position, thereby generating a voltage that can be recorded.
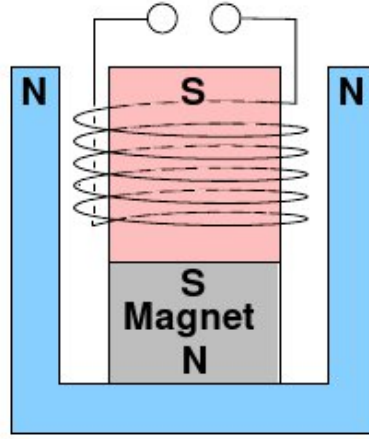
Figure 9: Cylindric magnet of geophone with gap between north and south pole, coil between north and south pole [Forbriger, 2007]

Transfer function of a geophone

The theory of geophone design is treated in detail in Dennison [1951]. To link the displacement of the ground with the recorded voltage of the geophone the following equation applies

$$\frac{d^3I}{dt^3} + \left(\frac{C}{L} + \frac{D}{m}\right)\frac{dI^2}{dt^2} + \left(\frac{S}{m} + \frac{DC}{mL} + \frac{K^2}{mL}\right)\frac{dI}{dt} + \frac{SC}{mL}I = \frac{K}{L}\frac{d^3z}{dt^3} \tag{17}$$

with,

t: time

m: seismic mass

I: current

C: resistant of coil and external circuit

L: inductance of coil and external circuit

D: mechanical damping factor

S: stiffness of spring for suspension

$K = 2\pi rnH$: n - turns of coil, r - mean radius of coil, H - permanent magnetic field.

For a perfectly working geophone the target is that the inductance L is zero. As that can not be reached it is assumed to be sufficiently small and can therefore be set to zero. By that the equation is reduced to:

$$\frac{d^2I}{dt^2} + 2h\omega_0\frac{dI}{dt} + \omega_0^2I = \frac{K}{C}\frac{d^3z}{dt^3} \tag{18}$$

with,

$$2h\omega_0 = \frac{D}{m} + \frac{K^2}{Cm} \tag{19}$$

$$\omega_0^2 = \frac{S}{m} \tag{20}$$

a common harmonic oscillator with driving force and with damping factor h.

The solution without driving force is then given by

$$I = A \cdot exp(-h\omega_0 t) \left[exp(\omega_0 \sqrt{h^2 - 1}t) + exp(-\omega_0 \sqrt{h^2 - 1}t) \right] \tag{21}$$

with the three different cases:

- Overdamped: $h > 1$

- Critically damped: $h = 1$

- Underdamped: $h < 1$

The solution of equation (21) then adds up with the solution for the driving force. An example of the transfer function of the geophone SM 4 is displayed in Figure 10. The SM 4 geophone by the company SENSOR is the geophone that was used for the measurements at Colle Gnifetti and at Halvfarryggen.
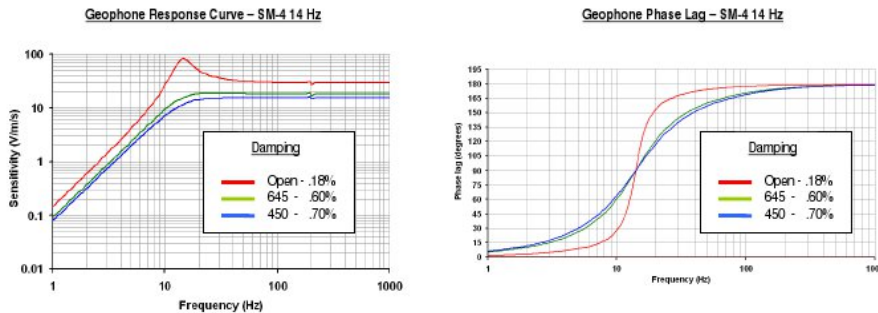
Figure 10: Transfer function of the Geophone SM4, natural frequency 14 Hz, SENSOR

Natural frequency

The natural frequency f_0 is given by $f_0 = \frac{\omega_0}{2\pi} = \frac{1}{2\pi}\sqrt{\frac{S}{m}}$ and is therefore a value of the seismic mass and the stiffness of the leaf springs. There is a shift in phase between the geophone output and the actual signal which is zero at the natural frequency. Above the natural frequency, however, there is little distortion in the phase (Figure 10). Besides that, the sensitivity of the geophone becomes a flat line so that there are little variations in the amplitude response as well. The natural frequency therefore sets the lower limit of the usable frequency band of a geophone. For the used geophone SM4 the natural frequency is 14 Hz.

Spurious frequency

In reality the coil has more degrees of freedom than just in z, in vertical direction. It can as well move a little bit within the horizontal directions or turn because the leaf springs, which hold the coil, are of course not completely fixed (Figure 11.

By that the transient function has discontinuities above the natural frequency. There is more than one discontinuity because of the different degrees of freedom of the coil. The lowest of these discontinuities is called spurious frequency, or parasitic resonance and sets the upper limit of the usable frequency band of a geophone, as it introduces phase shift and a variation in sensitivity. It is thereby a limit set by the construction of the geophone itself.

Common geophones have spurious frequencies around 160 to 180 Hz, but there have been attempts to push these frequencies to higher levels. This is normally accompanied by a higher natural frequency, nevertheless it is possible to build geophones with spurious frequencies up to 900 Hz. If the parasitic resonance is activated it becomes apparent by a long ringing in the seismogram. This ringing can be activated for example by a strong ground roll with high energy [Faber and Maxwell, 1997]. It is very hard to model these discontinuities to be able to calculate them out, as the higher modes are usually unknown.
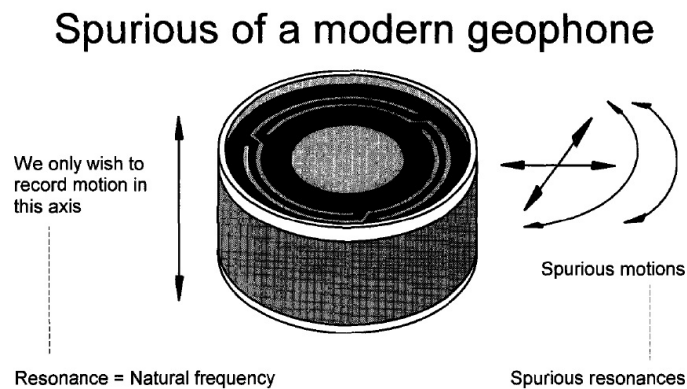
Figure 11: Construction of a geophone with direction of movement for wanted direction as well as spurious movement [Faber and Maxwell, 1997]

3   The field sites

For this thesis two seismic data sets were analyzed. One measurement was carried out at Colle Gnifetti, Monte Rosa, Switzerland and one at Halvfarryggen, Dronning Maud Land, Antarctica.

3.1   Colle Gnifetti

Colle Gnifetti is a glacier saddle in the Monte Rosa massif on the boarder between Switzerland and Italy. It is located between the highest mountains of Switzerland, the Dufourspitze (4634 m), the Zumsteinspitze (4609 m) and next to the Liskamm (4527 m) (Figure 12). The plateau itself lies at round about 4450 m altitude and is the upper accumulation area of the Grenzgletscher. Further down the Grenzgletscher is combined with the Gornergletscher at an altitude of about 2550 m. The Monte Rosa massif mainly consists

Figure 12: Colle Gnifetti in the Monte Rosa massif is the accumulation area of Grenzgletscher (www.schweizmobil.ch)

of gneiss and granites. While the Alps were built, the Adriatic skid of the African plate was pushed into the Eurasian plate (Figure 13). Thereby the Monte Rosa slab was pushed to the top and now builds up the Monte Rosa massif between Schwarzberg-Weisstor and Castor, Liskamm [Labhart, 2001]. With a mean annual air temperature (MAAT) of -14°C the climate conditions resemble very well those in polar regions. Although Colle Gnifetti
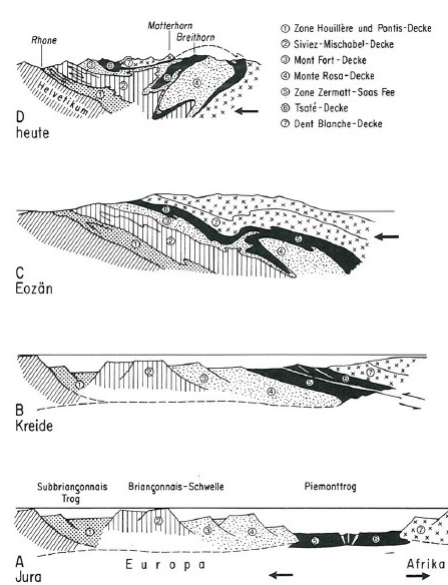
Figure 13: Building of the South-Valais due to the building of the different slaps within the Eocene (C) [Labhart, 2001]

is within the percolation zone only a few, very small ice lenses exist [Eisen et al., 2003]. It is therefore an ideal possibility to test geophysical techniques on glaciers nearby with a low financial and logistic effort.

Colle Gnifetti has been a survey area for decades. It is an amazing climate archive for climate records in industrial areas. Numerous ice cores have been drilled down to an age of the beginning of the Holocene [Haeberli et al., 1988]. Within the boreholes temperature records were taken [Haeberlie and Funk, 1991, Alean et al., 1983]. Besides this radar measurements were carried out [Eisen et al., 2003], ice flow models were developed [Haeberli et al., 1988, Lüthi and Funk, 2000] as well as heat flow models [Lüthi and Funk, 2001]. This makes Colle Gnifetti one of the best studied glaciers in the Alps.

3.1.1   Seismic survey at Colle Gnifetti

In August 2008 a combined seismic and radar survey was carried out on Colle Gnifetti. During this survey two seismic lines were shot (Figure 14). Radar surveys were also carried out along these two lines, so results could be compared in the end. The crossing point of both lines is near the borehole KCI that was drilled in August 2005. This borehole is located at 633999 east, 86554 north and an altitude of 4458 m in the swiss coordinate system (CH1903) measured during the field work in August 2008. The first line was shot in south-north direction, here called line 08001. This line is parallel to the flow line of the
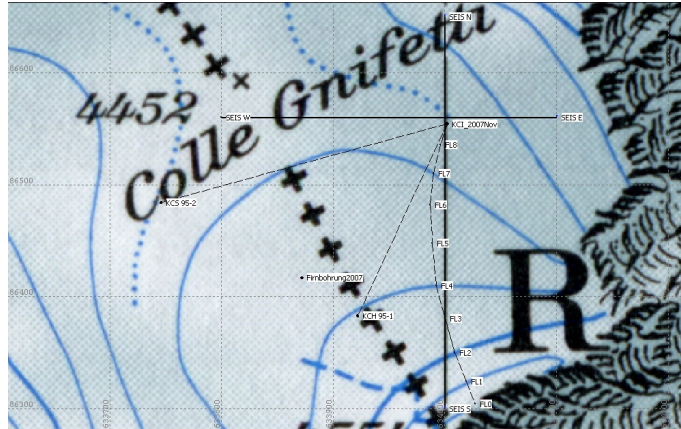
Figure 14: Seismic lines as planned, KCI in the crossing point of the two seismic lines 08001 (south-north) and 08002 (west-east)

glacier ice. The second line, from west to east, is thus perpendicular to the flow line. This line is called line 08002.

In both cases a line of 24 vertical geophones, SM 4 from SENSOR, were laid out. The spacing between the geophones was 3 m giving a spread of 69 (23·3) m. There are 34 shots on line 08001, 33 shots on line 08002. Shot 1 is either the southernmost or the westernmost shot, and is 95 m away from KCI. Shot 2 is 25 m away from Shot 1, so 70 m from KCI, as well as Shot 34 which is 70 m away from KCI on the other side of the geophone line. The other shots are 3 m apart from each other starting 45 m away from KCI and running through the geophone line. In this way a shot was always placed exactly between two geophones (Figure 15). In this way the CMP range from single fold for the first and last
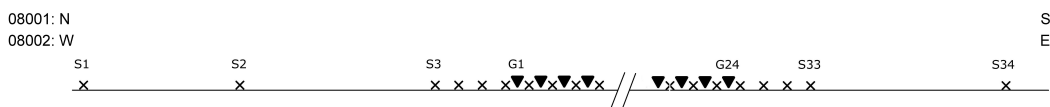
Figure 15: Setup of seismic survey at Colle Gnifetti, line 08002 does not contain shot 34

CMP and up to fold 24 for the CMP in the middle.

The data was recorded with a strataview R24 seismograph for 24 channels. The sampling interval was set to 30 μs to provide a high resolution, with a record length of 256 ms.

The shots were carried out with a SISSY (Seismic Impulse Source SYstem, chapter 2.2.4) in boreholes of about 1 m depth.

Line 08001

24 geophones, 34 shots:

- 3 far offset shots: Shot 1,2 and 34

- 8 shots outside of the geophone line: Shot 3-6, 30-33

- 23 shots within the geophone line: Shot 7-29

The line was shot starting in the middle at borehole KCI moving towards the north first. Afterwards the second branch of the line was shot from KCI towards the south. The files were later renamed so shot 1 is now the southernmost. The borehole KCI lies between shot 12 and 13 and shot 34 is the northernmost.

Line 08002

24 geophones, 33 shots:

- 3 far offset shots: Shot 1,2

- 8 shots outside of the geophone line: Shot 3-6, 30-33

- 23 shots within the geophone line: Shot 7-29

This line was shot starting in the west (shot 1) towards the east. For the processing the shots are still numbered the same way.
Additionally to the shots with the SISSY four shots with a sledgehammer were taken. This did not seem very promising, so that the SISSY data were only used. Problems occurred using the SISSY as the cartridge house ripped open during one shot. More problems were experienced with the electrical connection inside the SISSY because of liquit water.

3.2 Halvfarryggen

Halvfarryggen is a local ice dome in Antarctica. It lies south-east of the Neumayer III, the German Antarctic station, and defines the boundary of the Ekströmisen catchment, the ice shelf on which Neumayer is located (Figure 16). Three ridges come together near the ice dome of Halvfarryggen. As it is located quite close to Neumayer it seemed a suitable site to test the new equipment. From radar data it is known that anisotropies within the ice exist at Halvfarryggen, so it is a place where interesting ice features can be observed. For the planned LIMPICS campaign in January, February 2010 a Vibroseismic truck and

a new RAM Drill should be tested next to the conventional equipment like auger drill and explosives.

On top of the ice dome a 80 m deep ice core has been drilled, DML94, as a preliminary survey for a new drill site within the framework of the International Partnership In Ice Core Science (IPICS). From that ice core density data are available. The position of the
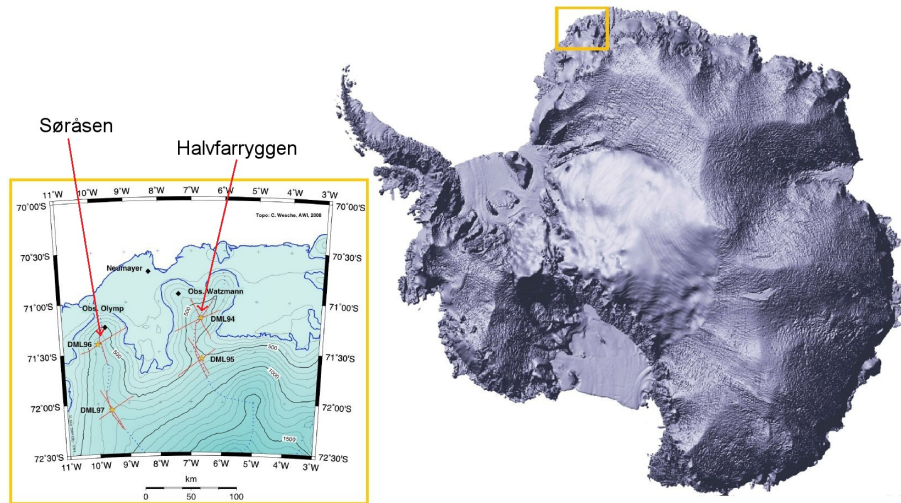
Figure 16: Position of DML94 (Daniel Steinhage, personal communication), location of Halvfarryggen at Antarctica (Coen Hofstede, personal communication)

ice core DML94 is 6.6989° W, 71.1621° S, with an elevation of 690.4 m. A digital elevation model (DML) for the region of Halvfarryggen and Søråsen was developed by Wesche et al. [2009]. Airborne radio-echo sounding (RES) has already been carried out here (Figure 17). The radar image shows the internal layering, anticline and a bulge in the middle, which is known as 'Raymond bump'. Deeper down one can observe the single Raymond bump turn into a double Raymond bump. This behavior can so far only be explained with a change in crystal orientation fabric (COF) [Martin et al., 2009]. COF (chapter 2.1.2) changes as well the acoustic impedance, thus we hoped to observe internal reflections here.

3.2.1   Seismic survey at Halvfarryggen

The seismic survey at Halvfarryggen was carried out in February 2010. Originally, a field season of four weeks was planned. As the ship to Neumayer, that carried the equipment, was delayed this time was reduced to nine days, so the heavy equipment like Vibroseis and a RAM Drill were not taken to Halvfarryggen. Radar measurements were carried out as well. They were taken along the traverse from Neumayer Station to Halvfarryggen and at Halvfarryggen itself (Figure 18).
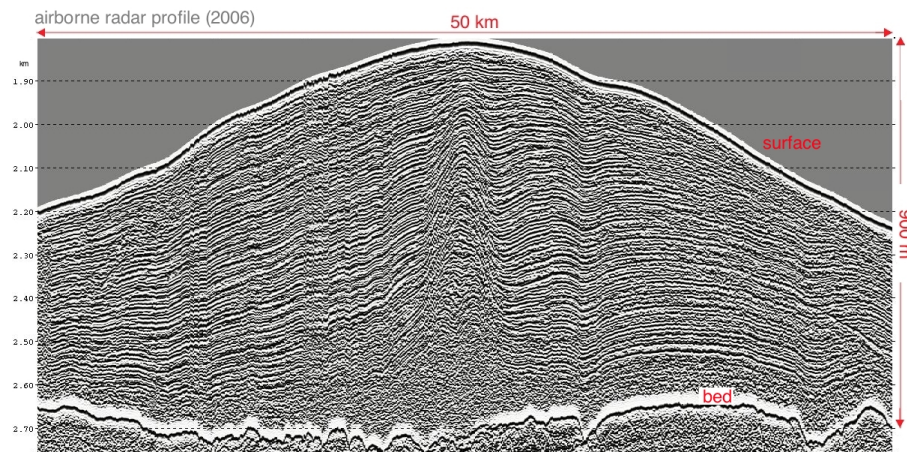
Figure 17: Radio-echo sounding profile across Halvfarryggen with Raymond bump at the center (Daniel Steinhage, personal communication)

The same geophones that were used at Colle Gnifetti were used here as well, recording the data with the strataview R24. The recording length was 2048 ms with a sampling interval of 0.5 ms.

As source explosives were used. 10 shots were carried out, where shot 1 and 2 had a charge of 400 g Pentolite. For the rest of the shots 250 g Pentolite were used, as that seemed enough. Pentolite is an explosive with a mixture of 50 % TNT and 50 % pentaerythritol tetranitrate (PETN).

To deploy the explosives holes were drilled in the firn with help of an auger drill. The boreholes obtained were between 8 and 10 m deep. This had the advantage, that the seismograms still contain very high frequencies, which would otherwise be filtered out within these first meters of the firn pack (Shot 1, chapter 4.4) and the ground roll is reduced.

Due to the delays of the ship the seismic line had to be reduced in length to the originally planned seismic survey. One seismic line of 1490 m was shot. The geophone spacing was 10 m giving a total spread of 230 m. To avoid extra work the geophone line stayed at one location and a shot was once fired at a distance of 265 m and then of 25 m to the first geophone. Afterwards the geophone line was moved, whereas the shot location stayed the same. Hence the next shot was fired at 265 m distance, before moving the shot location again (Figure 19). Thus every hole was used twice (table 1), except the first and last one. This way each shot covers an area of 120 m, with the next shot covering the following 120 m of CDP´s. The data is single fold throughout the record. Shots 2-5 were carried out in 10 m deep boreholes, shots 6-10 in 8 m deep boreholes. For shot 1 there was not enough
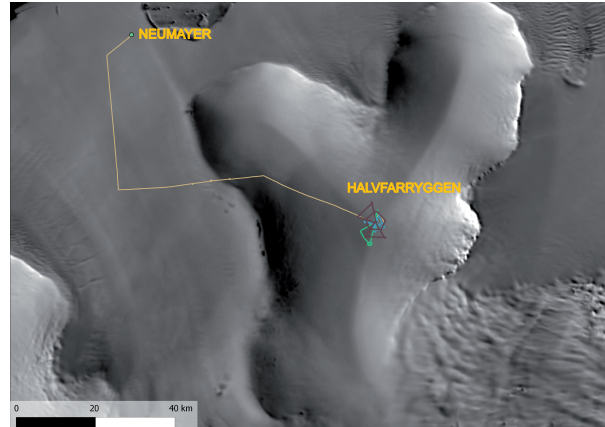
Figure 18: Radar Measurements that were taken at Halvfarryggen, seismic survey was carried out on top of the dome
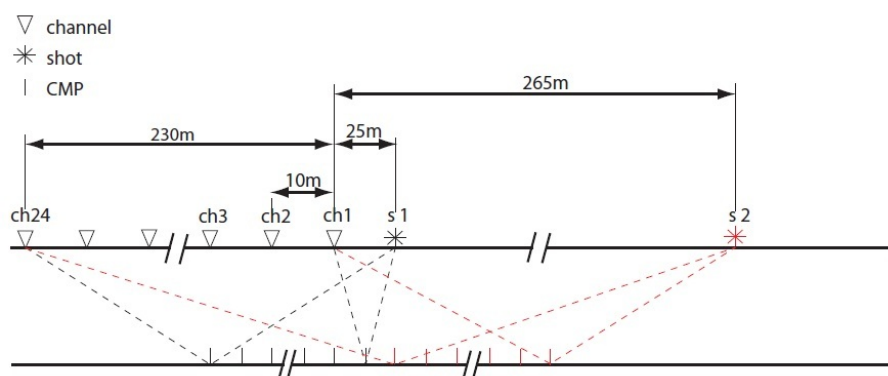
Figure 19: Survey carried out at Halvfarryggen, moving either shot position or geophone line (Coen Hofstede, personal communication)

time so only a 1 m deep borehole was drilled here. This resulted in very poor resolution as all the high frequencies got filtered out by the firn pack and the ground roll dominated. To find the best setting for the shots different ways of preparing the explosives were tried. A plugging was used for the shots 3 and 5 and a detonating cord was used at shot 4, 5, 7 and 9. A list of the different shots, the shot hole number, the distance to the first geophone, shot hole depth, whether plugging and/or detonating cord was used and the covered CDP numbers can be found in table 1.

shot	shot-hole number	offset to first geophone	hole depth	dynamite charge	comments
1	12	265 m	1m	400 g	
2	11	25 m	10 m	400g	
3	11	265 m	10 m	250 g	plugging
4	10	25 m	10 m	250g	sparse plugging detonating cord
5	10	265 m	10 m	250 g	plugging detonating cord
6	9	25 m	8.2 m	250 g	
7	9	265 m	8.2 m	250 g	detonating cord
8	8	25 m	8.2 m	250 g	
9	8	265 m	8.2 m	250g	detonating cord trigger over geophone
10	7	25 m	8 m	250 g	

Table 1: Information about shots taken at Halvfarryggen

4   Processing of seismic data

In this section I present the different processing steps that were used on the Colle Gnifetti as well as the Halvfarryggen data to obtain a satisfying result for the final stack. Not all processing steps that were tested were used in the end. Nevertheless the theory of the tested as well as the used steps is described in the following section. The processing sequences which were used in the end for the two different data sets are described afterwards.

4.1   Processing Theory

4.1.1   Frequency filter

Frequency filters are very common in geophysical data processing to suppress for example unwanted noise. A seismic wave has a frequency band, which is often overlaid by a band of frequencies from noise. To separate the actual signal from the noise, a forward Fourier transformation is carried out so the actual signal $x(t)$ becomes a function of the frequency f (Buttkus [2000]),

$$X(f) = \int_{\infty}^{-\infty} x(t) \exp(-i2\pi f t) dt. \tag{22}$$

Here, every frequency can be described as a sine wave. The whole signal is thereby approximated by a series of sine waves.

Afterwards unwanted frequencies can be filtered out by suppressing certain frequency bands or by the use of bandpass filters to pass on wanted frequencies. Therefore the filter is set to zero for the unwanted frequencies and to one for the frequencies that are passed on, changing them as little as possible. The result $Y(f)$ is then given by the product of the input $X(f)$ and the filter $H(f)$, which would correspond to a convolution in the time domain.

$$Y(f) = H(f)X(f) \tag{23}$$

In reality the frequency is not cut at one exact frequency f_1 so that the filter for example below this frequency f_1 is set to zero and above to one, but a slope is used in between. For the example of a highpass filter, the filter below the frequency f_1 is zero, then there is an increasing slope between zero and one up to the frequency f_2, from where the filter is set to one, so this frequency content is passed on. The slope for the frequency filter is important to avoid unwanted noise induced by the filter, like ringing at the edges of the filter, known as Gibbs phenomenon. The ringing is induced by the discontinuity, a certain jump at the edge of the filter. The discontinuity can only be approximated by a finite number of sine and cosine waves. Due to the finite number the edge can not be described
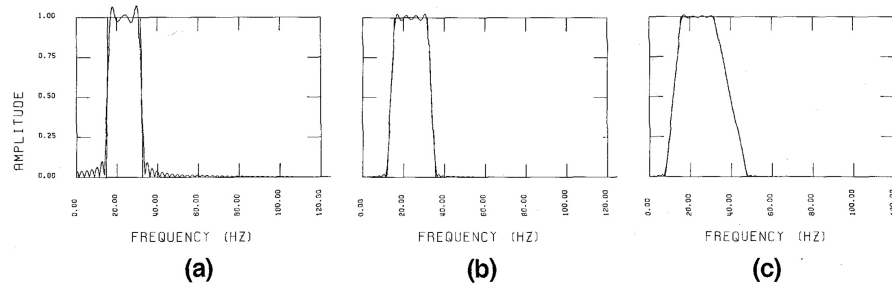
Figure 20: Gibbs phenomenon: (a) without slope, strong ringing at edges; (b) slight slope but still ringing; (c) with slope for frequency filter, ringing reduced [Yilmaz, 1987]

exactly and ringing is induced, which results in the Gibbs phenomenon (Figure 20).

Bandpass filter

Bandpass filters are the most used frequency filters in seismic data processing. Most of the time some low and high frequency noise needs to be cut,

$$H(f) = \begin{cases} 1 & \text{for } f_{min} \leq |f| \leq f_{max} \\ 0 & \text{otherwise .} \end{cases} \quad (24)$$

Here, f_{min} is the lower end where the filter cuts, f_{max} the upper end, so that the frequency in between is passed on.

High-/Lowpass filter

For a highpass filter the filter function is given by

$$H(f) = \begin{cases} 1 & \text{for } f_{cut} \geq |f| \\ 0 & \text{otherwise ,} \end{cases} \quad (25)$$

and for a lowpass filter by

$$H(f) = \begin{cases} 1 & \text{for } f_{cut} \leq |f| \\ 0 & \text{otherwise .} \end{cases} \quad (26)$$

Notch filter

A notch filter is the opposite of a bandpass filter. It gives the opportunity to suppress a small frequency band. When suppling a notch filter one normally chooses one frequency

that should be suppressed. One can however use a bandstop filter as well, where a wider frequency band gets suppressed. The filter function is

$$H(f) = \begin{cases} 0 & \text{for } f_{min} \leq |f| \leq f_{max} \\ 1 & \text{otherwise} \end{cases} \tag{27}$$

4.1.2   Frequency-Wavenumber Filter

Frequency-wavenumber filters (FK-filter) are used to separate events, within the frequency-wavenumber domain, which are coherent in the time-offset domain. Thus they are separated by the different dips of their phase velocities (Figure 21).

The signals are transformed into the frequency-wavenumber domain by a Fourier transformation. The wavenumber is the inverse of the wavelength $k = 2\pi/\lambda$. The phase velocity is given by $v = f\lambda$. By that the phase velocity is as well given by $v = 2\pi f/k$, thus events can be distinguished within the frequency-wavenumber domain by their phase velocity, that means by their different dips. Because of the dispersive nature of the ground roll, this wave should appear as a fan within the FK-domain. Thereby it should be possible to filter out the ground roll with a dip-filter.

4.1.3   Karuhnen-Loève Transformation

The Karuhnen-Loève (KL) transformation is an analysis of the main components of the seismogram. It is a diagonalization of the data set, calculating the eigenvectors. Flat events within a seismogram can be filtered out (Figure 22). The eigenvectors correspond to these flat events. Now it can be chosen if the first two eigenvectors are passed on, or if all the other eigenvectors are passed on. In this way the flat events can be filtered out after the KL-transformation.

To use the KL-transformation a horizontal event is needed in the seismogram. Normally that is not the case, but the traces with bigger offset can be shifted by a constant velocity. Now these created flat events can be filtered out and afterwards the traces can be shifted back to their former position.

4.1.4   Deconvolution

Another possibility to improve the data is by shaping the wavelet using deconvolution. The wavelet is for example shaped into a spike. However this is a very sensitive and complicated method [Yilmaz, 1987].
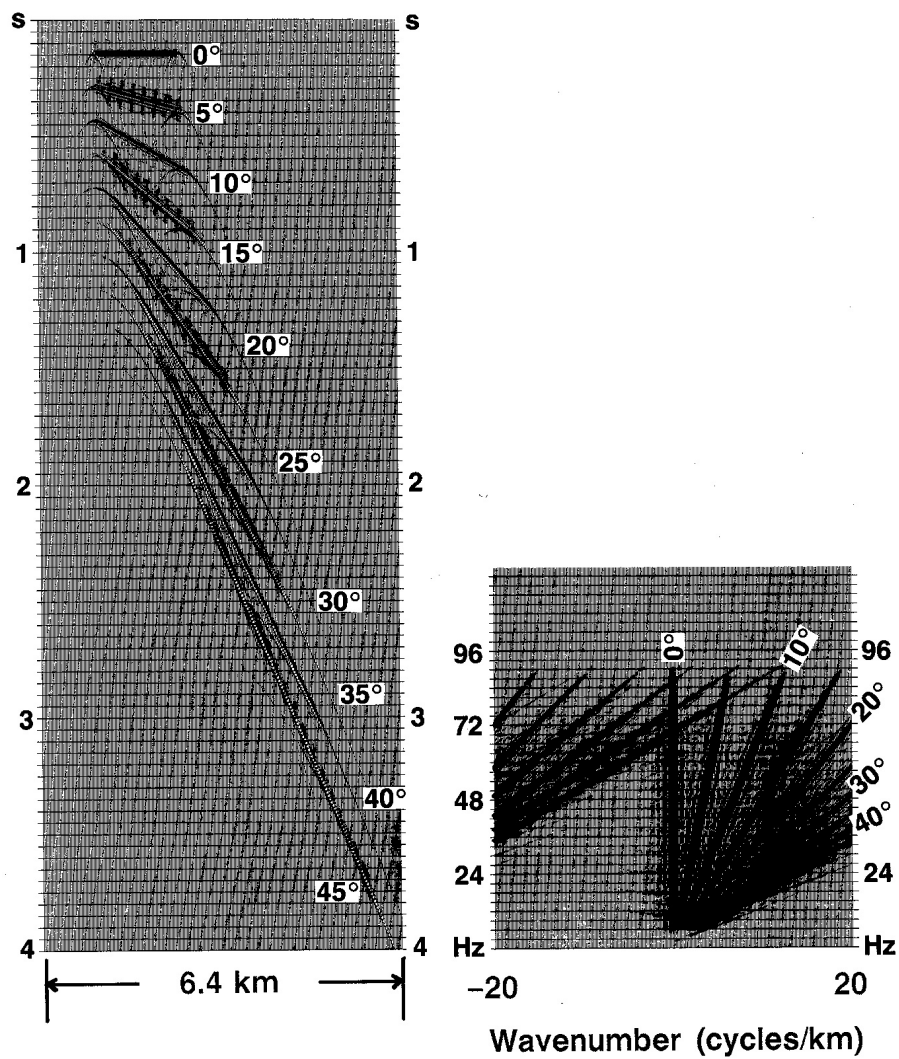
Figure 21: Example for waves with different velocities, and the transformation into the FK-domain. For lower frequencies the steeper dips are aliased. [Yilmaz, 1987]
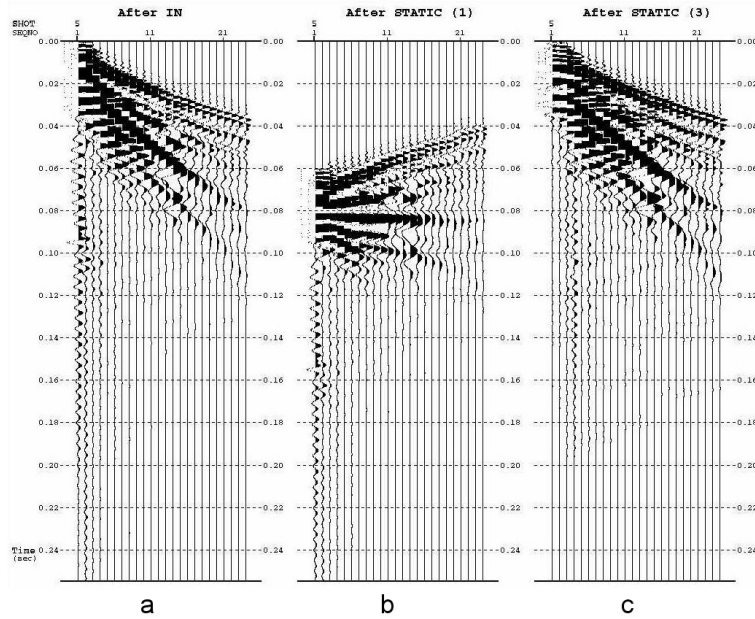
Figure 22: Example for KL-transformation, the traces have been shifted separately (b). The flat event was not filtered out very well (c) compared to the event before filtering (a)

After a shot the wave runs through the ground, gets for example reflected, runs back to the surface and is recorded by a geophone. The resulting seismogram contains all the information about the way. Thereby the initial wavelet of the shot is altered:

$$x(t) = \omega(t) * e(t) + n(t), \tag{28}$$

where $x(t)$ stands for the recorded seismogram, $\omega(t)$ is the initial seismic wavelet, $e(t)$ stands for the earth responds and $n(t)$ contains all the noise. $\omega(t)$ is convolved ($*$) with $e(t)$.

Neglecting noise, the aim is to develop a filter $a(t)$ such that a convolution of the filter with the initial wavelet leads to the earth response,

$$e(t) = a(t) * x(t) \tag{29}$$

by which the initial wavelet gets converted to a spike, at least for spiking deconvolution which was tested here:

$$\delta(t) = \omega(t) * a(t). \tag{30}$$

It is important for a deconvolution that the wavelet is minimum phase, so that the maximum energy is concentrated at the onset.

Besides this, the length of the initial wavelet needs to be known to convert it into a spike.

This is normally not the case. To get an idea about the length of the initial wavelet an autocorrelation of the seismogram is carried out. Now the length of the first wavelet is picked assuming it is close to the initial wavelet length.

Another problem occures in the amplitude spectrum. The operator of the spiking deconvolution is the inverse of the amplitude spectrum. If that amplitude spectrum is zero for a certain frequency the inverse is not defined at that point. To avoid this problem a certain amount of white noise is added. This is called prewhitening.

4.1.5 NMO correction

The normal moveout (NMO) correction is done before stacking the data. After the traces are sorted by common midpoint (CMP) the traces are altered in a way that the travel time hyperbole becomes a horizontal line. This means that the data is corrected for the offset. Therefore the velocity depth profile must be known and the data is corrected in the following way:

$$\Delta t_{NMO} = t(0) \left(\sqrt{1 + \left(\frac{x}{v_{NMO} t(0)} \right)^2} - 1 \right),$$

(31)

with $t(0)$ the vertical two-way travel time and x the offset between shot and receiver [Yilmaz, 1987], (Figure 23). For the velocity v_{NMO} that is used for correction, the root-
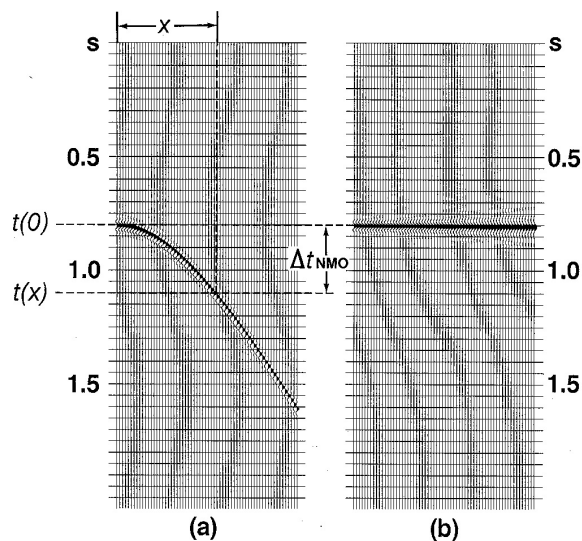
Figure 23: NMO correction, for offset x with time shift $\Delta t_{NMO} = t(x) - t(0)$ [Yilmaz, 1987]

mean-square velocity v_{RMS} is normally used. Therefore a horizontally layered earth model is used. The velocity of each layer i times the travel time in each layer is added up over

all layers N, giving a velocity for correction at each depth,

$$v_{RMS}^2 = \frac{1}{t(0)} \sum_{i=1}^{N} v_i^2 \Delta t_i(0). \tag{32}$$

Too low a velocity would result in overcorrecting, the event is bending upwards. Too high a velocity results in undercorrection, the event is still bending downwards. Thereby the velocity function can be adjusted to get the events lining up for all depths.

When the data get NMO corrected and the traces are lifted, the period of shallow events with big offset get stretched, thereby changing the frequency content to lower frequencies and damaging the shallow events. To get around this problem muting can be used. Hence one defines how much stretching is allowed in percent.

4.1.6   Stack

After the NMO correction the data can be stacked, increasing the resolution by increasing the signal-to-noise ratio. Thereby the amount of data is decreased as well.

All traces that belong to the same CMP are added up. Thus the value of the amplitudes are added up and get divided by the number of traces. The amount of data is reduced as only one trace per CMP is left. When the amplitudes are added up, signals from reflections really add up whereas the noncoherent noise cancels itself out leading to a better signal-to-noise ratio. This makes, of course, only sense when the data is more than single fold.

Median stack

A median stack works just like a stack, the difference is the way the amplitudes are added. For the normal stack the average of the amplitudes over the individual traces is used, for the median stack the median of the amplitudes is used. That means that the amplitude that occurs most often becomes the amplitude of the stacked trace, resulting in a different way of scaling the amplitudes.

4.1.7   Poststack Processing

Some of the filters that are used before stacking can as well be used after stacking, like the FK-filter or the deconvolution. Although, this is not very common Benjumea and Teixidó [2001] and Levato et al. [1999] showed that it can improve data from seismic measurements on glaciers significantly.

4.1.8 Migration

Migration is an important part in processing of seismic data. After stacking an image of the subsurface can be seen. This image is not correct yet. Dipping reflectors have the wrong angle or smaller structures are imaged as diffractions.

The wave field which was recorded at the surface is now converted to depth, using a velocity profile. By that diffractions collapse and dipping events are moved to their correct angle. Different methods of migration are known, like Phase-Shift-Migration or Kirchhoff-Migration. As seen later, the reflectors from Colle Gnifetti as well as Halvfarryggen are very flat. Because flat events are already displayed correctly, no migration was carried out here.

4.1.9 Depth conversion

The final step is then to convert the two-way travel time (TWT) of the stack into depth. Therefore the RMS velocities (equation 32), that where as well used for the NMO correction, are used. With help of the RMS velocities and the travel time the corresponding depth can be calculated and thus the depth of a reflector can be gained.

4.2 Processing of the Colle Gnifetti data

During processing it became clear that the Colle Gnifetti data set was not easy to filter because of difficulties which occurred due to the shot-receiver geometry that was used. The bed reflection, which we are interested in, is overlain by different waves, like refracted waves, diving wave, or ground roll (Figure 25). As some of these waves have a very similar frequency content as the bed reflection, frequency filters were more or less useless. The frequency content of the reflection, between 20 and 240 Hz, is known from shot 34, where it was possible to filter out the bed reflection (Figure 26). Due to spatial aliasing of the ground roll filtering in the FK-domain induced a lot of noise and could not be used either (Figure 27 and 28).

More problems occurred due to ringing in the near offset traces because of parasitic resonances. The final processing flow (Figure 24) contains one prestack and one poststack frequency filter and the near offset traces were killed. In the end I could achieve the best result by applying a poststack FK-Filter to the data like recommended by Benjumea and Teixidó [2001]. The different steps are explained in detail in the following sections. All the processing was carried out with the program FOCUS.
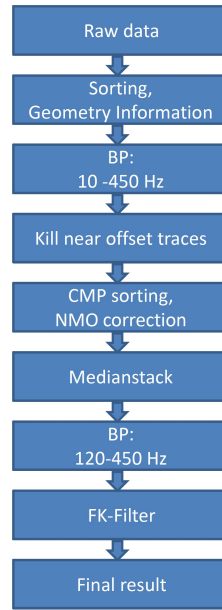
Figure 24: Final flow for processing of the Colle Gnifetti data set

The Colle Gnifetti data set can be split into three ensembles due to similar problems in the processing sequence. In all cases the different wave types with similar frequency contents were overlaying each other (Figure 25).

- Far offset shots: Reflection could be filtered out with help of an FK-filter (Figure 26).

- Near offset shots: Spatial aliasing of the ground roll occurs.

- Shots within the geophone line: Strong ringing due to parasitic resonances, spatial aliasing of the ground roll (Figure 27, 28).

4.2.1   FK-filter

KF filtering was applied by using the FKFILT command of FOCUS, which opens an interactive window. Here one is able to choose the filter interactively, to filter a dip or polygon in the FK-domain. I tried this for all ensembles of shots (far offset, outside line, within line). Thereby shot 34 turned out to be very useful. Here it was possible to filter out the refracted wave as well as the ground roll to recover the reflected P-wave. For the shots outside the geophone line, spatial aliasing occurred within the data because of the very slow ground roll, making it impossible to filter within the FK-domain. By using the FK-filter a lot of noise was induced and no advantage was gained from this approach.
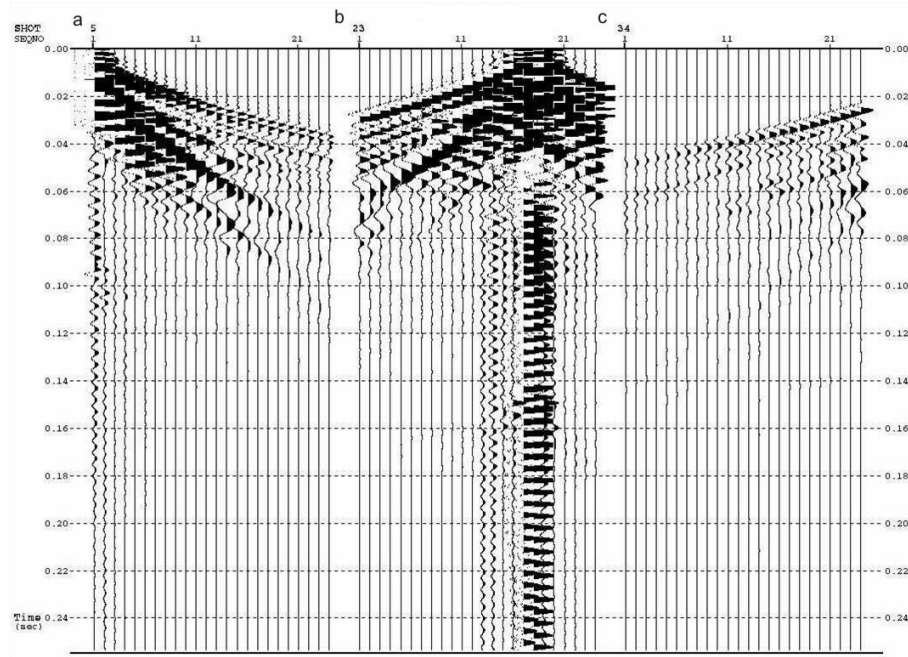
Figure 25: Raw shots: a - near offset, b - within geophone line, c - far offset
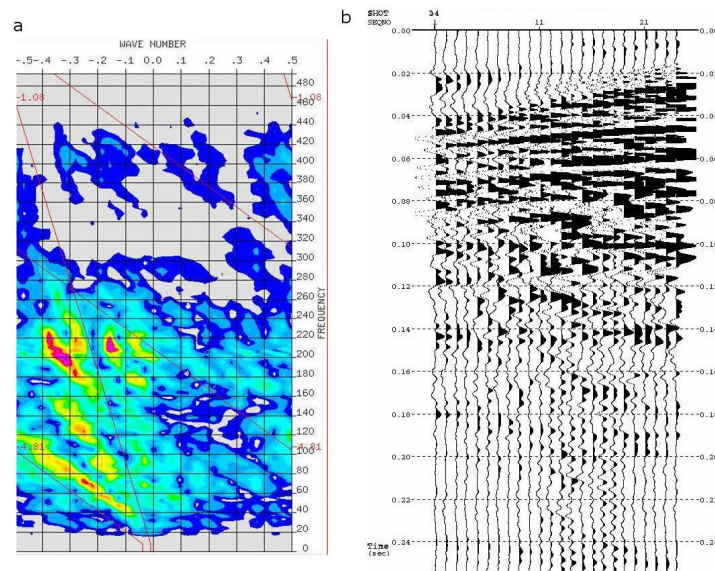
Figure 26: Shot 34, FK-domain with used dip filter, result with bed reflection just below 0.04 s
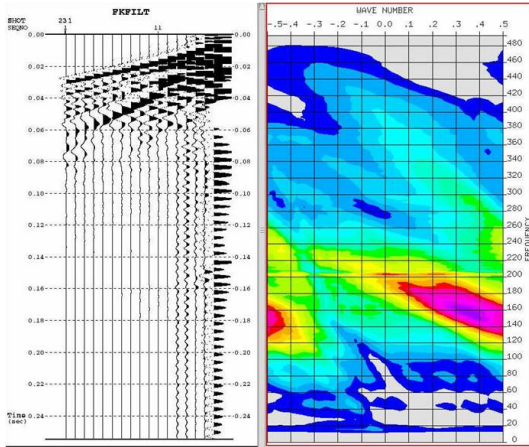
Figure 27: Split shot 23, line 08001, traces south of shot, with FK-spectrum and spatial aliasing of the ground roll
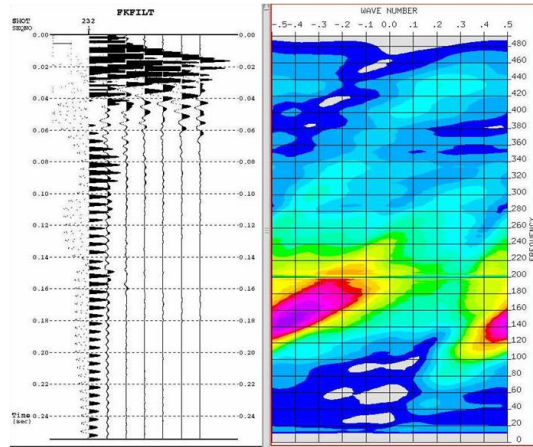
Figure 28: Split shot 23, line 08001, traces north of shot, with FK-spectrum and spatial aliasing of the ground roll

An additional problem occurred for the shots within the geophone line. Here the waves were running in opposite direction from the shot, so that high amplitude signals were observed in the positive, as well as the negative FK-domain. The best seemed to be to split the data at the shot point. This led to a similar problem like the one for the shots outside the line, spatial aliasing of the ground roll and was therefore not used in the end.

4.2.2 KL-transformation

To remove the refracted wave before FK filtering, the KLTRANS command was used. The arrivals of the direct wave were first shifted to a horizontal line by using a constant velocity for the RVMO command.

Because of the densification of the snow, the arrivals of one wave do not occur as a straight line, but as a bent one, making it impossible to generate a straight, horizontal line to be removed by the KL-transformation when using just one velocity to lift the traces (Figure 29). I tried to use the same procedure to remove the ground roll, with the same problem of bending. Besides that a second problem occurred here. Because of the very slow velocity of the ground roll, the earlier arrivals, like diving waves and reflections of the far offset traces were lifted above zero seconds. Here FOCUS just cuts away these signals.

To avoid this problem all traces were first shifted down 60 ms and shifted back up again after the KL-transformation (Figure 22). To avoid the problem of bending, I lifted every trace separately by a time that I picked before by hand. Nevertheless the ground roll could not be removed by this approach, although it was lining up straight now.
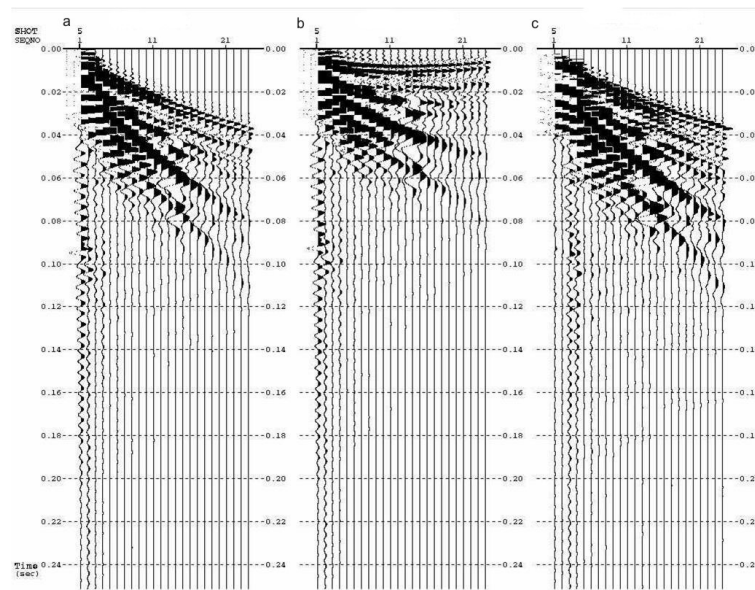
Figure 29: Lifting traces with one velocity (b), where bending can be observed. As the wave does not line up straight it can not be filtered out, compare before filter (a) and after filter (c)

Lifting every trace individually was also used to get the direct wave to line up horizontally. But here as well, the KL-transformation did not remove the refracted wave. That the wave was not filtered out, although it was lining up, might be because the wave was not very coherent.

4.2.3 Frequency filter

Different frequency filters were tried to achieve a satisfying result. As the different waves all had a very similar frequency content it was difficult to improve the data with frequency filters.

Highpass filter

Using a highpass filter for the shots outside the geophone line to remove the ground roll resulted in a lot of negative energy for positive incoming waves. The filter had to be set as high as 160 Hz to remove the ground roll. The problem is that the frequency of the reflection is between 20 and 240 Hz, which is known from shot 34. By using a highpass filter as high as 160 Hz to remove parts of the ground roll the actual reflection gets affected as well. The filter was therefore not of use.

Notch filter

At the near offset traces (offset 1.5 m) ringing could be observed (Figure 25, b). This ringing is due to parasitic resonances (chapter 2.2.5, Figure 30). The observed ringing has high amplitudes and can be observed around 205 Hz. I tried to remove this signal with help of a notch filter. Thereby the frequencies of all traces were changed enormously,
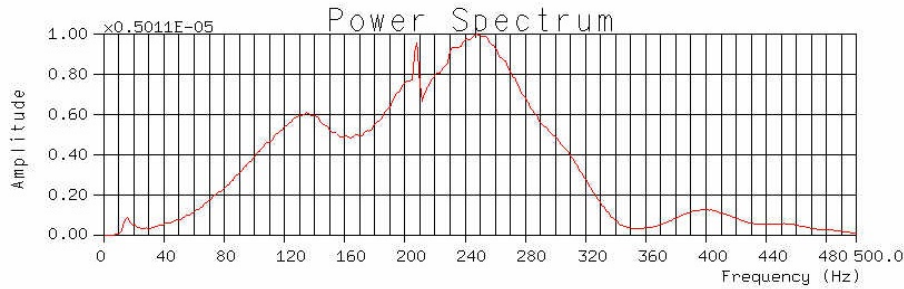
Figure 30: Parasitic resonance at 205 Hz in line 08001, shot 13, offset 1.5 m

resulting in a lot of noise. The other problem was that the expected signal of the reflection is at a similar frequency. This made it absolutely impossible to remove this kind of noise. Also a very narrow Bandstop (BS) filter was not of use because of the similar frequencies of the ringing and the reflection. Nevertheless, using a narrow BS-filter resulted only in a big frequency gap, not in a shift of frequencies. So neither of the two filters was used to reduce the ringing.

4.2.4   Trace killing

To improve the quality of the data and get rid of the ringing at the traces closest to the shot, the whole traces with offset 1.5 m were removed. The high amplitudes caused a lot of noise when stacking the data, and no advantage was gained from these traces anyway, so removing them seemed a reasonable step.

4.2.5   Stack

Filtering the data before stacking was not very successful. A wide bandpass filter was used with a lower ramp of 0-10 Hz and an upper ramp of 450-500 Hz, thereby getting rid of everything below the natural frequency of the geophone and the high frequency noise. Additionally the near offset traces were removed in order to remove the ringing. Afterwards the data was CMP sorted, NMO corrected and finally stacked. It became clear that a median stack enhanced the result. The used velocity model for the NMO correction was obtained using the density data from the ice core KCI (Figure 2). From this
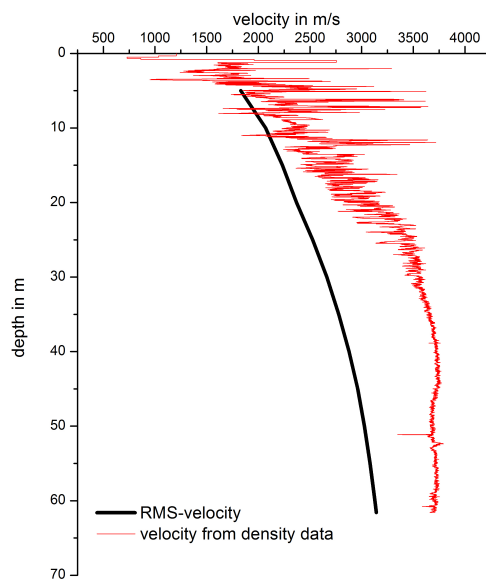
Figure 31: Velocity profile calculated from density data from KCI (red) and used RMS-velocities calculated from these velocities

density data, I calculated the P-wave velocity using the empirical formula by Kohnen [1972] (chapter 2.2.1). The velocities were averaged over five meter intervals. For the velocity file of FOCUS, I then calculated RMS-velocities (equation 32) from these averaged velocities (Figure 31).

4.2.6 Poststack Filter

Some filters can as well be applied after stacking. This proofed essential for the Colle Gnifetti data to be able to see the bed reflection.

FK-filter

As was recommended in the paper by Benjumea and Teixidó [2001] a poststack FK filter was applied to the data. A dip filter around the wavenumber $k = 0$ improved the data enormously. Now it was possible to separate the bed reflection from the noise. But it was still impossible to see any reflections from within the ice.

Poststack frequency filter

An improvement of the data was achieved with a bandpass filter of 100-120 Hz lower ramp
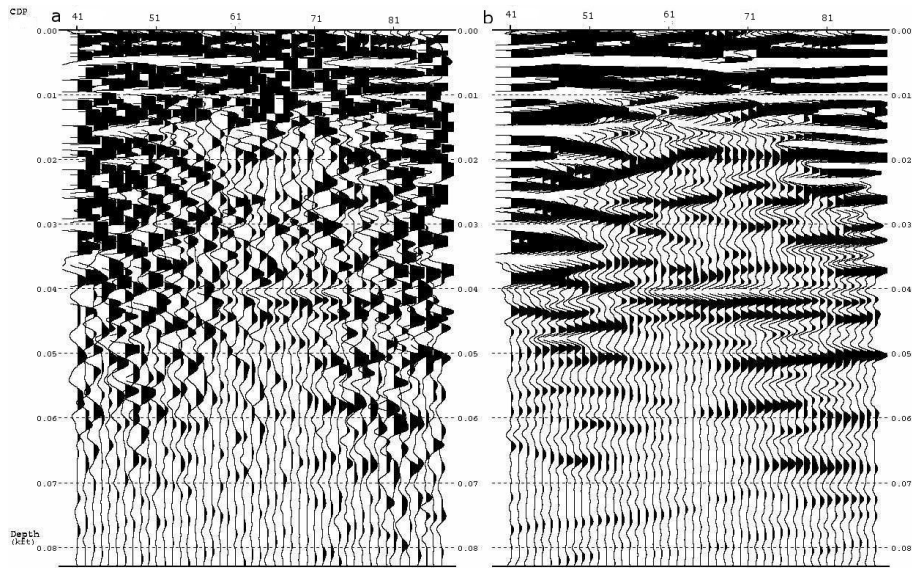
Figure 32: Line 08001 before (a), and after (b) FK-filter, bed reflection at 0.04 s (for line 08002 see appendix A.2)

and 450-500 Hz upper end. The FK-filter after stacking induced again some noise, nevertheless it improves the quality of the data significantly (Figure 32). Some of the induced noise can than be suppressed by a subsequent frequency filter.

Front mute

A lot of noise could still be observed before the reflection because not all refractions and ground roll could be removed before stacking. To improve the data furthermore and get rid of the confusing signals in the first few meters a front mute was used. The front mute resulted only in a hole without signals in front of the reflection, but could not really remove this noise. It was therefore not used for the final result.

Balance

It was also tried to balance the amplitudes of the traces, to reach a better level between the really high amplitudes of the refracted waves and the bed reflection. This resulted in an increase of amplitude before the reflection, making it impossible to pick the reflection any longer and was therefore not used for the final result either.

Deconvolution

Deconvolution was tried on prestack data as well as on poststack data. Levato et al. [1999] received very good results with the approach of an poststack deconvolution. In both cases

the results were not convincing, so that deconvolution was not used for the final result. This was probably due to the very bad signal to noise ratio in this data set.

4.2.7   Depth conversion

The final result for the two lines from Colle Gnifetti was obtained by carrying out a depth conversion with help of the velocity model obtained from KCI. Within these results a lot of noise still remained, that could not be filtered out. For the final result only those CMP's with fold ≥ 6 where used, as they have a better signal to noise ratio. Nevertheless it was only possible to see the bed reflection for 69 m on line 08001 and 67.5 m on line 08002 (Figure 39, chapter 4.5).

4.3   Spurious frequencies

Ringing could be observed in the Colle Gnifetti data as well as the Halvfarryggen data. This ringing was very strong in the Colle Gnifetti data at about 205-208 Hz and could be observed as well in the Halvfarryggen data. The cause of spurious frequencies was explained in chapter 2.2.5. The used geophone and the consequences for the data sets are discussed in the following sections.

4.3.1   Geophone type

To confirm that the observed ringing is due to parasitic resonances the measured spurious frequency was compared to the given spurious frequency of the manufacturer. This turned out to be quite difficult. There was no information about the type of geophone available. The only thing known was the natural frequency with 14 Hz. After consulting the manufacturer there were still three different geophones in question, all by the dutch company SENSOR:

- SM-4/U-B 14 Hz: Spurious frequency 190 Hz

- SM-15/U-B 14 Hz: Spurious frequency > 500 Hz

- SM-7/U-B 14 Hz: Spurious frequency 420 Hz

Because of our measurements it is very likely that the geophone in question is the SM-4. Here the given lower limit for the spurious frequencies of 190 Hz fits very well to the apparency of the parasitic resonance at a frequency just above 200 Hz.
Unfortunately we could not use the geophone data to confirm the frequency of the ringing

Figure 33: Colle Gnifetti, line 08001, shot 14, offset 1.5 m, spurious frequency 210 Hz and 225 Hz

as spurious frequency. Nevertheless it gives an important hint that the geophone in use is very likely the SM-4 geophone.

4.3.2   Influence of spurious frequencies to seismic data

As explained in chapter 2.2.5 spurious frequencies induce phase shift and variation in amplitude. If the resonance is activated, ringing can be observed like we see it in the Colle Gnifetti data as well as in the Halvfarryggen data. In both cases one mode gets activated probably due to the strong ground roll just above 200 Hz. In the Colle Gnifetti data a second mode can be observed at certain shots at about 225 Hz (Figure 33).

This ringing disturbs the data enormously. It could be filtered out with a notch filter of 206 Hz for the Halvfarryggen data and could only be reduced by killing the near offset traces in the Colle Gnifetti data. Getting rid of the ringing improved the data, and dealt with the biggest problem for the processing sequences, the disturbance of such a high amplitude. It was especially not a good idea to use an FK-filter that would cut through the signal of the ringing, as this induced a lot of noise. Nevertheless the problem of phase shift and variation in the sensitivity of the amplitude still remains. The observed frequency is just the first mode. Higher modes like the one at 225 Hz exist, inducing phase shift and variation in the sensitivity of amplitudes as well. As nothing is known about those frequencies they can neither be filtered out nor modeled.

When analyzing the data it should be kept in mind that the data from Colle Gnifetti and

Halvfarryggen could be phase shifted or could vary in the sensitivity. It would of course be better to use geophones with a higher spurious frequency. Also care has to be taken here, that the natural frequency is not too high, causing problems with the low frequencies.

4.4   Processing of the Halvfarryggen data

At Halvfarryggen the same geophones but more powerful sources were used as on Colle Gnifetti. Because of the different shot-receiver geometry and the much thicker ice, processing was a lot easier and reflections from within the ice could be observed.

Different setups for source deployment and triggering were tested. This leads to a very different quality from shot to shot (Figure 34) and furthermore to a processing sequence which varies a little for the different shots. The differences in the shooting were described in chapter 3.2.1. The main structure of the filtering for all the shots remains the same, the differences are in the exact values of the filter parameter. Shot 1 is very different from all
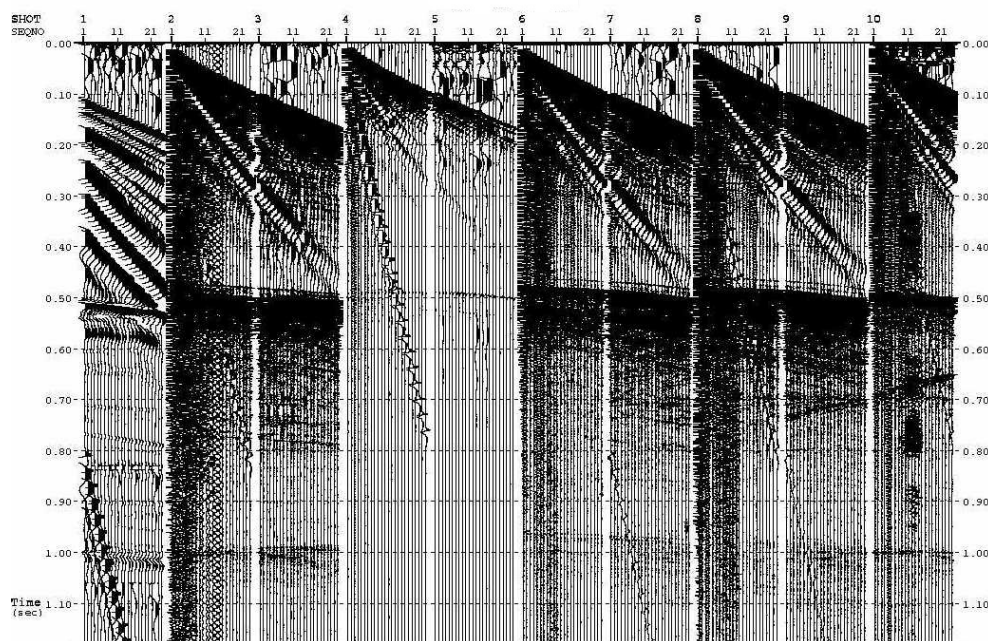
Figure 34: The raw shots 1-10, unprocessed

other shots. This shot was placed in a 1 m deep borehole, instead of a 10 m deep one. The effect was, that the high frequencies were attenuated within the first few meters of the firn pack. Thus we are missing a high resolution in our data, no frequencies higher than 80 Hz and no internal layers can be observed, although the bed is visible. As this shot is so very different in its frequency content it was not used any further.

Also problematic were shots 4 and 5. At shot 4 the plugging was pushed out slightly.

Shot 5 is shot in the same borehole, after shot 4 was shot. That might have caused the problems. These two shots had to be handled a bit different than the rest of the shots. The differences in processing are as well explained in the next sections.

4.4.1   Muting

Strong refractions are found within the first milliseconds of the shots. These were removed with a front mute as they could not be filtered out differently and the strong amplitudes suppressed the following signals.

Additionally, a front mute was used on shot 4. Here the problem of an air wave with very strong amplitudes and a velocity of around 320 m/s occurs. This wave could be weakened with a HP-filter, but the rest, down to the reflection, was afterwards removed with help of a front mute. An additional front mute was as well used on shot 5 to get rid of remains of refracted waves, that had not be removed with the first front mute in the case of this shot.

4.4.2   Frequency filter

For all shots a notch filter as well as a highpass filter were used.

Notch filter

As the same geophones were used at Halvfarryggen as on Colle Gnifetti, the problem of parasitic resonances occurs here as well. The parasitic resonance is activated for the near offset traces, up to about 125 m offset, at 206 Hz. In the case of the Halvfarryggen data, the notch filter worked fine.

FOCUS gives the possibility to choose between applying the notch filter once or twice. Running it just once does not suppress the chosen frequency completely. Nevertheless it weakened the 206 Hz ringing enough, so that the disturbance of the parasitic resonance was of no importance any longer (Figure 35). The only shot where no 206 Hz notch filter was needed, was shot number 5. In shot 4 however it was not enough to apply the 206 Hz notch filter just once, here it had to be applied twice to suppress the noise sufficiently.

Shot 2 had another anomaly at about 79 Hz, where the notch filter was applied once as well. It is still unclear what caused this strong signal at the frequency of 79 Hz, but it was filtered out very successfully by the notch filter.

Highpass filter

To get rid of the ground roll, it was necessary to use a low HP filter. For most shots (shot
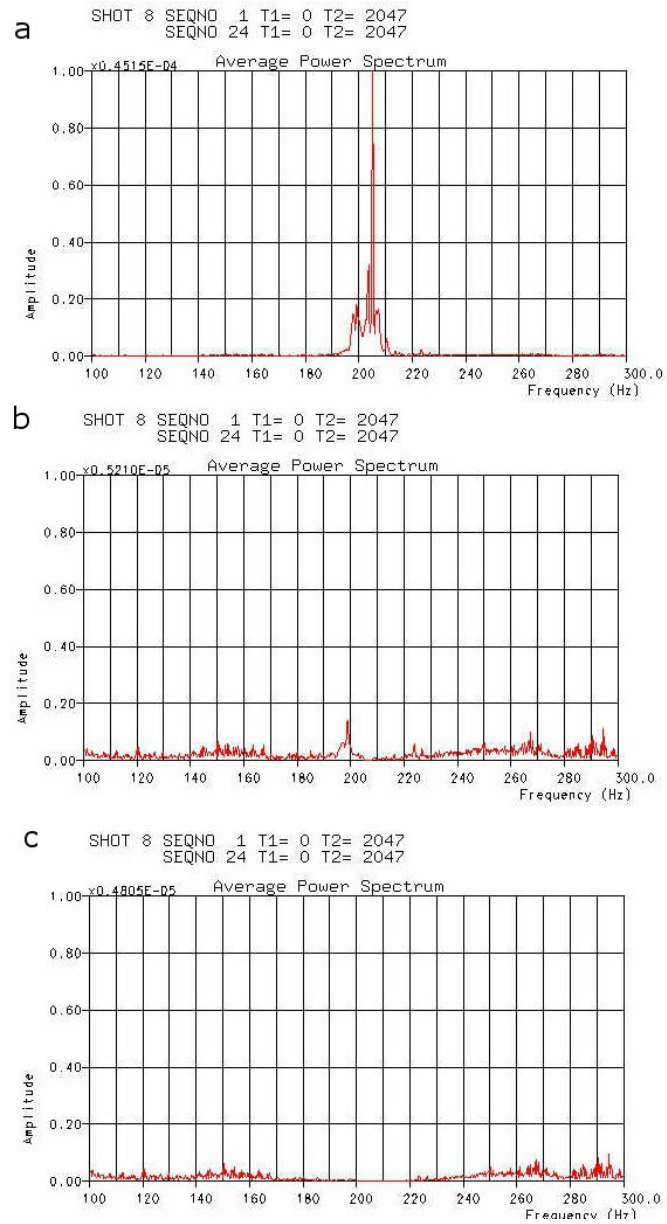
Figure 35: Used notch filter for spurious frequency of 206 Hz, a - without notch filter, b - notch filter applied once, c - notch filter supplied twice

2-3 and 7-10) this HP-filter has a ramp of 40-50 Hz. Thereby not all of the ground roll could be removed. For shot 4 and 5 the HP-filter is a bit lower, 20-30 Hz. In shot 4 the biggest problem is not the ground roll, but the air wave that was then partly removed with help of a frontmute. Nevertheless the low HP-filter helped to weaken the air wave.

4.4.3   FK-filter

To remove the ground roll completely and to get rid of some noise, the FK-filter proved very effective. As all of our reflectors are more or less flat, a dip filter around the wavenumber zero worked very fine (Figure 36). The reflections were passed on. The ground roll as well as parts of random noise were suppressed. This is very good, as our data is single fold and no stacking is going to improve the signal to noise ratio any further. The same dip FK-filter worked very good on shot 2, 3 and 7-10. On shot 4 and 5 the FK-filter had to be adjusted a little bit.
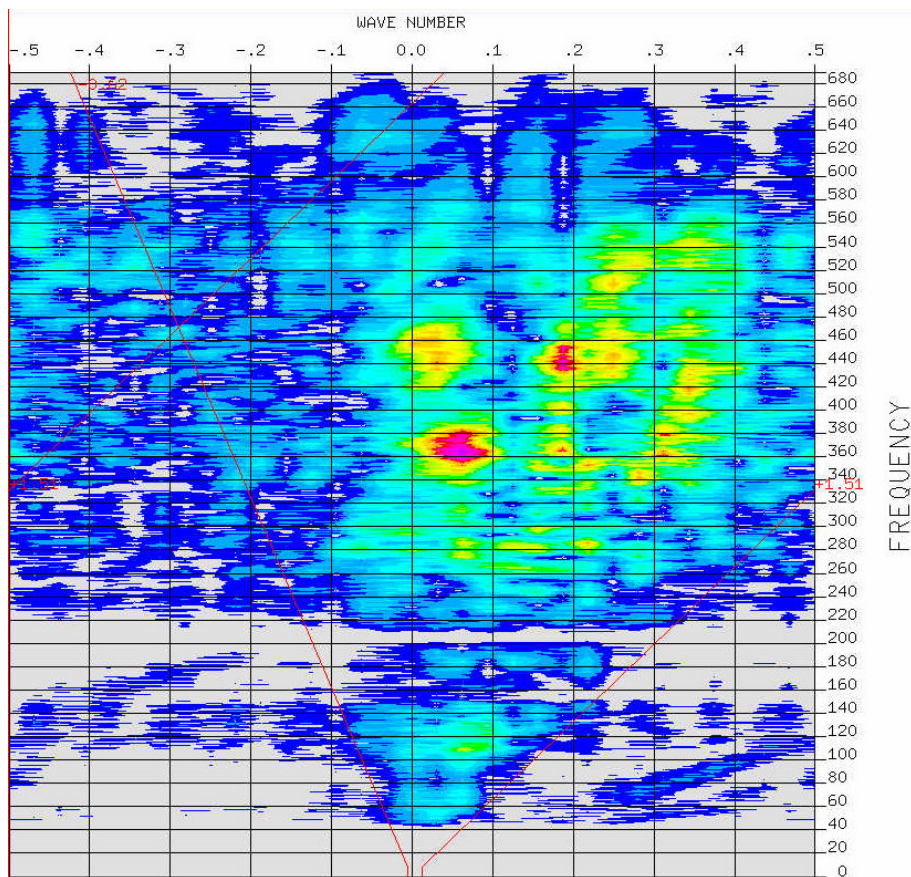
Figure 36: Example for dip filter used for filtering in the FK-domain (Shot3)

4.4.4 KL-transformation

As for the Colle Gnifetti data, a KL-transformation was not very useful to remove the ground roll or air wave. On shot 4 the FK-filter induced some noise due to the not completely removed air wave after the bed reflection. This noise was lining up completely flat just underneath the bed reflection and could be filtered away with help of a KL-transformation. This KL-transformation did not affect the bed reflection, as the bed reflection is slightly hyperbolic.

4.4.5 Static corrections

On two shots I performed static corrections. Shot 3 and shot 7 were shifted upwards by 1 ms. Why shot 3 was delayed is unclear. Shot 7 was shot with help of a detonating cord in a 8 m deep borehole. With a donation velocity of 8400 m/s in an 8 m deep borehole a delay of 1 ms fits very well.

4.4.6 NMO - Velocity model

For the velocity model I used density data from the core DML94 down to a depth of 83 m. From this density data I calculated P-wave velocities with help of the Kohnen formula (chapter 2.2.1). Afterwards, I fitted an exponential function to the data and extrapolated the velocity to greater depths (Appendix A.3). From these velocities the RMS-velocities were calculated afterwards and inserted into FOCUS. This velocity function was then adjusted a little bit, so the bed reflection would line up (Figure 37). With this velocity function the NMO correction was then carried out. As the data is single fold no stacking had to be preformed.

4.4.7 Gain

Due to geometrical spreading the amplitudes decrease. This effect is large here because of the large offsets. To correct for this, an offset dependent gain control is carried out. Therefore the same velocity model as for the NMO correction was used to correct for the geometrical spreading.

4.4.8 Poststack Processing

Poststack processing proved essential for the Colle Gnifetti data It was tried as well on the Halvfarryggen data set. Using deconvolution after stacking increased the quality of
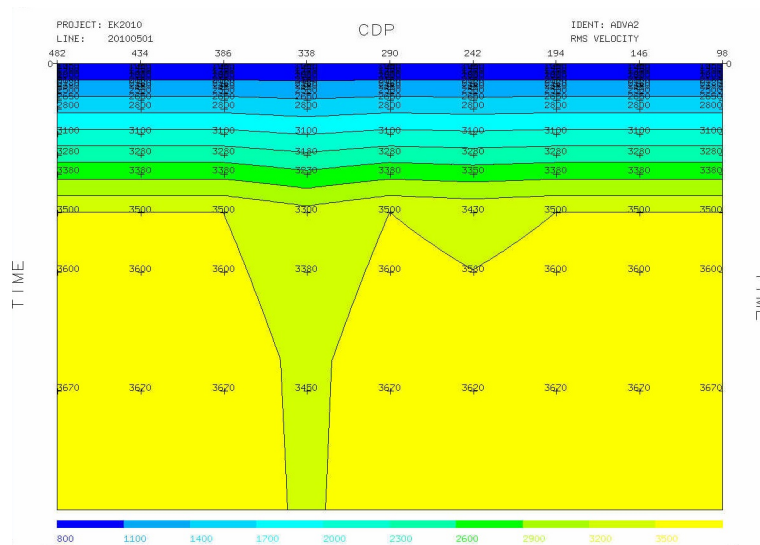
Figure 37: Velocity model used for NMO correction, adjusted at certain points. The low velocity zone, CMP 338 is between shot 4 and 5, the weak shots

the bed reflection. Unfortunately it distorted the internal reflections from the ice as the signal-to-noise ratio is not that good here. FK-filtering just induced a lot of noise and was therefore not of any use in the case of the Halvfarryggen data.

Afterwards I also used the depth conversion function from FOCUS. This function works with the RMS-velocities that were used for stacking as well. Because of the stretching after NMO, due to the bigger offsets and the shallow reflections, that we are interested in, this depth conversion did not work very well. It bent the far offset reflection upwards. Therefore it is not used, but we can still extrapolate the approximate depth from that. The final stack is presented in chapter 4.5.3.

4.4.9   Processing for AVO

AVO analyses of the reflectors from within the ice were carried out. When doing an AVO analysis the relative amplitude of the reflection should not be changed. So care has to be taken when processing data for AVO or AVA.

To determine if the different processing steps have an unwanted influence on the amplitude I picked the amplitude after each processing step for the shots 6 and 7. The amplitude was always picked after NMO-correction and after a gain control correcting for the geometrical spreading. This correction is important to correct for the offset dependent decrease in amplitude [Resnick, 1993]. Besides this the shots were scaled with the help of the diving wave (chapter 5.2.1)

Figure 38 shows the change in amplitude after the different filtering steps. The black points are the amplitudes after front muting and gain control. Afterwards the data was notch filtered (red) and than additionally frequency filtered (blue). The final step was a FK-filter (green). As the changes in amplitude that were induced by filtering were very small the data was filtered completely before picking the amplitudes for the other shots.
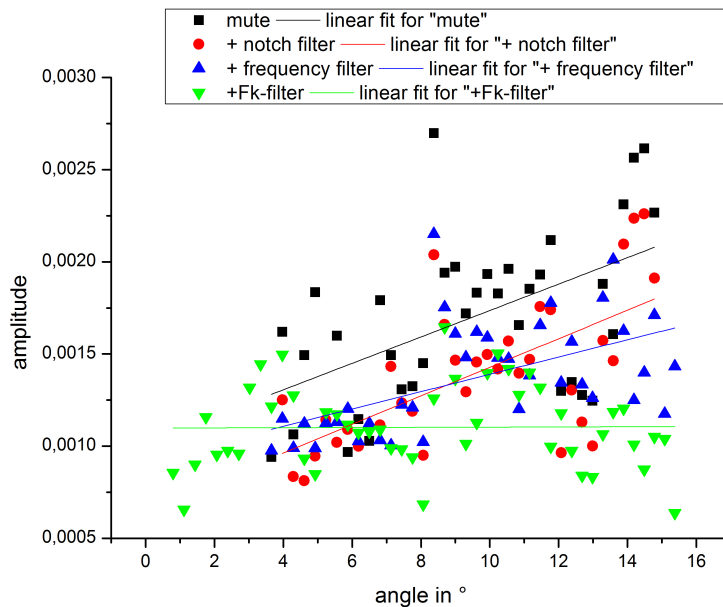
Figure 38: Change in amplitudes after different processing steps

4.5   The final stacks

The aim was to process the data from Colle Gnifetti and Halvfarryggen to be able to see reflections from within the ice. After all the different processing steps were tried and some of them used, internal layers could be observed in the final stack of the Halvfarryggen data. Filtering out internal reflections was not possible for the Colle Gnifetti data, but the bed reflection can be seen in the final stacks.

4.5.1   Colle Gnifetti result

As described in chapter 4.2 it was not easy to process the Colle Gnifetti data. The primary aim to detect reflections from within the ice was not reached. Although it is still not clear if they do exist at Colle Gnifetti. Filtering out the bed reflection was already a challenge. For the final stacks (Figure 39) only these CMPs were used that have fold equal or bigger than 6.
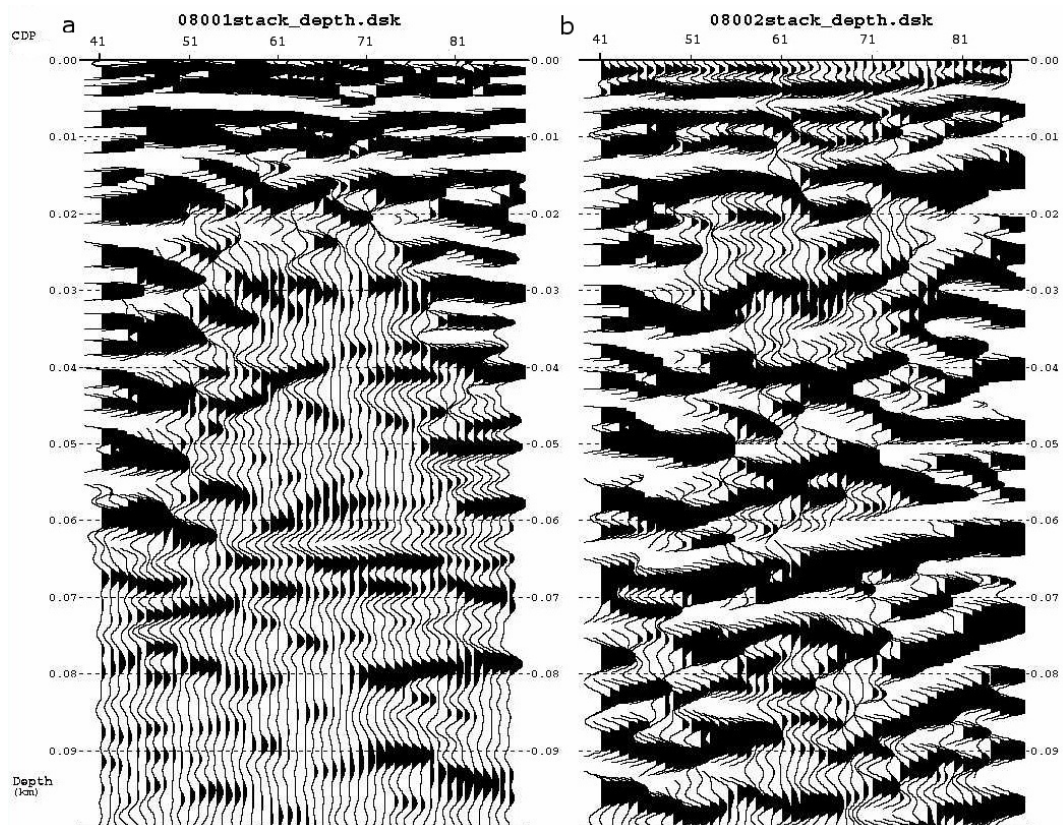
Figure 39: The final stacks for line 08001 (a), south - north and line 08002 (b), west-east with the bed reflection at about 62 m

The bed reflection can be seen in both lines. It is really flat for the south - north line, line 08001, where it can be observed at about 62 m dipping slightly towards the south. The whole stack is 69 m long. Hence the reflection is not visible in the southernmost CMP's of this stack.

In the west - east line, line 08002, the reflection dips towards the west, from about 59 m in the east to 64 m in the west. The whole line is 67.5 m long.

The two lines cross near the borehole KCI. That falls together with the CMP 63 where the depth in both lines, about 62 meters, corresponds very well. This depth fits very well with the data from the core KCI, which was drilled down to a depth of 61.5 m and drilling stopped because of gravel in the ice.

As it was quite difficult to find the bed reflection I compared the seismic data to the processed radar data. Line 08001 hereby corresponds to the traces 83 - 441 of the radar profile 081611 (Figure 40) which was measured from north to south. As one can observe
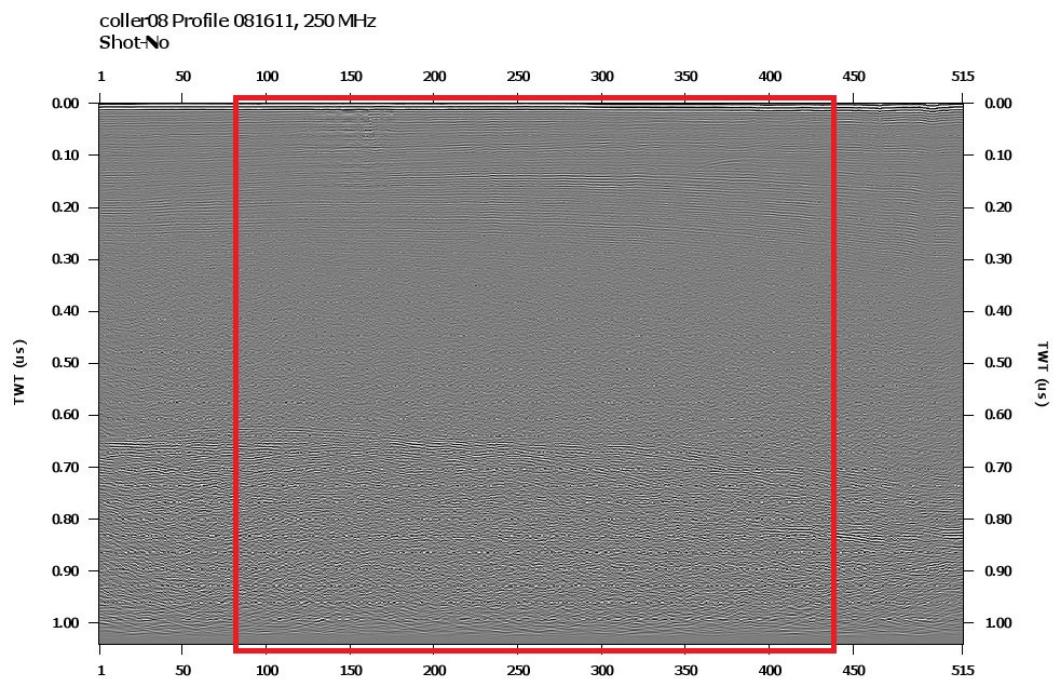
Figure 40: Radar profile north - south along the seismic line 08001 (Pascal Bohleber, personal communication)

in this radar profile, the bed reflection is dipping towards the south as well.

Line 08002 corresponds to the radar profile 081610 (Figure 41), traces 80 - 408. It was measured as well as the seismic data from west to east. In both data sets the dip is stronger than in the north - south line, dipping towards the west.
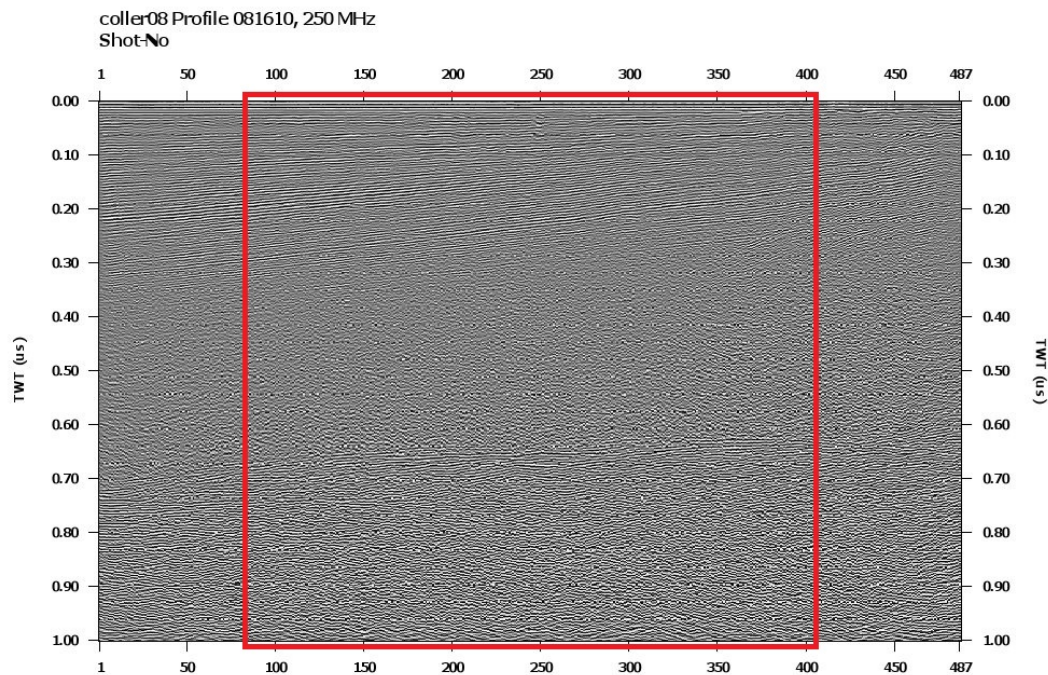
Figure 41: Radar profile west -east along the seismic line 08002 (Pascal Bohleber, personal communication)

4.5.2   Changes in shot geometry at Colle Gnifetti

Some of our problems of the Colle Gnifetti data are due to the shot-receiver geometry. Therefore some changes should be made to this geometry to be able to observe internal reflections.

The shots within the geophone line were not very usable. They had strong ringing for the near offset traces, the ground roll was spatially aliased and it was not possible to filter out the bed reflection. These shots did not help very much to improve the final result. It would therefore be good to carry out more far offset shots, instead of shots within the geophone line.

Here a problem occurs, because of the very limited space at Colle Gnifetti. The shots with the biggest offset, shot 1, shot 34 and shot 33, already reach the biggest possible spread. Nevertheless some more shots could be taken between the end of the geophone line and the far offset shots. Hereby a high fold could be reached without the need of shots within the geophone line.

It would of course be very good to get rid of the ringing due to parasitic resonances. Therefore geophones with a higher spurious frequency are needed, preferably above 400 Hz. Also shooting at larger offset would not reduce the problem of phase shift and variation

in sensitivity of the amplitudes, it would reduce the problem of ringing. The energy of the source SISSY is not high enough to activate the parasitic resonance for the far offset shots. Another possibility, that has already been tried in Antarctica, is the use of a vibroseismic source. To reduce the ringing, the Vibroseis is an advantage because it does not generate such a strong ground roll as an explosion. Besides this, the signal is reproducible and the frequency band of the signal can be chosen.

Another possibility is to shoot in deep boreholes. The less firn the waves have to run through, the less high frequencies are filtered out, increasing the resolution of the signal. This is, however, time intensive as it takes a lot of time and effort to drill deep holes in firn.

4.5.3 Halvfarryggen result

The final stack (Figure 42) obtained for the Halfvarryggen data shows the internal reflections we were missing in the Colle Gnifetti data. This is the first time that internal layers could clearly be observed at an ice dome. The internal layers can be observed from a depth of 300 m down to a bed and within all shots that had sufficient quality to filter out internal reflections. The processing sequence worked fine on all shots except shot 4 and 5. Here, CDP 292 - 386, the internal reflections cannot be seen because of the weak character of these two shots. Sometimes a reflection can be observed shortly after another
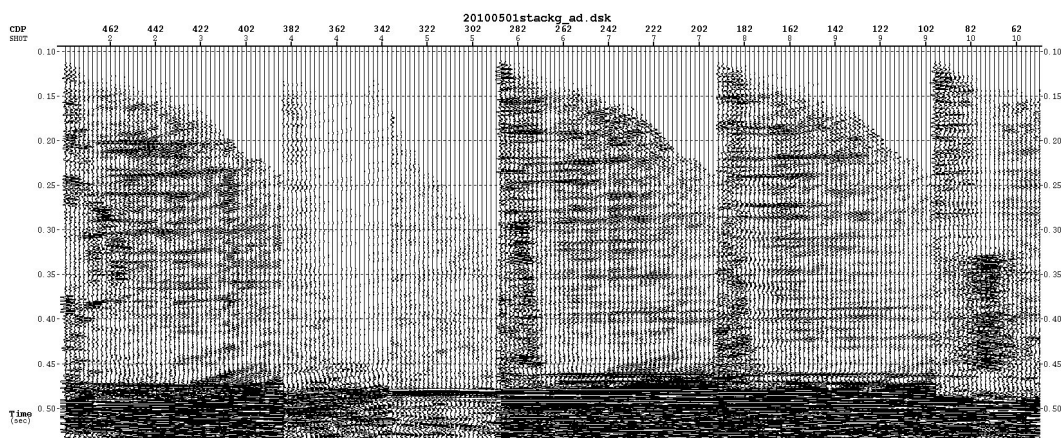
Figure 42: Processed stack for Halvfarryggen data set, with internal reflection and bed at about 0.48 s, corresponding to a depth of round about 900 m

reflection. This is due to the ghost, the wave traveling from the source up to the surface getting reflected there and than traveling back down. Some noise can still be observed at the near offset shots, that could not be filtered out. A zoom into the bed region can be
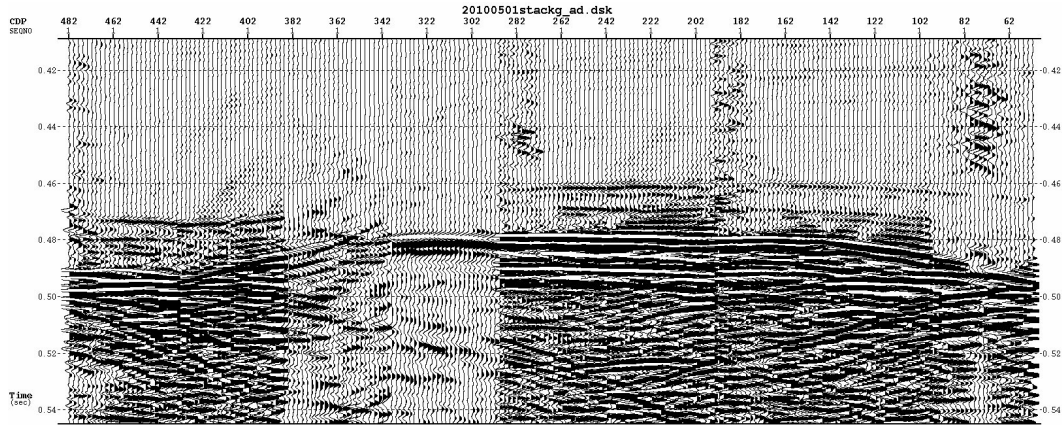
Figure 43: Zoom into the region of the bed reflection, with an internal reflection just above the bed

seen in Figure 43. This reflection is probably due to change in COF, because of the simple shear stress near the bed of the ice sheet (chapter 2.1.2). A change in density can not be the reason for the reflection at that depth and change in bubble content and form is not very likely. Also intrusion of debris is only known close to the bed from ice cores and icebergs [Horgan et al., 2008]. The seismic velocity depends a little bit on temperature [Kohnen, 1974] but the temperature variations are continues and not big enough to cause such reflections. An AVO analysis could help to find out if the reflections can be caused by change in COF (chapter 5.2).

5 Deriving physical properties from seismics

The seismic data from Halvfarryggen and Colle Gnifetti could be used to analyze the physics of the ice. At Colle Gnifetti the diving wave could be used to derive a density profile. At Halvfarryggen internal structures were visible and an AVO analysis could be carried out.

5.1 Diving waves to derive density-depth profile

The diving waves (chapter 2.2.2) can be used to derive a velocity-depth profile. As shown earlier, a velocity-depth profile can be converted into a density-depth profile via the empirical formula of Kohnen (chapter 2.2.1). A density-depth profile was therefore calculated from the Colle Gnifetti data to be compared with the density data from the ice core KCI (Figure 2).

5.1.1 Calculating depth-offset for diving wave at Colle Gnifetti

To make sure that our largest offset is still reached by a diving wave and not by a refracted wave the known density function of the drill core KCI was used to calculate corresponding depth-offset pairs for diving waves. The largest offset, 129.5 m, is between shot 1 and geophone 24.

I approximated the continuous velocity gradient by layers of 0.01 m. The velocity gradient itself was calculated by using the measured density values of KCI and the formula given by Kohnen [1972]. A curve was fitted to this data set, a polynomial of 4th order (fitted curve appendix A.4). An incident angle was inserted for the first layer, which was used to calculate the slowness p (equation 10) and by that the emergent angles for the following layers. Using the emergent angle the horizontal distance of the ray could be calculated for every layer, giving the total offset for a specific depth. In addition the travel time for each layer was calculated to get the corresponding travel time for each depth-offset pair (program appendix B.1).

An offset distance of 141.2 m thereby corresponds to an emergent angle of 26° and a depth of 31.8 m (Figure 44). From the drill core as well as from the radar data it is well known that the glacier is around 60 m deep at that point. Reaching a depth of around 30 m with the diving wave for the largest offset means that we are still within the firn pack.
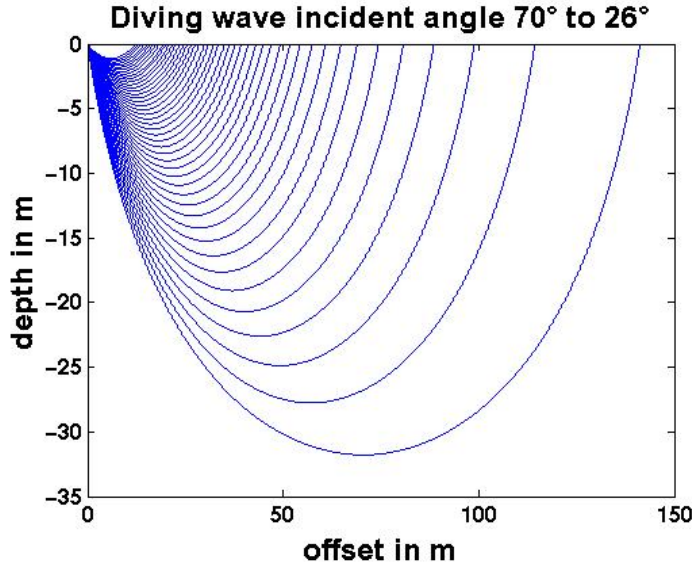
Figure 44: Diving waves calculated with matlab using density profile from KCI

5.1.2 Herglotz-Wiechert inverse formula

The Herglotz-Wiechert inversion is a method to calculate a velocity-depth function from travel time-offset pairs. The inversion formula was introduced by Herglotz in 1907, also solved by Bateman in 1910 and further elaborated by Wiechert in 1910 [Slichter, 1932].

The most important assumption in the Herglotz-Wiechert inversion is a monotonically increasing velocity with depth, which is mandatory for the application of the formula. Low velocity zones lead to wrong results. Therefore it is a quite suitable method for the velocity gradient on a glacier in the accumulation area. Due to the densification process of snow to glacier ice in the dry-snow zone (chapter 2.1.1) no melting occures. As Colle Gnifetti is within the percolation zone ice lenses exist, but they are very small compared to the seismic wavelength. Hence a continues density-depth function can be expected. This still holds in the percolation zone if the ice lenses are small compared to the wave length of the seismic wave.

For a diving wave, the inverse of the ray parameter equals the velocity v at the deepest point Z of the ray:

$$p = \frac{1}{v(Z)}. \tag{33}$$

Here the angle of incidence is $\pi/2$ and the sine is therefore zero in equation (10).

The largest horizontal offset $X(p)$ can be calculated over the ray path, with depth z

$$X(p) = 2 \int_0^{Z(p)} \frac{p}{\sqrt{v(z)^{-2} - p^2}} dz. \tag{34}$$

The aim is now to find $z(v)$ using $X(p)$. Therefore the integration variable is changed resulting in the following equation:

$$\frac{X(p)}{2p} = \int_{v_0^{-2}}^{p^2} \frac{dz/d(v^{-2})}{\sqrt{v^{-2}-p^2}} d(v^{-2}). \tag{35}$$

A similar problem was solved in 1826 by Niels Abel, regarding a particle moving frictionless within the gravity field up and down along a slope taking the time and initial velocity [Aki and Richards, 2002] to calculate the slope. This problem is similar to Abel´s problem and his solution can be used, leading to a result for $z(v)$:

$$z(v) = -\frac{1}{\pi} \int_{v_0^{-1}}^{v^{-1}} \frac{X(p)}{\sqrt{p^2-v^{-2}}} dp. \tag{36}$$

Using partial integration the result can be simplified to

$$z(v_d) = -\frac{1}{\pi} \int_{x=0}^{x=d} \left[cosh^{-1}\left(\frac{v_d}{v_x^a} \right) \right]^{-1} dx, \tag{37}$$

with offset x. The velocity $v_d = (\partial x/\partial t)_d$ is the gradient of the travel time t at the largest offset d, whereas v^a is the apparent velocity and therefore given by $v^a = x/t$.

Taking the known offset-time pairs a curve can be fitted to the data. Using the inverse of the derivative, a velocity function is obtained. This velocity function can now be inserted into the Herglotz-Wiechert formula to obtain the corresponding depth.

5.1.3   Curve fitting

An important point is to have a good fit to the travel time data to calculate the velocities for the Herglotz-Wiechert inversion. The actual problem is to find a good fit where the inverse of the derivative can be taken as the velocities for v_d.

An exponential function of the form

$$t = a(1 - \exp(-bx)) + c(1 - \exp(-dx)) + ex \tag{38}$$

was proposed by Kirchner and Bentley [1990] as a good fit. Here t is the travel time of the diving wave and x the offset. The variables a, b, c, d and e are constants. The advantage is, that the exponential function 'satisfies the requirement of monotonic increase in velocity' [Kirchner and Bentley, 1990].

The velocity is then given by:

$$v = \left(\frac{dt}{dx} \right)^{-1}. \tag{39}$$

I used the software Origin to obtain the fit using a Levenberg-Marquadt (least-square) algorithm. The picked travel times of the diving waves for one line but different shots
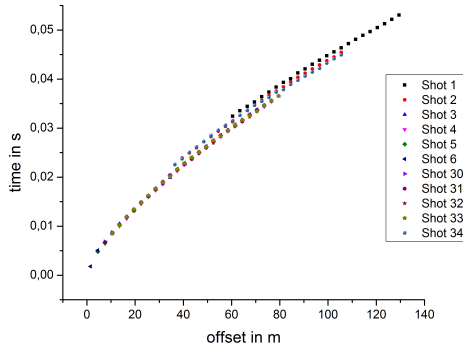
Figure 45: Arrival times of diving waves, line 08001
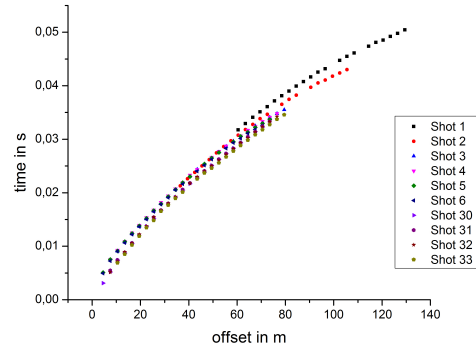
Figure 46: Arrival times of diving waves, line 08002

were quite inhomogeneous as can be seen in Figure 45 and 46. Therefore the exponential function was fitted to different sets of travel times (table 2). First I fitted a curve to all the picked arrival times. Afterwards I fitted a curve only to those picks, which belong to the near offset shots (S3-33). The picked travel times for the near offset shots were quite homogeneous.

A curve was as well fitted to the arrival times of the near offsets shots without the use of the picked arrival time of shot 6, offset 1.5 m. This was done as this pick was quite inaccurate due to a lot of noise. Between the near offset shots, shots 3-6 and 30-33 and the

line, used shots	a	b	c	d	e
08001, 08002	0.01308	0.02544	0.00243	0.37199	2.96E-04
08001	0.00243	0.37199	0.01308	0.02544	2.96E-04
08001, S3-33	0.01609	0.02286	0.00247	0.35695	2.59E-04
08001, S3-33 without 1.5m offset	0.01485	0.02492	0.00234	0.43718	2.69E-04
08002	0.40602	0.00205	0.00525	0.10254	-3.78E-04
08002, S3-33	0.01611	0.02846	0.00138	0.79899	2.45E-04

Table 2: Calculated values for fitting the exponential function to the different data sets

far offset shots (1, 2 and 34) there exists a gap in the travel times (Figure 45 and 46, offset 40-120 m). This means, that a ray with equal length has a longer travel time at the far offset shots than at the near offset shots. Surprising is, that the far offset shots are always slower than the near offset shots. This gap exists and is of similar magnitude between the far offset and the near offset shots on the north, south, west and east side of the seismic

line.

The travel times were as well picked after using a bandpass filter with a slope at the lower limit of 0-10 Hz and at the upper limit of 180-200 Hz. This was done to evaluate whether this gap in travel times is due to inhomogeneities within the firn pack or due to a shift of the phase because of the spurious frequencies above 200 Hz.

To evaluate this shots 1 and 2 were used. It turned out that the observed gap was still present after the use of the BP-filter, by which the spurious frequencies were suppressed. By that it can be concluded, that the gap is not due to the phase shift of the spurious frequencies but it is likely caused by inhomogeneities in the firn pack.

What is surprising however is that the gap between the near offset shots and shot 2 in line 08001 is just as big as the gap between the near offset shots and shot 33. One gets the impression that this gap is symmetric and by that systematic, which can presently not be explained.

5.1.4 Comparison of densities from diving waves and an ice core

The fitted travel time curve was inserted into a Matlab program to calculate the depth-velocity function with help of the Herglotz-Wiechert formula (program appendix B.2). The depth values were always calculated to the depth that corresponds to the largest picked offset. After obtaining the velocity-depth function the empirical formula of Kohnen was used to calculate a depth-density profile to be compared with the density profile of the ice core KCI.

The linear formula by Robin [1958] (equation 8) was as well used to calculate a depth-density profile. The best result could be obtained with the near offset shots (S3-33) of line 08001 without the use of the picked arrival time at 1.5 m offset (Figure 47, green). These were as well the most homogeneous arrival times. In comparison to line 08001, line 08002 yields poorer results. For line 08002 the arrival times of the direct wave were overall not as homogeneous as the results from line 08001. Nevertheless, especially the densities obtained from the near offset shots show some strange behavior (Figure 48, green). In Figure 49 I compared the formulas from Robin [1958] and Kohnen [1972]. Here the arrival times from all picks were used, line08001 and 08002 together. Keeping in mind that the Robin formula is not valid for a density < 0.58 g/cm^3 it gives very good results as well. The difference between the two formulas is mainly the part below 0.55 g/cm^3, where the formula by Kohnen seems to work better.

The velocity-depth function was always calculated down to the depth that corresponds to
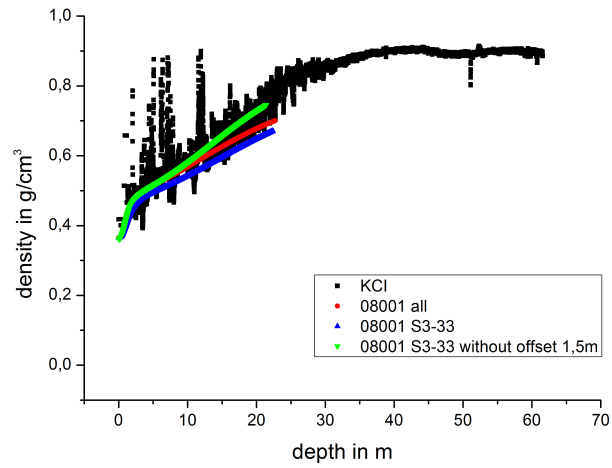
Figure 47: Depth-density profiles line 08001
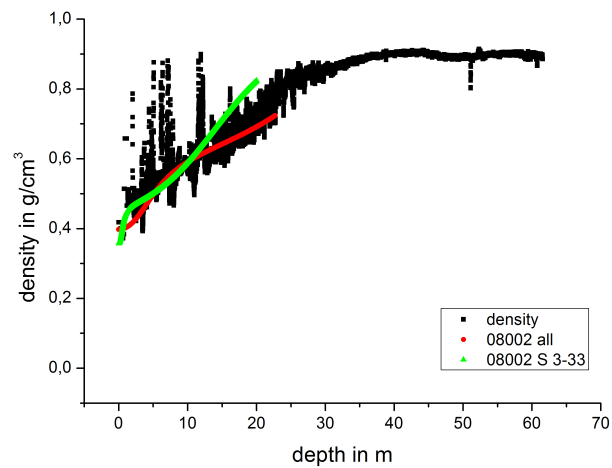
Figure 48: Depth density profiles line 08002
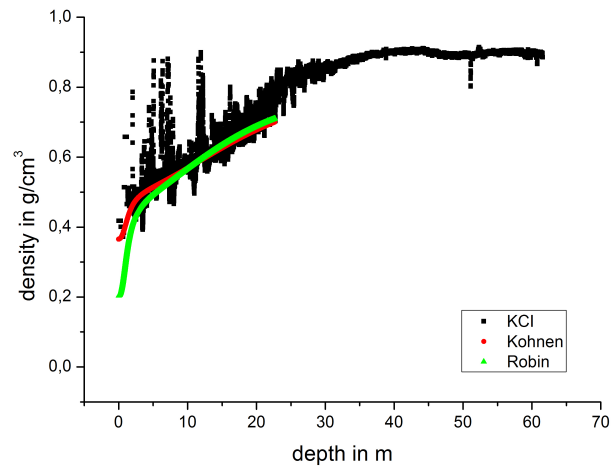
Figure 49: Comparing denities derived from Robin and Kohnen formulas with ice core densities, line 08001 and 08002 together

the largest picked offset. When no ice core is available a velocity function is needed for the processing. To see if velocities can be gained from the diving waves down to the bed of the glacier I calculated the velocity values from the fitted travel time curve for values larger than our largest offset. Thus the velocity, respectively the density could be calculated down to the bed (Figure 50). Here the curve with the best fit to the density data was
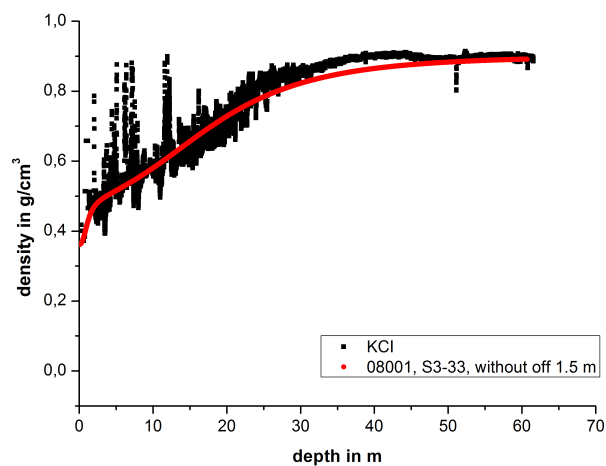
Figure 50: Densities calculated down to the glacier bed, extrapolated from diving waves

used, the travel times from line 08001, S3-33 without offset 1.5 m. Although no diving waves exist within the ice, the travel times from the diving waves within the firn pack can be used to calculate the densities in the ice. This extrapolation gives good results for the

shot number	travel time	apparent velocity	density [Kohnen, 1972]
1	33.54 ms	1893.26 m/s	0.504 g/cm^3
2	32.61 ms	1947.25 m/s	0.511 g/cm^3
3	31.29 ms	1029.40 m/s	0.524 g/cm^3

Table 3: Example for difference in apparent velocity and corresponding density for different travel time and same offset between far offset shots and near offset shots of line 08001

densities down to the glacier bed.

Estimation of travel time difference due to density difference

The reason for the gap that exists between the travel time of the near offset shots and the far offset shots is not clear. Spurious frequencies as a reason can be ruled out, as the gap still existed after filtering out the spurious frequencies (chapter 5.1.3). For an offset of 63.5 m the difference in travel time between shot 1 (far offset) and shot 3 (near offset) is 2.25 ms (line 08001). From the travel time I calculated the apparent velocity for these waves by dividing the travel time t by the shot-receiver offset x. From that the densities belonging to these apparent velocities could than be calculated. For a difference in travel time of 2.25 ms this would correspond to a density difference of 0.0209 g/cm^3 (table 3). The problem is, that this density is kind of an apparent, averaged density over the whole ray path. The true difference in density could be much higher as the true velocity that is reached by the diving wave is higher than the apparent velocity for the diving wave. In a second step I used the program for calculating the diving waves (chapter 5.1.1) and used systematically higher density functions. I added 0.01 g/cm^3 (respectively 0.02 g/cm^3 and 0.03 g/cm^3) to the density data from KCI, calculated the velocities and then the offset, travel time and depth of these rays. The offset - travel time results were afterwards compared to each other (Figure 51). For the example of 63.5 m a difference in travel time of 2.25 ms could nearly be reached by shifting all densities by 0.03 g/cm^3. This resulted in a gap of 2.15 ms. The variation of the density data of KCI (Figure 2) for the first 30 m which are interesting for our diving waves are however much higher than 0.03 g/cm^3.
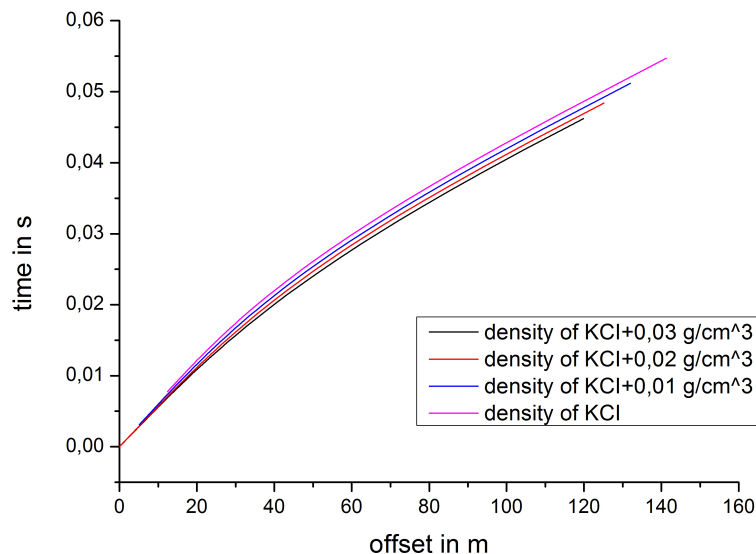
Figure 51: Travel times for diving waves calculated from different density profiles which were than converted to velocities with help of Kohnen [1972]

5.1.5 Advantages of the diving wave to derive densities

When investigating ice with the help of seismics the glacier or ice sheet is mostly shallow and the surveys that are carried out have small offsets compared to seismic surveys that are interested in for example the crust of the earth. With small offsets it is however difficult to pick a good velocity model. The diving wave gives the opportunity to derive such a velocity model which is necessary for a successful processing of the seismic data. Although, the diving wave only runs through the firn pack, the upper 30 m at Colle Gnifetti, the curve fitted to the travel times can be used to calculate the velocities over the whole glacier thickness.

These velocities can be used to calculate the densities of the firn. The comparison to the density data of the ice core KCI shows that deriving density of firn from diving waves works extremely well (Figure 47, 48). This approach was used before on polar ice [Kirchner and Bentley, 1990, King and Jarvis, 2007], but so far not on alpine glaciers with a much smaller firn pack compared to the ice thickness and a stronger density gradient than in polar regions. Some difficulties occur due to the inhomogeneous character of the travel times of the diving waves (Figure 45, 46). The variation in densities, that were used to calculate the travel times, are however smaller than the variations of the density data from ice core KCI (Figure 51). As the diving wave is not a local measurement like the point

measurement of an ice core it averages the densities over a larger area. Nevertheless, it resembles the density data of the ice core very well. It is a very good approach to use the diving wave to derive density data in the accumulation area of an alpine glacier.

5.2   AVO

To investigate internal layers from the Halvfarryggen data set an Amplitude versus Offset (AVO), respectively versus angle (AVA) analysis was used on an internal layer just above the bed. There it could be supposed, that the reflection is due to change in COF (chapter 2.1.2).

I picked the amplitude for the internal reflection at about 0.46 s in shots 2, 3, 6, 7, 8 and 9, which corresponds to a depth of about 900 m. The data was picked after filtering (chapter 4.4.9) as this did not change the amplitudes significantly, but picking the amplitudes at the near offset traces became possible, giving better results (Figure 38). I always picked the maximum amplitude of the wavelet. The signal was, however, not a zero-phase signal (Figure 52). The phenomenon could as well be observed at the diving wave, where it can be expected that the phase is preserved. It therefore seemed reasonable to pick the maximum amplitude of the wavelet and not the first amplitude of the examined signal. The amplitudes were scaled, and an expected AVA function was plotted to be compared
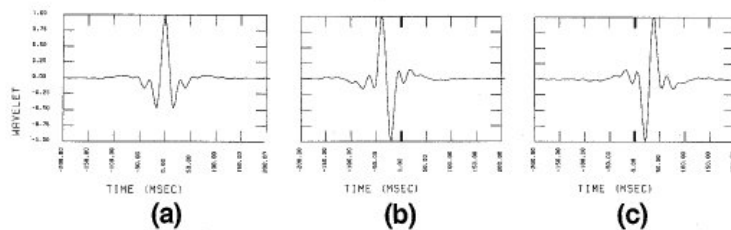
Figure 52: (a) zero-phase signal maximum amplitude at the beginning (time 0 sec), (b), (c) nonzero-phase wavelet [Yilmaz, 1987]

with the picked data. This is explained in the next sections.

When picking the amplitudes they are picked in relationship to their offset. The interesting part however is the change of the reflection amplitude with different incoming angle. This angle can then be calculated when the depth of the internal layer is known. In the case of the internal reflection close to the bed, which is investigated here, the depth is round about 900 m. This gives angles up to 15° for the biggest offset of 495 m.

5.2.1 Scaling for AVO

As source amplitude and attenuation are normally unknown and as they can vary from shot to shot, the amplitudes need to be scaled. An approach exists by Holland and Anandakrishnan [2009] where the diving wave is used to scale for the source amplitude. Two diving waves with the ratio of 2 between the path of these two waves are needed. With help of these two diving waves the source amplitude can than be calculated without knowledge of the attenuation. The source amplitude is then given by

$$A_0 = \frac{B_1^2}{B_2} \frac{\gamma_2}{\gamma_1^2} \tag{40}$$

where B is the amplitude of the diving wave and γ includes spreading losses ($\gamma_1/\gamma_2 = 2$). The problem now exists that a string of 24 geophones was used at Halvfarryggen, which was than moved one spread length to create a streamer with twice the length of the geophone spread. This means, that two shots belong to each other, where the source amplitude can be different. These two shots first needed to be scaled under each other before two diving waves with the path length ratio of 2 could be found.

The amplitude of the diving wave was picked for all offsets. A jump of amplitude could than be observed between offset 255 m belonging to the near offset shot and offset 265 m belonging to the far offset shot. This gap in amplitudes was correct by dividing the amplitudes of the far offset shot by a constant value, fitting those amplitudes to the ones from the near offset shot by eye (Figure 53). The amplitudes of shot 3 were divided by 1.3 to fit to shot 2, as well as those from shot 7 to fit to shot 6. The amplitudes from shot 9 were divided by 1.1 to fit to shot 8.

Now the approach by Holland and Anandakrishnan [2009] could be used to calculate the source amplitude A_0 with help of equation (40). When the source amplitude is known the reflection coefficient can be calculated [Holland and Anandakrishnan, 2009] by

$$R(\theta) = \frac{A_1}{A_0} \frac{1}{\gamma_1} e^{\alpha d_1}, \tag{41}$$

where the correction γ for the spreading loss was done by the gain control (chapter 4.4.9). α is the attenuation and d_1 is the distance of the travel path. In this case the attenuation needs to be known. Dividing by the source amplitude without knowing the attenuation sets a lower limit for the reflection coefficient, as the amplitude of the incident wave is smaller than the source amplitude.

Figure 54 shows the picked amplitudes after the different steps of scaling. First (black, Figure 54) the amplitudes are only scaled so the two shot pairs fit together. Scaling with
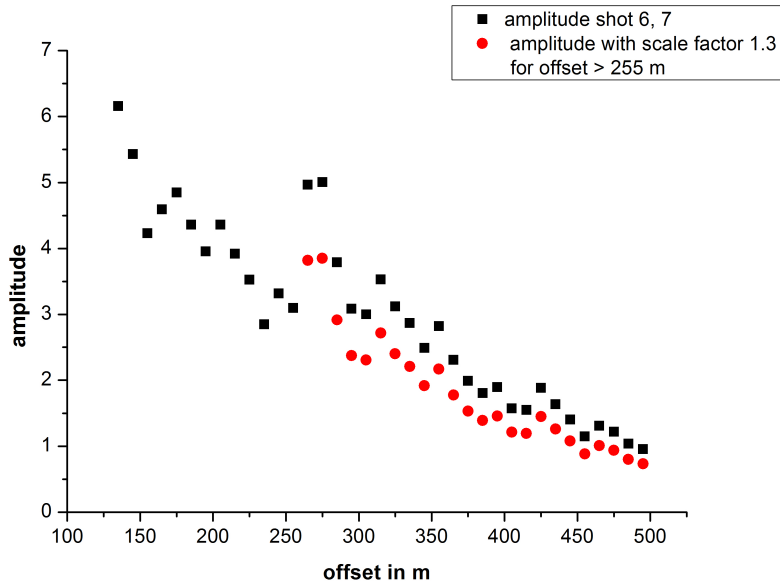
Figure 53: Amplitudes picked from the diving wave for offset bigger than 135 m, scaling of the amplitudes of the far offset shot to the ones of the near offset shot, here factor 1.3 for shot 7 to fit to shot 6

the source amplitude (blue, Figure 54) sets a lower limit for the amplitude as the actual incoming amplitude at the reflection is somehow smaller due to the attenuation. The scaling for the source amplitude shows very good that the high amplitudes that belonged to shot 2 and 3 (bigger source) are now scaled to the same values, as the the amplitudes from shot 6 to 9.

Using a common value for attenuation $\alpha = (0.2 \pm 0.05) * 10^{-3}$ 1/m [Bentley and Kohnen, 1976] gives a slightly higher reflection amplitude, than scaling only with the source amplitude (red, Figure 54).

5.2.2   Expected AVO functions

The Zoeppritz equations (equations 12 to 15) can be used to calculate the reflection coefficients. Approximations for small changes of the physical properties exist like the one given by Aki and Richards [2002] (equation 16).

As internal ice layers are investigated, the assumption can be made, that there is no change in density. This is justified below the firn-ice transition. Hence the equation from Aki and Richards [2002] reduces to:

$$R(\theta) = \left[\frac{1}{2}\left(1 + \tan^2\theta\right)\right]\frac{\Delta v_p}{v_p} - \left[4\frac{v_s^2}{v_p^2}\sin^2\theta\right]\frac{\Delta v_s}{v_s}. \tag{42}$$
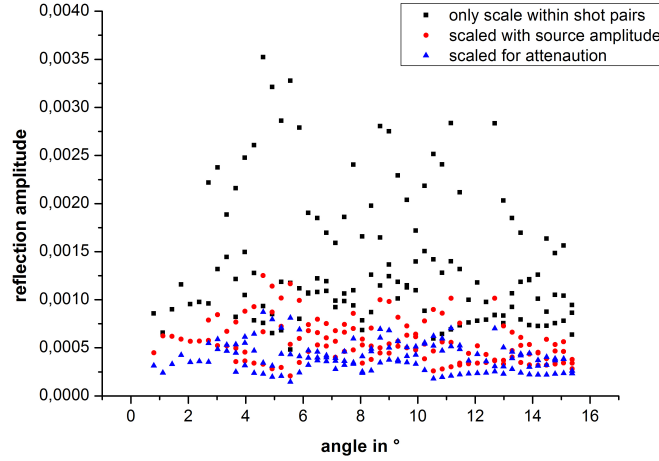
*Figure 54: Picked reflection amplitudes after different steps of scaling (detailed expla-
nation in the text)*

Additionally, v_p and v_s was put into a constant relationship $f = v_p/v_s$, as the S-wave
velocity is not known more precisely. Thus the S-wave velocity can be eliminated and the
equation reduces further to:

$$R(\theta) = \left[\frac{1}{2} \left(1 + \tan^2 \theta \right) \right) - \frac{4}{f^2} \sin^2 \theta \right] \frac{\Delta v_p}{v_p}. \tag{43}$$

The constant value f is then given by $f = 76/39$ when the maximum velocity for v_p is set
to 3800 m/s and v_s is set to 1950 m/s.

Now the reflection coefficient for different incident angles and different velocities of the
second layer can be calculated (Figure 55, program appendix B.3). In the case of the
reflector at about 900 m depth, the graphs of the AVA analysis are all more or less flat
over the first 15° but varying in the value of the reflection amplitude. The graphs were
calculated for a change in velocity up to 200 m/s.

The biggest change in velocity that is possible within ice is a change from an anisotropic
state with c-axis parallel to the propagation direction of the seismic wave to a state with
c-axis perpendicular to the propagation direction of the seismic wave. This would give
a velocity difference of 120 m/s (chapter 2.1.2 and 2.2.3). For a normal incident ray the
reflection amplitude would than be 0.0155, which correspond to the yellow line just above
0.015 in Figure 55. Hence it sets the upper limit for a change in velocity due to COF.

Calculating the reflection amplitude for bigger angles (Figure 56 and 57) shows how con-
clusions about physical properties could be made by comparing the picks to the different
calculated curves when larger offsets are available. With the offsets at Halvfarryggen a
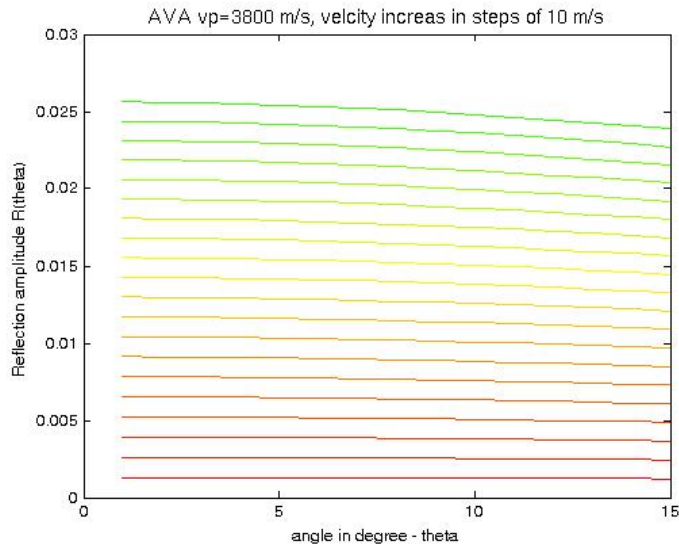
Figure 55: Calculated reflection amplitudes with help of equation 43, velocity of first layer 3800 m/s velocity of second layer varies from 3810 m/s (red) to 4000 m/s (green) in steps of 10 m/s

maximum incident angle of 15° was reached. The curves of the reflection coefficient are all flat within these 15° and thus conclusions of the reflection coefficient cannot be made by comparing the picked and the calculated curves.

5.2.3   Velocity change of internal layers

As the curvature of the AVA plots could not help to derive physical properties, because of the limited range of θ, the scaled values for the reflection amplitudes were used instead. From the results of the scaled amplitudes one would conclude that the jump in velocity near the bed is due to an increase in velocity by around 5 m/s. Figure 58 shows the amplitude values after scaling with the source amplitude. In Figure 59 an estimation for the attenuation is taken into account as well. The unscaled data however has values more around 10 to 20 m/s (Figure 60). This would give an upper value for the velocity change as the source amplitude and attenuation would definitively decrease this value for the reflection coefficient. It can therefore be concluded that the reflection near the bed is due to an velocity increase of the second layer by 5 to 15 m/s.

To be able to deduce something about the change in COF, I also looked at the phase of the lower internal reflectors (Figure 61 and 62). The maximum amplitude of all internal reflectors is negative except for the reflector close to the bed at 0.46 s (no. 11, Figure 62) and the reflector number 8 (Figure 62) where the maximum amplitude is positive. The
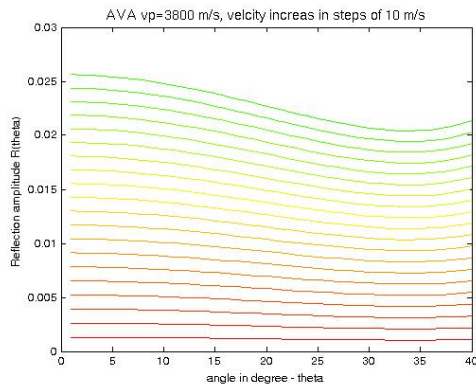
Figure 56: Calculated reflection amplitudes, velocity of second layer varies from 3810 m/s (red) to 4000 m/s (green)
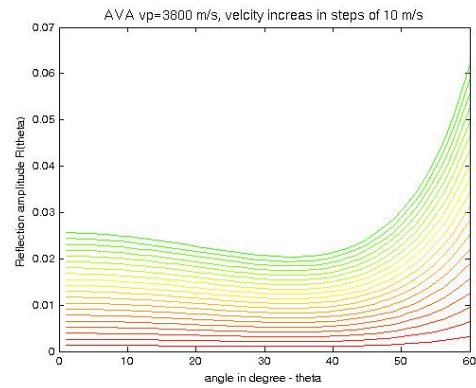
Figure 57: Calculated reflection amplitudes, velocity of second layer varies from 3810 m/s (red) to 4000 m/s (green)
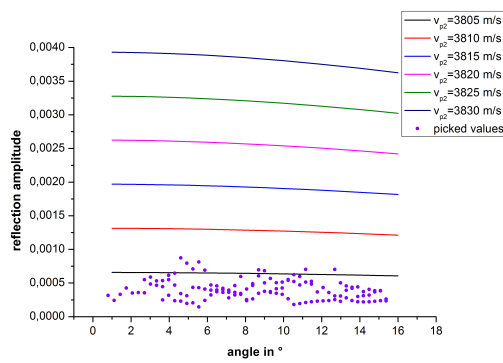
Figure 58: Reflection amplitudes scaled with source amplitude, plotted over calculated reflection amplitudes. $v_{p1} = 3800$ m/s
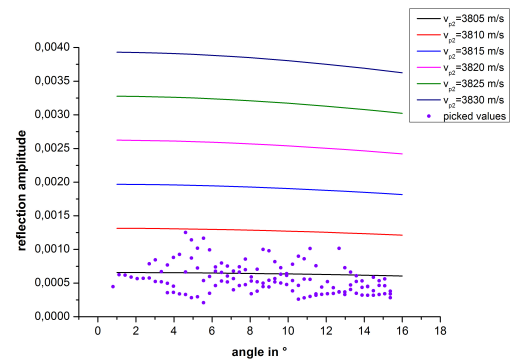
Figure 59: Reflection amplitudes scaled for source amplitude and attenuation, plotted over calculated reflection amplitudes. $v_{p1} = 3800$ m/s
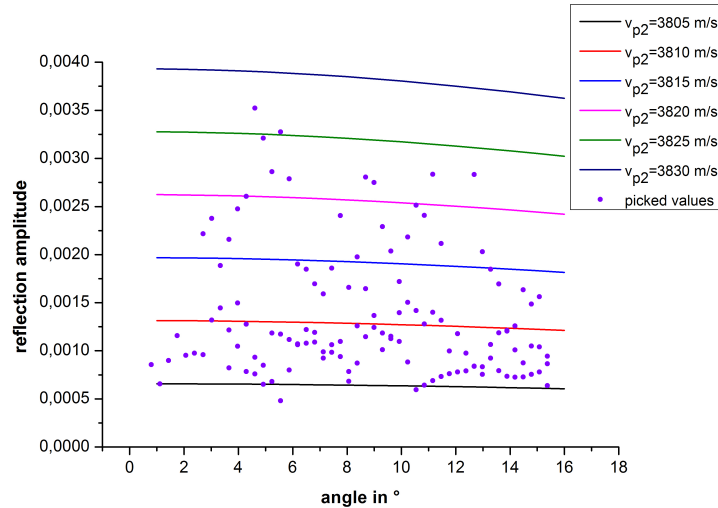
Figure 60: Reflection amplitude only scaled between corresponding shots with help of the diving wave. The high values up to 0.003 belong to shot 2 and 3 were the source amplitude was bigger. $v_{p1} = 3800 \ m/s$

strongest of these internal reflectors is reflector number 11, the reflector close to the bed, so the biggest change in velocity occures at that reflector.   The change in velocity is negative for those reflections that have the amplitude negative. This means, that the velocity of the second layer is lower than that of the layer above. As nearly all internal reflectors have a negative phase, it can be concluded that the velocity is getting slower and slower. Near the bed of the ice sheet it then changes to a faster velocity.

5.2.4   Changes in COF

Reflections from within the ice, which result from changes in seismic velocity could be observed at Halvfarryggen. In nearly all cases the velocity within the ice changes from a faster velocity to a slower one in the next layer, except the strong reflector close to the bed. Here the velocity changes to a higher velocity. The change from a slower velocity to a higher one near the bed may come from a change in COF where the c-axis is rotated towards the vertical (chapter 2.1.2). As the P-wave is fastest along the c-axis of a crystal a vertical, single maximum of the c-axes leads to the fastest possible velocity in ice sheet. The part where the velocity gets slower and slower is a bit more difficult to explain, but it could be caused by a change in the orientation of the girdle fabric (Figure 63) or vertical c-axes orientation with different variations around the vertical.
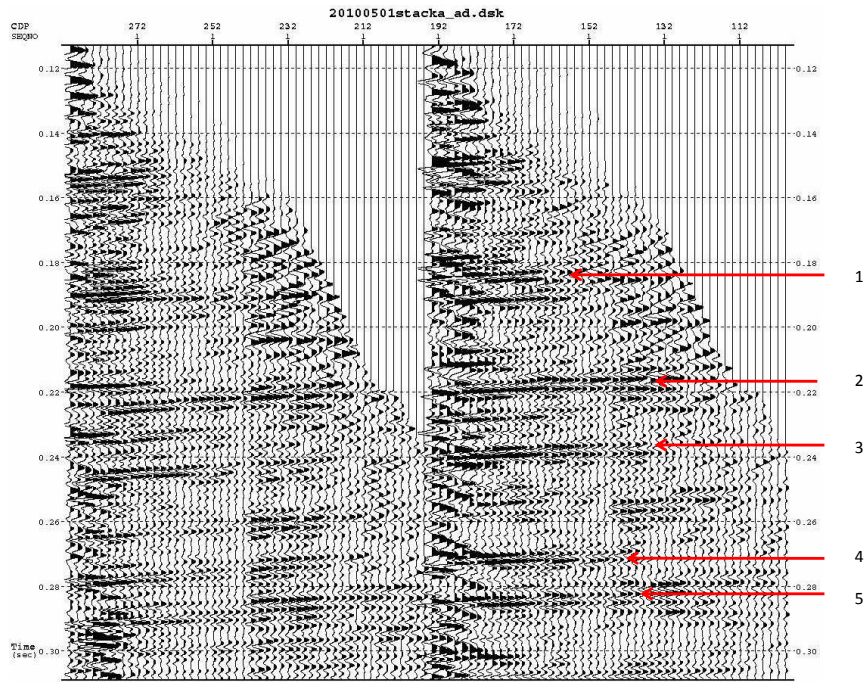
Figure 61: Internal layers for shot 6, 7, 8 and 9 down to 0.3 s
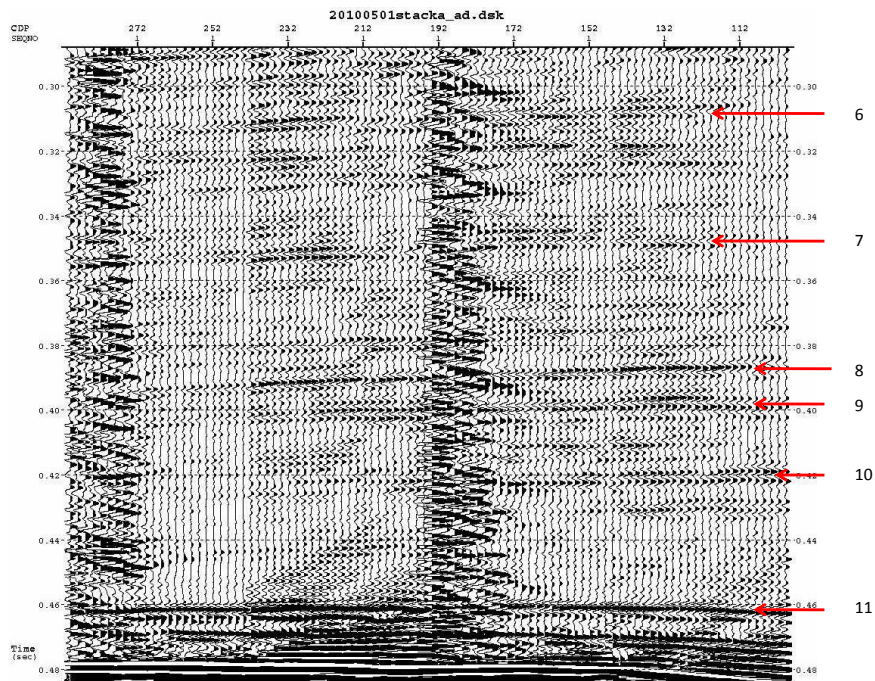
Figure 62: Internal layers for shot 6, 7, 8 and 9 down to the bed

The crystal orientation fabric can be described by eigenvalues λ_i. With help of these eigenvalues the velocities for the different directions in space for different COF can be calculated. Following Eisen et al. [2007] the velocity in one direction can be calculated by $v_i = v_\perp + \Delta v \lambda_i$ with $v_\perp = 3800$ m/s. The biggest velocity difference is $\Delta v = 120$ m/s, for a change from horizontal oriented c-axes to vertical oriented c-axes. For isotropic ice the eigenvalues are given by $\lambda_1 = \lambda_2 = \lambda_3 = 1/3$, for a girdle by $\lambda_1 = 2/3$, $\lambda_2 = 1/3$, $\lambda_3 = 0$ and for a single maximum by $\lambda_1 = 1$, $\lambda_2 = \lambda_3 = 0$.

When the shot-receiver line is along the x-axis of a coordinate system the vertical direction would be the z-axis and x- and y-axis the horizontal directions. For isotropic ice, where the c-axes are oriented randomly, the eigenvalues would lead to a velocity of 3840 m/s in all directions of space. Due to the stresses within the ice the c-axes orientation can change into a girdle, thus the c-axes of all crystals are oriented in one plane over 180°. When the c-axes are oriented in a vertical girdle the vertical velocity would increase by 40 m/s compared to the isotropic state. A girdle vertical and parallel of the direction of shooting, thus in the x,z-plane, would have a velocity in x-direction of 3840 m/s (Figure 63,b). A girdle in the y,z-plane, thus perpendicular to the shot-receiver line would have a velocity in x-direction of 3800 m/s (Figure 63,a). As the velocity of the P-wave depends on the propagation direction of the wave it depends on the velocity in z- and x-direction. A wave would thus be slower when the girdle is oriented perpendicular to the direction of shooting than when it is parallel to the shooting line. A girdle that is moved from a parallel, vertical orientation to a perpendicular, vertical orientation would thus lead to a decrease in velocity. Another possibility for a decrease in velocity is when the c-axes orientation is vertical and the c-axes would than be moved a bit away from the vertical, thus leading to a slower velocity as well.

At Halvfarryggen reflections could be observed from a depth of around 300 m down to the bed. Here the maximum phase can be analyzed to see whether these reflections are from a change to higher or lower velocities. Even if no AVA analysis is carried out it is thus possible to say something about the change in velocity. The negative phase of the internal reflectors (Figure 61, 62) shows, that the seismic velocity decreases with depth. The sudden increase in velocity near the bed is then most likely due to the vertical orientation of the c-axes.

Carrying out an AVA analysis holds some problems. It is important to have a large variation in incident angles for the reflection that is observed. For the reflection near the bed at Halvfarryggen angles up to 40° would be important (Figure 56). As the Halvfarryggen data
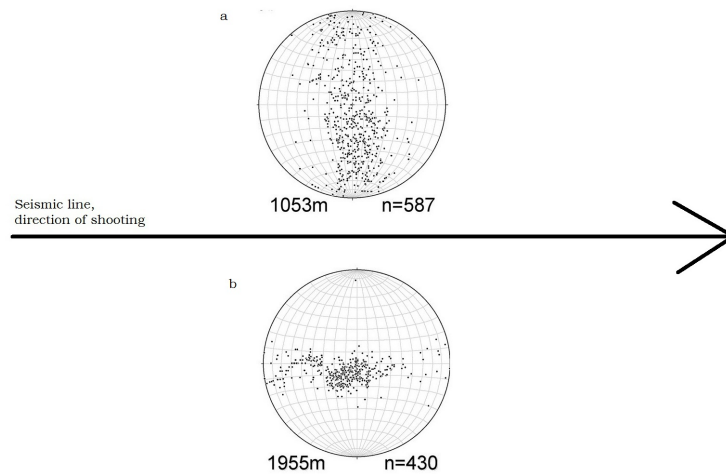
Figure 63: Orientation of seismic line in comparison to c-axis orientation (a) velocity would be slower compared to isotropic state, (b) velocity would be faster compared to isotropic state

only covers angles up to 15° it is not possible to derive information about the reflection coefficient by comparing the curvature of the calculated and picked reflection amplitudes (Figure 55). But also without a wide range of angles it was possible to give an upper and lower limit for the velocity increase of the reflection. The unscaled reflection amplitudes are not higher than they would be for a velocity increase of 15 m/s (Figure 60). The amplitudes scaled with help of the source amplitude derived from the diving wave show an increase in velocity of 5 m/s (Figure 58). It could thus be concluded that the change in velocity of 5-15 m/s near the bed at Halvfarryggen is most likely due to change in COF towards a vertical oriented c-axis. This change is after a decrease in velocities due to changes in girdle orientation or due to changes in the extension of the c-axes around the vertical. It would thus help to have more data, especially from a shot-receiver line perpendicular to the one here, to be able to derive more information about the COF. It could for example help to find out if the velocity decrease is due to different orientation of the girdle or due to changing extension of the c-axes around the vertical.

6   Conclusion and Outlook

So far analyzing an ice core is the only way to gain knowledge about the physical ice properties. In this thesis I analyzed two seismic data sets so derive physical properties of ice. Densities could be derived at Colle Gnifetti and internal structures could be observed at Halvfarryggen, that were investigated more closely by analyzing the reflection coefficient. With the Herglotz-Wiechert inversion it was possible to derive densities of the firn from the Colle Gnifetti data. The filtering of the data was however difficult and no internal reflections could be filtered out. To be able to gain good results about the internal structure of ice with reflection seismics a good survey geometry is mandatory. As it is difficult to separate the different waves by their frequency, it is important to separate them in the time-offset domain.

The Colle Gnifetti data shows the difficulty in finding internal layers, assuming they do exist there. The problem is, that the different wave types are overlying each other in the time-offset domain as well as in their frequencies. Especially for thin glaciers, with a thick firn pack far offset shots are important to separate the waves from each other. Thus the diving wave and refracted waves are not overlaying the reflection, so that it became possible to filter out at least the bed reflection (chapter 4.5).

Another big problem in the Colle Gnifetti data was the strong ground roll. On the one hand it has a lot of energy and is therefore able to activate parasitic resonances, creating a lot of noise (chapter 4.3). On the other hand the high amplitudes of the ground roll itself disturb the records enormously. Besides this, the low velocity of the ground roll harbors the danger that the recording resolution is not high enough and the frequencies become spatially aliased, like they are in the Colle Gnifetti data. Filtering out the ground roll with a FK-filter is therefore no longer possible. It is thus necessary to shoot more far offset shots to gain better results with seismics at Colle Gnifetti.

Although no internal reflections could be observed at Colle Gnifetti, physical ice properties could still be derived. A density profile was derived from the travel times of the diving wave. The diving wave therefore gives a fantastic opportunity to develop a velocity model for processing of the data when no ice core data is available. Bedsides this, the densities of the firn pack could be determined very well with this approach (chapter 5.1). Even calculating the densities over the whole glacier thickness was possible, although no diving wave exists within the glacier ice. The results show that using the Herglotz-Wiechert inversion to calculate velocities respectively densities from diving waves works just as well on an

alpine glacier as in polar regions.

The internal reflections we were missing in the Colle Gnifetti data could be observed in the Halvfarryggen data. From a depth of around 300 m internal reflectors exist down to the bed. It is the first time that internal layers could clearly be observed at an ice dome, over such a big depth. These internal layers can be observed in all shots that had a quality high enough to filter out internal reflections, shots 2, 3, 6-10. As Halvfarryggen has an ice thickness of around 900 m and the used shot-receiver offsets were much bigger than at Colle Gnifetti the waves were separated in the time-offset domain. Without spatial aliasing of the ground roll an FK-filter worked fine here. Thus it was possible to filter out many internal reflections. The internal reflectors could be analyzed more precisely with help of an AVA analysis.

When the aim is to carry out such an AVA analysis a wide range of angles is desirable. Only with a wide range of angles the characteristic behavior of the reflection coefficient curve shows up. It can then be used to derive changes in the physical properties.

For a reflection at a depth of 900 m, like investigated in the Halvfarryggen data, an offset of at least 1500 m, better 3000 m is needed to supply a sufficient range of angles. Even if this range is not available the data can still be used to make an approximation of the change in seismic velocity. When using the actual amplitude values the problem is to scale the amplitudes correctly. Especially the unknown attenuation of the wave is not easy to estimate, reliable values can be found in the literature.

With values from literature for the attenuation an increase in seismic velocity between 5 and 15 m/s for the internal reflector close to the bed at Halvfarryggen could be derived. The negative amplitudes of the lower internal reflection indicate a decrease in velocity over depth, down to that near bed reflector where the seismic velocity suddenly increases again. This decrease in velocity could then be due to a change in COF from a girdle, parallel and vertical to the direction of shooting to a girdle perpendicular and vertical to the direction of shooting or due to a movement of the c-axes away from the vertical. This girdle furthermore turns into a point, vertical orientation of the c-axes near the bed (chapter 5.2). Even without an AVA analysis it is thus possible to say whether the velocity is getting faster or slower and make assumptions about the change in COF. With the AVA analysis the magnitude of the change in seismic velocity can then be determined.

To improve the results from Colle Gnifetti and hopefully make it possible to compare

the seismic data with the radar data a new survey is needed with a changed shot-receiver geometry. This survey is going to be carried out on Colle Gnifetti this summer. Additionally to the equipment from 2008 a small Vibroseis (ElViS, www.geosym.de) is going to be used. A big Vibroseis truck has so far been used on a glacier at Ekströmisen within the field season 2009/2010 [Kristoffersen et al., 2010], with very promising results. The advantage is hopefully a reduction of the strong ground roll. In the next field season in Antarctica 2010/2011 the big Vibroseis that was used on Ekströmisen is going to be used at Halvfarryggen as well. With larger offsets between shot and receiver it should then be easier to carry out an AVA analysis. Additionally it would be good to shoot two lines perpendicular to each other to gain the possibility to derive more information about the change in COF. Besides this, the S-wave will be analyzed. The velocities of the S-wave in ice can be derived and the higher resolution of the S-wave in comparison to the P-wave can be of use for the analysis of the internal ice structures.

It was demonstrated that seismics is a tool to investigate physical properties of ice. With radar surveys carried out along the same profiles like the seismic lines it will hopefully become possible to use these two geophysical methods for a combined seismic and radar inversion to gain a more comprehensive knowledge about physical properties of ice sheets.

References

K. Aki and P. G. Richards. *Quantitative Seismology*. University Science Books Sausalito, California, 2002. ISBN 0-935702-96-2.

J. Alean, W. Haeberli, and B. Schädler. Snow accumulation, firn temperature and solar radiation in the area of the colle gnifetti core drilling site (monte rosa, swiss alps): Distribution patterns and interrelationship. *Zeit. Gletsch. Glaz.*, 19(2):131–147, 1983.

R. B. Alley. Fabrics in polar ice sheets: Development and prediction. *Science*, 1988.

S. Anandakrishnan. Dilatant till layer near the onset of streaming flow of ice streamc, west antarctica, determined by avo (amplitude vs offset) analysis. *Ann. Glaciol.*, 36:283–286, 2003.

S. Anandakrishnan, J. J. Fitzpatrick, R. B. Alley, A. J. Gow, and D. A. Meese. Shear-wave detection of asymmetric c-axis fabrics in the gisp2 ice core. *J. Glaciol.*, 40(136):491–496, 1994.

B. Benjumea and T. Teixidó. Seismic reflection constraints on the glacial dynamics of Johnsons Glacier, Antarctica. *J. Appl. Geophys.*, 46:31–44, 2001.

C. R. Bentley. Seismic-wave velocities in anisotropic ice: A comparison of measured and calculated values in and around the deep drill hole at byrd station, antarctica. *J. Geophys. Res.*, 77, 1972.

C. R. Bentley and H. Kohnen. Seismic refraction measurments of internal friction in antarctic ice. *J. Geophys. Res.*, 1976.

D. D. Blankenship, C. R. Bentley, S. T. Rooney, and R. B. Alley. Seismic measurements reveal a saturated porous layer beneath an active antarctic ice stream. *Nature*, 322 (6074):54–57, 1986. doi: doi:10.1038/322054a0.

B. Buttkus. *Spectral Analysis and Filter Theory in applied geophysics*. Springer, 2000. ISBN 3-540-62674-3.

A. T. Dennison. The design of electromagnetic geophones. *Presented at Hague Meeting of the European Association of Exploration Geophysicists*, 1951.

O. Eisen, U. Nixdorf, L. Keck, and D. Wagenbach. Alpine ice cores and ground penetrating radar: combined investigations for glaciological and climatic interpretations of a cold alpine ice body. *Tellus*, 55B(5):1007–1017, 2003.

O. Eisen, I. Hamann, S. Kipfstuhl, D. Steinhage, and F. Wilhelms. Direct evidence for continuous radar reflector originating from changes in crystal-orientation fabric. *The Cryosphere*, 1(1):1–10, 2007. ISSN 1994-0416. URL http://www.the-cryosphere.net/1/1/2007/.

K. Faber and P. W. Maxwell. Geophone spurious frequency: What is it and how does it affect seismic data quality? *Canadian Journal of exploration geophysics*, 33(12):46–54, 1997.

T. Forbriger. Das elektrodynamische seismometer. Skriptum zur Vorlesung 'Seismologische MEsstechnik', 2007.

W. Haeberli, W. Schmid, and D. Wagenbach. On the geometry, flow and age of firn and ice at the colle gnifetti core drilling site (monte rosa, swiss alps). *Zeit. Gletsch. Glaz.*, 24(1):1–19, 1988.

W. Haeberlie and M. Funk. Borehole temperature at the colle gnifetti core-drilling site (monte rosa, swiss alps). *J. Glaciol.*, 37(125):37–46, 1991.

M. M. Herron and C. C. Langway. Firn densification: an empirical model. *J. Glaciol.*, 25(93):373–385, 1980.

C. W. Holland and S. Anandakrishnan. Subglacial seismic reflection strategies when source amplitude and medium attenuation are poorly known. *J. Glaciol.*, 55(193):931–937, 2009. doi: 10.3189/002214309790152528.

Roger LeB. Hooke. *Principles of Glacier Mechanics*. Cambridge University Press, 2005. ISBN 978-0-521-83609-3.

H. J. Horgan, S. Anandakrishnan, R. B. Alley, L. E. Peters, G. P. Tsoflias, D. E. Voigt, and J. P. Winberry. Complex fabric development revealed by englacial seismic reflectivity: Jakobshavn isbræ, greenland. *Geophys. Res. Letters*, 35(10):L10501+, May 2008. ISSN 0094-8276. doi: http://dx.doi.org/10.1029/2008GL033712.

IPCC. Climate change 2007 (ar4), synthesis report. *Fourth Assessment Report of the Intergovernmental Panel on Climate Change*, 2007.

E.C. King, J Woodward, and A.M. Smith. Seismic evidence for a water-filled canal in defoming till beneath rutford ice stream, west antarctica. *Geophys. Res. Letters*, 31: 61–76, 2004. doi: 10.1029/2004GL020379.

Edward C. King and Eric P. Jarvis. Use of shear waves to measure poissons ratio in polar firn. *JEEG*, 12(1):1521, 2007.

Edward C. King, John Woodward, and Andy M. Smith. Seismic and radar observations of subglacial bed forms beneath the onset zone of rutford ice stream, antarctica. *J. Glaciol.*, 53:665–672, 2007. URL `http://www.ingentaconnect.com/content/igsoc/jog/2007/00000053/00000183/art00015`.

J. F. Kirchner and C. R. Bentley. Riggs iii: Seismic short-refraction studies using an analytical curve-fitting technique. *The Ross Ice Shelf: Glaciology and Geophysics Antarctic Research Series*, 42(5):109–126, 1990.

H. Kohnen. Über die beziehung zwischen geschwindigkeiten und der dichte in firn und eis. *Zeitschrift für Geophysik*, 38:925–935, 1972.

H. Kohnen. The temperature dependence of seismic waves in ice. *J. Glaciol.*, 13(67): 144–147, 1974.

H. Kohnen and C. R. Bentley. Seismoglaziologische untersuchungen nahe byrd station, antarktis. *Meteorology and Atmospheric Physics*, 22(2):311–324, 1973. URL `http://dx.doi.org/10.1007/BF02247550`. 10.1007/BF02247550.

Y. Kristoffersen, R. Blenkner, O. Boebel, R. Drews, L. Kindermann, C. Hofstede, D. Jansen, A. Lambrecht, C. Mayer, N. Neckel, D. Steinhage, R. Witt, and O. Eisen. Vibroseismic measurements on an ice shelf. Poster at EGU General Assembly, 02.-07. May, Vienna, Austria, 2010.

Toni P. Labhart. *Geologie der Schweiz*. Ott Verlag Thun, 2001. ISBN 3-7225-6760-2.

L. Levato, L. Veronese, A. Lozej, and E. Tabacco. Seismic image of the ice-bedrock contact at the lobbia glacier, adamello massif, italy. *J. Appl. Geophys.*, 42:55–63, 1999.

M. Lüthi and M. Funk. Dating ice cores from a high alpine glacier with a flow model for cold firn. *Ann. Glaciol.*, 31:69–79, 2000.

M. Lüthi and M. Funk. Physics of glaciers i. Versuchsanstalt für Wasserbau, Hydrologie und Glaziologie VAW, ETH Zürich, 2008.

M. P. Lüthi and M. Funk. Modelling heat flow in a cold, high-altitude galcier: interpretation of measurements from colle gnifetti, swiss alps. *J. Glaciol.*, 47(157):314–324, 2001.

C. Martin, G. H. Gudmundsson, H. D. Pritchard, and O. Gagliardini. On the effects of anisotropic rheology on ice flow, internal structure, and the age-depth relationship at ice devides. *J. Geophys. Res.*, 2009.

W. S. B. Paterson. *The Physics of Glaciers.* Pergamon, 1994. ISBN 0-08037944 3.

J. R. Resnick. *Seismic data Processing for AVO and AVA Analyses*, volume 8 of *Offset-dependent reflectivity - Theory and Practice of AVO Analyses, Investigations in Geophysics Series.* Society of Exploration Geophysicists, 1993.

G. De Q. Robin. Seismic shooting and related investigations. *Norwegian-British-Swedish Antarctic Expedition, 1949-52, Scientific Results, Norsk Polainstitutt, Oslo*, 1958.

L. B. Slichter. The theory of the interpretation of seismic travel-time curves in horizontal structures. *Physics*, 1932.

A. Smith and T. Murray. Bedform topography and basal conditions beneath a fast-flowing west antarctic ice stream. *Quat. Sci. Rev.*, 2008. ISSN 02773791. doi: http://dx.doi.org/10.1016/j.quascirev.2008.05.010. URL `http://dx.doi.org/10.1016/j.quascirev.2008.05.010`.

A. M. Smith. Subglacial bed properties from normal-incidence seismic reflection data. *JEEG*, 12(1):3–13, 2007.

B. Stauffer. Enclosure of air during metamorphosis of dry firn to ice. *Ann. Glaciol.*, 1985.

C. Wesche, S. Riedel, and D. Steinhage. Precise surface topography of the ground ice ridges at the ekströmisen, antarctica, based on several geophysical data sets. *ISPRS Journal of Photogrammetry and Remote Sensing*, 2009.

Ö. Yilmaz. *Seismic data processing*, volume 2 of *Investig. Geophys.* Society of Exploration Geophysicists, 1987.

Ö. Yilmaz. *Seismic data processing*, volume 2 of *Investig. Geophys.* Society of Exploration Geophysicists, 2001.

Appendices

A Additional figures

A.1 Complete COF from EDML

The change in c-axis over depth for the ice core EDML, east Antarctica. The explanation about crystal orientation fabric is treated in chapter 2.1.2.
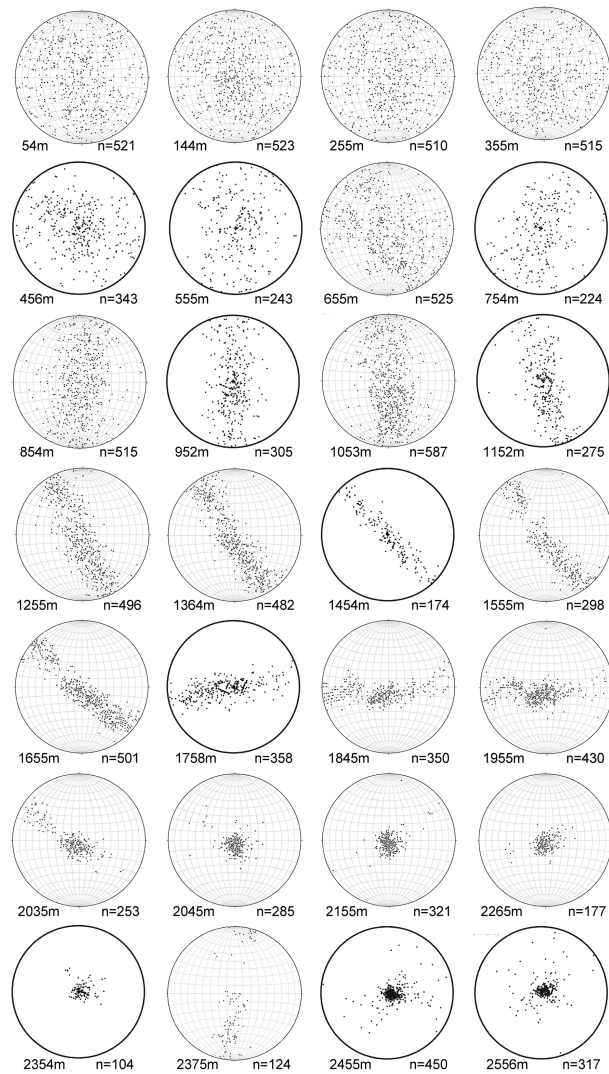
Figure A1: COF for different depth from ice core EDML (Ilka Weikusat, personal communication)

A.2   Comparison before and after FK-filter for line 08002

The data from Colle Gnifetti was FK-filtered after stacking the data. This improved the result enormously (chapter 4.2.6).
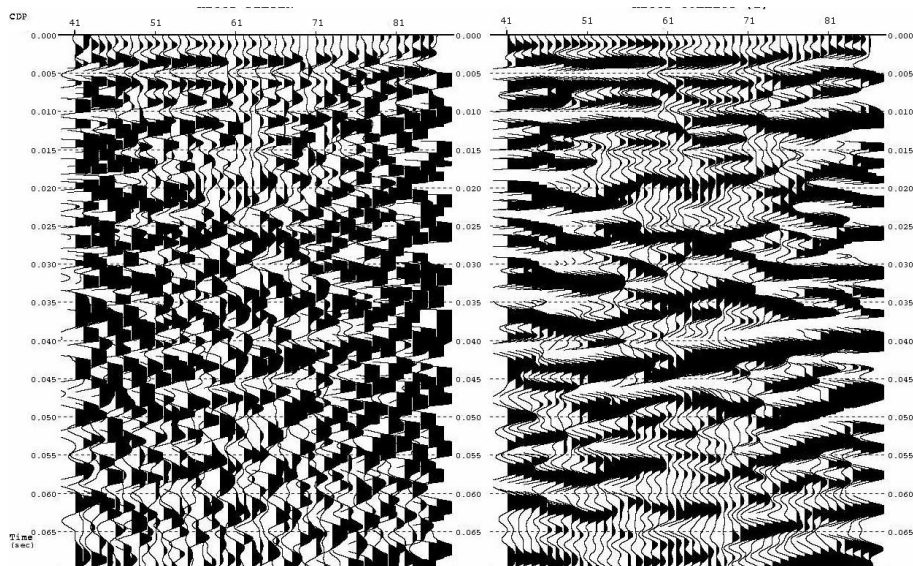
Figure A2: Compare before (a) and after (b) FK-filter, line 08002

A.3   Velocity Model for Halvfarryggen

Density data was only available to an depth of 84 m. It was therefore extrapolated to greater depth to calculate a velocity model for the NMO correction (chapter 4.4.6).
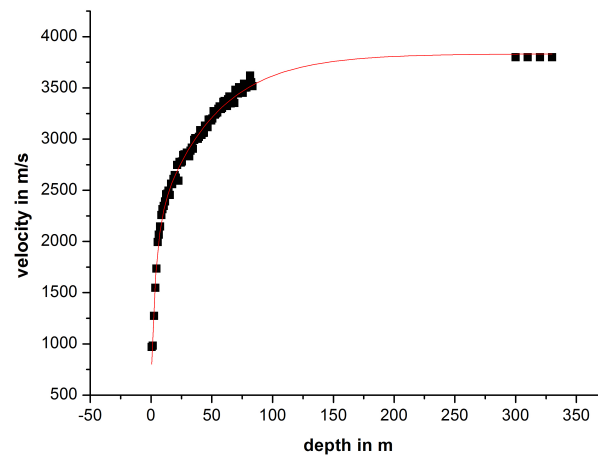
Figure A3: Velocity model, down to 80 m velocities calculated from density data from DML94, afterwards extrapolated, expecting ice at a depth of 300 m

A.4   Fit to density data for matlab program

For the calculation of the arrival times of the diving wave the density data of the ice core KCI was used. For better calculation a polinomial of 4th order was fitted to the density data (chapter 5.1.1).
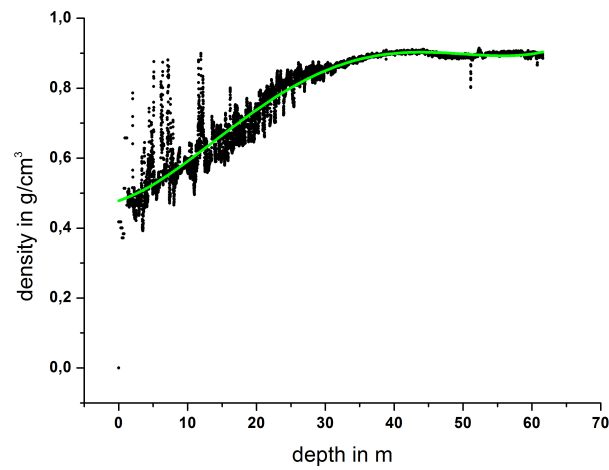
Figure A4: Polynomial of 4th order fitted to density data

B Programs

B.1 Calculation of diving wave

The travel path of the diving wave was calculated for Colle Gnifetti, using the density data from KCI (chapter 5.1.1).

```
                                        divingwave
             % calculate path of diving wave
             % Anja Diez

             clear all, close all;
             clf;

             % to calculate for all alpha
             m    = 0;          % to count number of cicles
             result=zeros(m,4);       % matrix with results Z,X,T,V
             for a=70:-1:26
                 m        = m+1;
                 %a       = 26;                  % incident angle
                 % variables
                 deltaz   = 0.001;              % thickness of depthlayers in m
                 z        = 0;                  % start at surface
                 alpha    = pi/180*a;           % start angle for ray path
                 v        = 1567.51812;         % velocity of first layer
                 x        = 0;                  % x distance to shot for first layer
                 deltax   = 0;                  % start for delatx to calculate traveltime
                 time     = 0;                  % start to calculate travel time
                 i        = 1;

                 % calculate p (slowness) for ray path
                 p=sin(alpha)/v;

                 % calculate emergent angle until wave gets refracted and distance to shot
                 while alpha<pi/2
                     depth(i)    = -z;
                     offset(i)   = x;

                     % travel time
                     dy          = sqrt(deltax^2+deltaz^2);
                     time            = time + dy/v;


                     deltax      = deltaz*tan(alpha);
                     x           = x+deltax;
                     z           = z+deltaz;
                     i           = i+1;
                     %v          =
             1567.51812+89.61514*z-0.17178*z^2-0.03046*z^3+3.05205*10^-4*z^4;      %origin
             fit for KCI
                     %v          =
             1651.77588+85.04098*z-0.00906*z^2-0.03285*z^3+3.17978*10^-4*z^4;      %origin
             fit for KCI+0,01g/cm3
                     %v          =
             1730.96+81.34275*z+0.08815*z^2-0.03325*z^3+3.08379*10^-4*z^4;      %origin fit
             for KCI+0,02g/cm3
                     v           = 1768.78418+91.64231*z-0.97701*z^2;
                         %originf fit for KCI+0,03g/cm^3 (parabol fit)
                     %v          =
             1679.14221+85.13439*z-0.16319*z^2-0.02893*z^3+2.89945*10^-4*z^4;      %origin
             fit for KCI+5%
                     %v          =
             1790.76631+80.65363*z-0.1546*z^2-0.02741*z^3+2.74685*10^-4*z^4;      %origin fit
             for KCI+10%
                     %v          =
             2014.0145+71.69211*z-0.13742*z^2-0.02437*z^3+2.44164*10^-4*z^4;      %origin fit
             for KCI+20%

                     % emergent angle

                     alpha       = asin(p*v);
                 end

                 % calulate second part of trace for plot
                 i = i-1;   %because while circle goes one step to far

                 for n=1:1:i-1
                     depth(i+n)  = depth(i-n);
                     offset(i+n) = offset(i)*2-offset(i-n);
                 end

                 % matrix with results Z,X,T,V
                 % -deltaz/-deltax because while circle goes one step to far

                 result(m,1) = (z-deltaz);
                 result(m,2) = 2*(x-deltax);
                 result(m,3) = time*2;
                 result(m,4) = 1/p;


                 %plot
                 figure(1)
                 plot(offset,depth)
                 set(gca,'fontsize',14,'fontweight','b')
                 title('Diving wave incident angle 70° to
             26°','fontsize',18,'fontweight','b')
                 xlabel('offset in m','fontsize',18,'fontweight','b')
                 ylabel('depth in m','fontsize',18,'fontweight','b')
                 hold on

             end
```

B.2   Calculation for Herglotz-Wiechert inversion

The travel times of the diving wave can be used to calculate a velocity-depth function with help of the Herglotz-Wiechert inversion formula (chapter 5.1.2)

```
                              Herglotz_Wiechert
% calculate veolcity-depth funktion using Herglotz-Wiechert
% Anja Diez


clear all, close all;
clf;


% variables
deltax      = 0.01;                % steps in m for calculation of depth and
velocity
stop        = 80;              % should not be longer than biggest offset

% Matrix with results, depth - velocity
res=zeros(stop+1,2);
rho=zeros(stop+1,1);
%zt=zeros(stop+1,1);


% values of fit
% 08001all
% a = 0.00243;
% b = 0.37199;
% c = 0.01308;
% d = 0.02544;
% e = 2.95894*10^(-4);
% 08001 Shot 3-33
% a = 0.01609;
% b = 0.02286;
% c = 0.00247;
% d = 0.35695;
% e = 2.95894*10^-4;
% 08001 Shot 3-33 kill Shot 6 offset 1.5
% a = 0.01485;
% b = 0.02492;
% c = 0.00234;
% d = 0.43718;
% e = 2.68835*10^-4;
% 08002all
% a = 0.40602;
% b = 0.00205;
% c = 0.00525;
% d = 0.10254;
% e = -3.78025*10^(-4);
% 08002 Shot 3-33
a = 0.01611;
b = 0.02846;
c = 0.00138;
d = 0.79899;
e = 2.44727*10^-4;
% 08001+08002
% a = 0.01308;
% b = 0.02544;
% c = 0.00243;
% d = 0.37199;
% e = 2.95894*10^-4;

% vector with veolcities for different offsets

for i=1:1:(stop/deltax+1)
    j           = (i-1)*deltax;         % calculate j=offset to be able to start
at surface j=0
    offset(i)   = j;
    v(i)        = (a*b*exp(-b*j)+c*d*exp(-d*j)+e)^-1;
    % calculate apperent velocity from fitted curve
    av(i)       = j/(a*(1-exp(-b*j))+c*(1-exp(-d*j))+e*j);
    av(1) = 0;
end

% calculate depth z(v)

for i=1:1:(stop/deltax+1)
    z       = 0;                % start depth for every ray
    %Zt      = 0;                % t for triangular calculation
    % Summing up depth parts for one ray
    % only go to i-1

    for x=1:1:i-1
        dz      = (acosh(v(i)/av(x)))^-1*deltax;
        z       = z+dz;
        % triangular calculation of integral
        %dzt     = ((acosh(v(i)/av(x)))^-1+(acosh(v(i)/av(x+1)))^-1)/2*deltax;
        %Zt      = Zt+dzt;
    end
    z(i)        = 1/pi*z;         % vector with results for depth
    %zt(i)       = 1/pi*Zt;
    % Matrix with velocity - depth pairs
    res(i,1)    = v(i);
    res(i,2)    = z(i);

    % calculate density rho(z)
    rho(i,1)        = 0.915/(1+((3.8-v(i)/1000)/2.25)^1.22);        % using
Kohnen
    rholin(i,1)     = 0.221*v(i)/1000+0.059;                %using Robin
linear
end


%plot
figure(1)
plot(v,z)
set(gca,'YDir','reverse')
figure(2)
plot(offset,v)
figure(3)
plot(rho,z,rholin,z)
set(gca,'YDir','reverse')
```

B.3   Calculation for AVA

Program used to calculate the reflection coefficient for changes in P-wave velocity (chapter 5.2.2)

```
                              Reflection_ampli
% Calculate Amplitude variation with offset for possible reflection within
% the ice
% rho1=rho2
% vp_max = 3800 m/s , vs_max = 1950 m/s -> vp/vs = 76/39
% Anja Diez


clear all, close all;

vp1=3800;          %velocity ice


for i=1:1:20
    in          = i*10;              % velocity increas in steps of 10 m/s
    vp(i)       = vp1+in/2;        % vp=(vp1+vp2)/2
    deltavp(i)  = in;             % deltavp = vp2-vp1

    for j=1:1:16
        %calculate Reflection amplitude for different angles
        R(j,i)      =
((1+(tan(j/180*pi))^2)/2-(4/(76/39)^2*(sin(j/180*pi))^2))*(deltavp(i)/vp(i));
        theta(j)    = j;
    end

end
%plot
figure(1)
set(0,'DefaultAxesColorOrder',hsv)
plot(theta,R)
title('AVA vp=3800 m/s, velcity increas in steps of 10 m/s','fontsize',12)
xlabel('angle in degree - theta','fontsize',10)
ylabel('Reflection amplitude R(theta)','fontsize',10)
%colorbar('location','southoutside')
%hold on
```